This is to certify that the
dissertation entitled

Electronic and Structural Properties of Functional
Nanostructures

presented by

Teng Yang

has been accepted towards fulfillment
of the requirements for the

_____Ph.D._____ degree in _____Physics and Astronomy_____

David Womqiul

Major Professor's Signature

May 7, 2009

Date

PLACE IN RETURN BOX to remove this checkout from your record.
TO AVOID FINES return on or before date due.
MAY BE RECALLED with earlier due date if requested.

DATE DUE	DATE DUE	DATE DUE

5/08 K:/Proj/Acc&Pres/CIRC/DateDue.indd

ELECTRONIC AND STRUCTURAL PROPERTIES OF FUNCTIONAL
NANOSTRUCTURES

By

TENG YANG

A DISSERTATION

Submitted to
Michigan State University
in partial fulfillment of the requirements
for the degree of

DOCTOR OF PHILOSOPHY

Physics and Astronomy

2009

ABSTRACT

ELECTRONIC AND STRUCTURAL PROPERTIES OF FUNCTIONAL NANOSTRUCTURES

By

Teng Yang

In this Thesis, I present a study of electronic and structural properties of functional nanostructures such as MoS_xI_y nanowires, self-assembled monolayer on top of metallic surfaces and structural changes induced in graphite by photo excitations. MoS_xI_y nanowires, which can be easily synthesized in one step, show many advantages over conventional carbon nanotubes in molecular electronics and many other applications. But how to self-assemble them into desired pattern for practical electronic network? Self-assembled monolayers of polymers on metallic surfaces may help to guide pattern formation of some nanomaterials such as MoS_xI_y nanowires. I have investigated the physical properties of these nanoscale wires and microscopic self-assembly mechanisms of patterns by total energy calculations combined with molecular dynamics simulations and structure optimization.

First, I studied the stability of novel Molybdenum chalcohalide nanowires, a candidate for molecular electronics applications.

Next, I investigated the self-assembly of nanoparticles into ordered arrays with the aid of a template. Such templates, I showed, can be formed by polymer adsorption on surfaces such as highly ordered pyrolytic graphite and Ag(111).

Finally, I studied the physical origin of of structural changes induced in graphite by light in form of a femtosecond laser pulse.

To my father and mother,

younger sisters Hsia and Caiping

and black-belted Bárbara da Fonseca Magnani.

ACKNOWLEDGMENTS

Countless number of people contribute to one Ph.D Thesis and this one is no exception. I am so grateful to many people – my advisor, my Guidance Committee, my friends, my family and others. This Thesis can't be possible without their strong support and encouragement, I want to take a full use of this part to thank them.

First of all I thank my advisor Prof. David Tománek. He has done so much that an excellent advisor does for his student. He initiated many fruitful discussions with me and showed me how to communicate more efficiently with research colleagues. He showed me hand by hand how important it is to make a successful presentation and how to make me successful. He supported me to attend domestically and internationally as many workshops, colloquia and conferences as possible and introduced me to almost all the top scientists in my field. During these years, I have also learned from his great passion to scientific research, his unique way to inspire students to think, and his sincere concern to human beings, for instance, on the ethnical controversy of poverty and bio-fuel. And far more than that, Prof. Tománek is like my second father who puts so many touching concerns to my life and my future. I would say that I would not have grown up so fast and be in this position without his continuous support and guidance.

I want to show my gratitude to the members of my Guidance Committee: Professor Vladimir Zelevinsky, Professor Chong-Yu Ruan, Professor Carlo Piermarocchi, Professor C. P. Yuan.

I feel fortunate to collaborating with Prof. Savas Berber, Prof. Gotthard Seifert, Prof. Glen P. Miller and Prof. Karsten Pohl. A special thank-you goes to Prof. Savas Berber and Gotthard Seifert. Savas Berber taught me in an exhaustive way on how SIESTA code works and tolerated me and my trivially naive questions. The

productive exchange of viewpoints and discussions with him has been a treasure to me. I want to thank Prof. Seifert for his great encouragement to me.

Among many friends, Jerry McAllister takes a special position. He has been a loyal listener to "Science Friday" in National Public Radio program every Friday afternoon, always had a great perspective on science-related issues and most importantly never hesitated to share it with me. I still clearly remember how excited he was when talking to me on the phone about his "buckyball", in which he accidentally burned his sweet potato. Moreover he has been a wonderful English tutor to me. I also want to say a special "thank you" to Anne Serotkin for her encouragement and her wonderful book gift "a beautiful mind". I thank Daniel Enderich for his great effort to polish my writing. I thank Kiseok Chang and Kristsada Kittimanapun for many scientific discussions in our BPS-4240 office. Many friends added a lot of enthusiastic and beautiful memories to my MSU life: they are Sharron Xiaohong Ye, Nini Xian Zhang, Jiwu Liu, the Yorks, Cathy Yunfang Cui, Yueya Sun, Fangye Sun.

Finally I thank my family – my parents and my sisters for putting up with me.

Table of Contents

List of Tables

List of Figures

Chapter 1

Introduction

1.1 Overview

1.1.1 Transition metal chalcohalide nanowires

One of the major challenges in the emerging field of molecular electronics is to identify conducting nanostructures with desired electronic properties, which are stable and easy to manipulate. Due to their high stability and favorable electronic properties [1], carbon nanotubes [2] have been discussed extensively as promising candidates for molecular electronics applications. A major drawback is our current inability to synthesize or to isolate nanotubes with a given diameter and chiral angle, which determine their metallic or semiconducting nature. Moreover, single-wall carbon nanotubes are hard to isolate from stable bundles, which form spontaneously during synthesis [3]. In this respect, recently synthesized Mo chalcohalide nanowires [4], such as $Mo_xS_yI_z$, seem to offer several advantages by combining uniform metallic behavior, atomic-scale perfection and easy dispersability [5, 6].

Chalcohalides of molybdenum and other transition metals are known to form stable, intriguing 2- and 1-dimensional structures [7] with an unusual combination of electronic properties [8] including good conductance, superconductivity, magnetism,
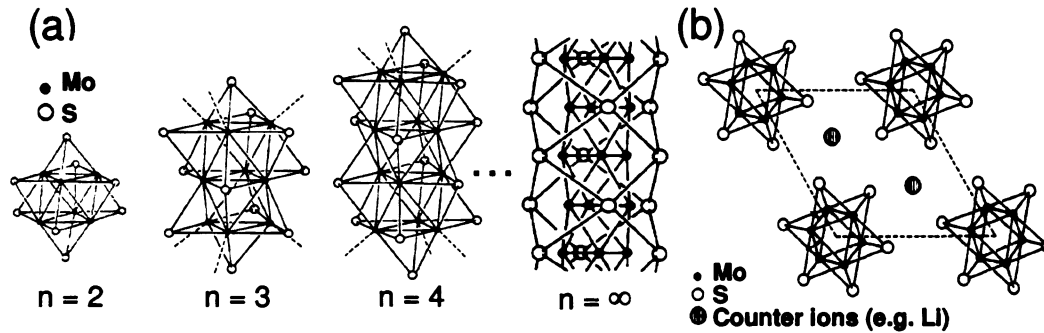
Figure 1.1: Schematic structure of $Mo_{3n}S_{3n+2}$ clusters assembled to infinite nanowires. (a) Chevrel phase of Mo_6S_8. (b) End-on view of nanowires forming triangular lattices, stabilized by intercalated counter-ions (e.g. lithium).

and nonlinear polarizability. These layered or filamentous substances are known as catalysts [9] and, to a much larger degree, as excellent solid lubricants [10, 11, 9]. Their potential to become unique building blocks of nano-devices has barely been noticed so far [9], in stark contrast to popular carbon nanotubes [12]. Recent progress in the synthesis of $Mo_xS_yI_z$ nanowires [13] suggests that these monodisperse, self-supporting nanostructures may nicely complement carbon nanotubes by avoiding their shortcomings such as strong dependence of conductivity on the nanotube structure and difficulty to separate bundled tubes [12].

Chalcogenide compounds containing Mo and S have been studied for a long time [7, 14]. Whereas the best known allotropes, including MoS_2, are insulating and form layered compounds, more interesting structures often occur at lower sulfur concentrations. Well known are Chevrel phases, characterized by cluster compounds with Mo_6S_8 subunits, which may be finite clusters or needle-like quasi-1D systems [15], shown in Fig 1.1(a). All these interesting structures necessitate the presence of metal counter-ions, depicted in Fig 1.1(b), for their synthesis. Besides providing structural stability, the main role of the counter-ions is to transfer electrons into the chalcogenide substructures [16, 17], thereby promoting formation of an ionic crystal [18]. In their most stable electronic configuration, many of these compounds contain $(Mo_6S_6)^{2-}$ building blocks [14].

2

I found it intriguing to study the possibility of stabilizing Mo-based nanowires by substituting the divalent sulfur by a monovalent halogen atom (i.e. iodine) with a similar electronegativity, thus avoiding the need for metal counter-ions. In this way, a desirable electronic configuration could be preserved while maintaining the covalent character of the system and avoiding transformation to an ionic crystal.

Combining sub-nanometer diameter with structural stability and interesting electronic properties, transition metal chalcogenide nanowires have been discussed as a potentially viable alternative to carbon nanotubes [19] for many applications. Mo_6 $S_{9-x}I_x$ nanowires, in particular, have been studied extensively both experimentally [20, 21, 22, 6, 5, 23, 24, 25, 26, 27, 28, 29, 30, 31, 32, 33, 34] and theoretically [35, 36, 37]. In contrast to other nanowires and nanotubes, $Mo_6S_{9-x}I_x$ nanowires are believed to be metallic, independent of their structure [35, 36, 21], and can be synthesized [38], dispersed [6, 5] and functionalized [23] in a straightforward manner. Nano-mechanical studies indicate a very low shear modulus of the bundled nanowires [26], suggesting self-lubricating properties and potential applications in nano-tribology [39]. Sulfur terminators act as "alligator clips", providing optimum contact to gold leads for molecular electronics applications.

In spite of these many studies, several questions about $Mo_6S_{9-x}I_x$ nanowires still await a definitive answer. There is a consensus that the skeleton of these systems consists of Mo octahedra, which are functionalized by S and I adsorbates and connected by bridges containing S or I atoms. Still, there is an open controversy about the atomic arrangement in nanowires with $x = 4.5$ and $x = 6$, which have been observed as stable compounds. X-Ray Diffraction (XRD) [21] and Extended X-ray Absorption Fine Structure (EXAFS) [40] studies agree in the identification of Mo octahedra as stable building blocks of the nanowires, but disagree about the precise positions of sulfur and iodine. In particular, both iodine [21, 40] and sulfur [33, 35, 36] have been proposed as constituents of the bridges connecting the Mo octahedral building

blocks. Additional uncertainty exists about whether the connecting bridges contain three [41, 35] or four [26, 40] atoms.

1.1.2 Controlled self-assembly of molecules as nano-template

Controlled self-assembly of molecules to form ordered nanoscale patterns is an area of active research. These superstructures often exhibit unusual properties [42] and are finding numerous applications in nanotechnology, including use as nanotemplates [43]. Nanotemplates enable directed assembly of nanoscale objects and allow for the transfer of those patterned objects onto a substrate. For example, as nanoparticles can be selectively attached to either molecular or polymeric species, nanotemplates derived from self-assembled molecules or polymers provide an efficient means to prepare ordered arrays of uniformly spaced nanoparticles. Nanotemplates of this type permit small feature sizes and high assembly rates that are unrivaled by current lithographic techniques including electron-beam nanolithography and scanning probe methods such as dip-pen nanolithography [44] and field-assisted nanolithography [45].

Self-assembled monolayers (SAMs) of molecular and polymeric species on highly oriented pyrolytic graphite (HOPG) have attracted much attention, since the formation of various adsorption patterns can be monitored using scanning tunneling microscopy (STM) methods [46, 47, 48, 49]. Although many patterns have been reported even for alkane films on graphite, the energetic grounds for the optimum SAM structure have never been investigated. Since the interplay between adsorbate-adsorbate and adsorbate-substrate interactions ultimately determines the equilibrium geometry of the molecular assemblies, it should be possible to induce specific changes in the SAM superstructures by modifying the terminal functional groups of the molecules in a pre-determined manner. Unfortunately, published STM data of SAMs on graphite do not provide a quantitative interpretation of the resulting superstructures and therefore do not allow for predictions concerning the effect of specific functional groups on

4

Figure 1.2: (a)-(d) Schematic depiction of a controlled assembly of nanoparticles on a re-usable nano-template (green), followed by transfer onto an unpatterned substrate (red).

the corresponding self-assembled superstructure.

Ordered arrays of molecules or nanoparticles such as C_{60} fullerenes have a great number of practical applications, ranging from sensors and biological interfaces [50] to organic electronics [51], photovoltaics, and novel computational methods such as quantum dot cellular automata and, with endohedral fullerenes, spin-based quantum computers [52, 53]. Generally speaking, self-assembled monolayers of molecules (SAMs) form as a result of a delicate balance between competing molecule–substrate and intermolecular interactions [54]. Therefore, to control such self-assembly processes and grow molecular arrays of designed geometries, it is mandatory to understand how this balance of interactions reflects onto the SAM's final structure [55].

1.1.3 Photo-induced structural transformations

There is growing interest in displacing atoms in materials by photo-excitations [56]. Observations of transient structures thus formed offer a glimpse into the transformation pathways between different structures. Carbon, with its propensity to form a wide range of bonding networks (sp, sp^2, sp^3), is ideal to study the dynamics of bond formation and rupture. Of particular interest is the conversion of rhombohedral graphite to diamond [57, 58, 59, 60, 61]. Whereas pioneering ultrafast optical studies of graphite have provided evidence of photo-induced melting [62, 63] and generation of coherent phonons [64, 65] by observing changes in the electronic properties, direct determination of lattice structural dynamics proves to be difficult, especially in the far-from-equilibrium regime. X-ray diffraction has been successful in observing nonthermal structural changes in semiconductors [66], relying primarily on the integrated Bragg intensities. However, direct observation of atomic motion in nanostructures with low atomic number, such as carbon, is very challenging and has not yet been achieved. Much more promising is electron diffraction, with its five orders of magnitude enhanced scattering cross-section and advances allowing experimental

6

observations on the femtosecond time scale [67, 68, 69, 70], offers a new window into the realm of photo-excited structural dynamics, with resolution down to $\lesssim 1$ nm [67, 70, 71].

1.2   Outline of the dissertation

This PhD Thesis contains 9 Chapters, including this introductory chapter. In Chapter 2 I present a detailed description of the computational methods used in this Thesis.

In Chapters 3 to 5, I present a study of various physical properties of a new kind of molybdenum chalcohalide nanowires, which are considered powerful candidates for molecular electronics applications.

In Chapter 3, I investigate the equilibrium geometry and electronic structure of $Mo_{12}S_9I_9$ nanowires. The skeleton of these unusually stable nanowires consists of rigid, functionalized Mo octahedra, connected by flexible, bi-stable sulphur bridges. Interestingly, this structural flexibility translates into a capability to stretch up to $\approx 20\%$ at almost no energy cost. My results indicate that the nanowires change from conductors to narrow-gap magnetic semiconductors in one of their structural isomers.

In Chapter 4, I combine *ab initio* density functional and quantum transport calculations based on the nonequilibrium Green's function formalism to compare structural, electronic, and transport properties of $Mo_6S_{6-x}I_x$ nanowires with carbon nanotubes. I find systems with $x = 2$ to be particularly stable and rigid, with their electronic structure and conductance close to that of metallic $(13, 13)$ single-wall carbon nanotubes. $Mo_6S_{6-x}I_x$ nanowires are conductive irrespective of their structure, more easily separable than carbon nanotubes, and capable of forming ideal contacts to Au leads through thio-groups.

Chapter 5 covers the compositional ordering and quantum transport study in

$Mo_6S_{9-x}I_x$ nanowires in complement to Chapter 3. I find nanowires with $x = 3$ to be particularly stable. Nanowires with other compositions are likely to phase separate into iodine-rich and iodine-depleted segments, some of which should have the stoichiometry $Mo_6S_6I_3$. My transport calculations, based on the nonequilibrium Green's function formalism, indicate that the nanowires are metallic independent of composition and exhibit a quantum conductance of $G = 3G_0$, with the three conductance channels involving the S_3 bridges.

Self-assembly of nanomaterials into ordered arrays with the aid of a template is important to form desired networks for molecular electronics applications. In Chapters 6 to 7, I present results for molecule and polymer adsorption on metallic surfaces such as HOPG and Ag(111).

Chapter 6 is devoted to the self-assembly of long chain alkanes and related alcohol and carboxylic acid molecules on graphite. I studied it using *ab initio* total energy calculations and compare my results to scanning tunneling microscopy (STM) measurements. For each system, I identified the optimum adsorption geometry and could thus explain the energetic origin of the domain formation observed in the STM images. My results for the hierarchy of adsorbate-adsorbate and adsorbate-substrate interactions provide a quantitative basis to understand the ordering of long chain alkanes in self-assembled monolayers and ways to modify it using alcohol and acid functional groups.

Combining my computational results with experimental studies performed by others, I present in Chapter 7 a theoretical study of the self-assembly of C_{60} molecules functionalized with long chain alkanes on the (111) surface of silver. I find that the conformation of the functionalized C_{60} molecule changes upon adsorption on Ag(111) and that the unit cell size in the self-assembled monolayer is determined by the interactions between the functional groups. I show that C_{60} molecules can be assembled in ordered two-dimensional arrays with intermolecular distances much

larger than those in compact C_{60} layers. This introduces a novel way to control the adsorption pattern by appropriate chemical functionalization.

Finally, in Chapter 8 I address the stability of particular templates and study the possibility of structural changes induced in graphite by a femtosecond laser pulse. Experimental results suggest that a variety of interesting phenomena occur following irradiation by light. At moderate fluences of ≤ 21 mJ/cm^2, lattice vibrations are observed to thermalize on a time scale of ≈ 8 ps. At higher fluences approaching the damage threshold, lattice vibration amplitudes saturate. Following a marked initial contraction, graphite is driven non-thermally into a transient state with sp^3-like character, forming interlayer bonds. Using *ab initio* density functional calculations, I trace the governing mechanism back to electronic structure changes following the photo-excitation and find that the modified force field in the excited state and the Coulomb stress are the main forces driving this structural change.

Chapter 2

Density Functional Theory for *ab initio* simulations

In order to get insight into the intriguing electronic and structural properties of nanostructures, we need to solve the many-body Schrödinger equation for those systems,

$$H\Phi = E\Phi,$$

where the many-body wavefunction Φ depends on electronic and ionic coordinates. The Hamiltonian is written as

$$H = \sum_i \frac{p_i^2}{2m} + \sum_I \frac{p_I^2}{2M} + \sum_{i,I} U_{ion}(\vec{r}_i - \vec{R}_I) + \sum_{i \neq j} \frac{e^2}{|\vec{r}_i - \vec{r}_j|} + \sum_{I \neq J} \frac{Z_I Z_J e^2}{|\vec{R}_I - \vec{R}_J|}. \quad (2.1)$$

The first two terms are kinetic energies of electrons and nuclei; the last 3 terms are electron-ion, electron-electron and ion-ion interactions, respectively. $\vec{r}_i$ denotes the electron coordinates and $\vec{R}_I$ the nuclei positions in the lattice.

In systems with many electrons, it is impossible to solve equation (2.1) exactly. In view of this difficult problem, several approximations have been developed and

applied successfully to a large number of solid-state systems [72]. In the ground state, these include the adiabatic (or Born-Oppenheimer) approximation [73], which has long been used to separate the nuclear motion from electron motion, since the electrons are four orders of magnitude lighter than the ions. Other approximations include the Hartree-Fock (HF) self-consistent method [74, 75] and the popular Density Functional Theory (DFT) [76]. The basic advantage of DFT over HF is the treatment of both electron exchange and correlation in DFT. The exchange-correlation energy is exact in selected systems and approximate in others. Infinite periodic solids are treated as ideal crystals with translational symmetry. Using these methods, we can map the unsolvable many-body problem approximately onto a single-particle problem.

DFT would not be very successful in studying electronic and structural properties of atoms, molecules, solids, surface and interfaces without the Kohn-Sham approach to obtain a workable solution [77]. The Kohn-Sham approach maps a many-body problem onto an independent-particle problem by splitting off the difficult many-body terms into an exchange-correlation functional of the electron density. I will start with a brief introduction of the basic idea behind the Kohn-Sham approach, discuss how it transforms interacting electrons to non-interacting quasi-electrons and finally include selected details about how it is implemented into popular computer codes like SIESTA [78, 79, 80] (with a localized basis) and Quantum-Espresso [81] (with a plane-wave basis) to obtain the electron density, total energy, and other derived quantities such as forces.

2.1 Density Functional Theory and Kohn-Sham equations

2.1.1 Hohenberg-Kohn theorem

The essence of the Density Functional Theory is that in the electronic ground state, the total energy of a system of interacting electrons is a unique functional of the ground state electron density $n_0(\vec{r})$ only. According to the Hohenberg-Kohn theorem, the external potential $V_{ext}(\vec{r})$ determines uniquely the ground state density $n_0(\vec{r})$ of the interacting electrons. For any external potential $V_{ext}(\vec{r})$, we can write the total energy as a universal functional $E[n]$ in terms of the density $n(\vec{r})$, which is globally minimized only by the exact ground state density $n_0(\vec{r})$. The global minimum value of this functional gives the ground state energy as

$$E_{HK}[n] = T[n] + E_{int}[n] + \int d^3 r V_{ext}(\vec{r}) n(\vec{r}) + E_{II}, \qquad (2.2)$$

where E_{II} is the energy of ions, which are treated classically in the following.

It follows that once the kinetic energy $T[n]$ of the interacting particles and interaction energy $E_{int}[n]$(equal to the repulsive Hartree energy and energy terms associated with exchange and correlation interactions) are known, the ground state charge density $n(\vec{r})$ and energy can be determined by minimizing the total energy (2.2) with respect to $n(\vec{r})$. The most challenging of the energy terms is $E_{int}[n]$, which is known exactly only in the hydrogen atom and the uniform electron gas. In other systems, the $E_{int}[n]$ functional is typically determined numerically using various approximations, to be discussed in the following.

2.1.2 Kohn-Sham equations

The ground state charge density determines the total energy and derived properties of the many-body system. The Kohn-Sham approach is to identify a system of non-interacting quasi-electrons, the ground state density of which is equal to that of the original system of interacting electrons. Different from the energy functional (2.2), the ground state energy functional of this system is rewritten in the form

$$E_{KS}[n] = T_0[n] + E_{int}[n] + \int d^3r V_{ext}(\vec{r}) n(\vec{r}) + E_{II}$$
$$= T_0[n] + E_{Hartree}[n] + E_{xc}[n] + \int d^3r V_{ext}(\vec{r}) n(\vec{r}) + E_{II}. \tag{2.3}$$

The system of N independent particles (quasi-electrons) in a given potential $V_{ext}(\vec{r})$ can be described using a Schrödinger equation, which yields the wavefunctions $\psi_i(\vec{r})$ of the quasi-electrons. Then, the total electron density is given by

$$n(\vec{r}) = \sum_{i=1}^{N} |\psi_i(\vec{r})|^2. \tag{2.4}$$

With the quasi-electron wavefunctions identified, the kinetic energy T_0 of the quasi-electrons (which is different from the electronic kinetic energy T) is

$$T_0 = -\frac{1}{2} \sum_{i=1}^{N} \left\langle \psi_i \left| \nabla^2 \right| \psi_i \right\rangle \tag{2.5}$$

and the Coulomb energy of the interacting quasi-electrons (Hartree energy) is given by

$$E_{Hartree} = \frac{1}{2} \int d^3r d^3r' \frac{n(\vec{r}) n(\vec{r}\,')}{|\vec{r} - \vec{r}\,'|}. \tag{2.6}$$

The remaining term, describing the exchange and correlation energy of these particles,

13

can be rewritten as a functional of n that needs to be determined, as

$$E_{xc}[n] = T[n] + E_{int}[n] - T_0[n] - E_{Hartree}[n].$$
(2.7)

The most common way to solve the Kohn-Sham independent quasi-particle problem in the electronic ground state is to perform variational minimization of the energy functional (2.3) with respect to the charge density $n(\vec{r})$. In the energy functional (2.3), most terms (i.e. E_{xc}, $E_{Hartree}$) are functionals of the electron density, except T_0 in Eq.(2.5), which is a functional of the wavefunctions. Variational minimization with respect to orthonormal wavefunctions ($< \psi_i | \psi_j >= \delta_{ij}$) can be performed using the method of Lagrange multipliers, yielding

$$\delta \left[E_{KS}[n] - \lambda_i (< \psi_i | \psi_i > -1) \right] = 0.$$
(2.8)

This leads to a set of equations that, together with Eq.(2.4), are called the Kohn-Sham equations,

$$\left[-\frac{1}{2} \nabla^2 + V_{eff}(\vec{r}) \right] \psi_i(\vec{r}) = \lambda_i \psi_i(\vec{r}).$$
(2.9)

Here, $V_{eff}(\vec{r})$ can be viewed as the effective potential, which depends implicitly on $n(\vec{r})$ and is given by

$$V_{eff}(\vec{r}) = V_{ext}(\vec{r}) + \frac{\delta E_{Hartree}}{\delta n} + \frac{\delta E_{xc}}{\delta n} = V_{ext}(\vec{r}) + V_{Hartree}(\vec{r}) + V_{xc}(\vec{r}).$$
(2.10)

The Kohn-Sham eigenvalues λ_i are not to be confused with the energies of electrons [82].

The attraction of the Kohn-Sham approach lies in the way of separating off the independent quasi-particle kinetic energy, the Hartree energy, and the interaction with the external potential $V_{ext}(\vec{r})$; these form the largest fraction of the total energy and can be determined in a straightforward way. The remaining exchange-correlation

functional $E_{xc}[n]$ is rather small and can be approximated by a local function of $n(\vec{r})$ and its gradients. As mentioned earlier, the DFT treatment of correlation is approximate, but still superior to its complete neglect in the Hartree-Fock approach. Once a proper approximation of $E_{xc}[n]$ is identified, the Kohn-Sham equations can be solved self-consistently, yielding $n(\vec{r})$ and the total energy of the many-body system. Widely used methods to describe the exchange-correlation functional are the Local Density Approximation (LDA) [77] and Generalized Gradient Approximation (GGA) [83]. LDA is exact in the uniform electron gas and justified by the finding that the exchange-correlation energy per electron $\epsilon_{xc}(\vec{r})$ varies slowly in an electron gas of slowly varying density, where it is well represented by a local function. The proper parametrization of this local function can be obtained using more microscopic quantum Monte Carlo calculations [84, 85, 86] for a uniform electron gas.

2.2 Solving the set of Kohn-Sham equations

In the following, I provide a step-by-step explanation of solving self-consistently the set of Kohn-Sham equations, as implemented in the SIESTA code [78, 79, 80, 87] that uses a localized basis of atomic orbitals, and the Quantum-Espresso code [81] that uses a plane-wave basis for a given system.

2.2.1 Self-consistency process overview

The self-consistency procedure can be summarized within a few essential steps as indicated in Table 2.1. Once the initial electronic charge density $n_0^{in}(\vec{r})$ is determined, most commonly as a superposition of atomic orbitals, the single-particle effective potential V_{eff} can be constructed by using approximations such as LDA. Next, we need to decide if we wish to expand the system wave function in a plane-wave basis or a localized atomic orbital basis. A finite system is solved conveniently in real

Step 1:
Get an initial $n_0^{in}(\vec{r})$

$\downarrow$

Step 2:
Construct V_{KS}
$V_{eff} = V_{ext} + V_{Hartree} + V_{xc}$

$\downarrow$

Step 3:
Expand $\psi_i(\vec{r})$ in local orbitals $\phi(\vec{r})$
and solve $H_{eff}\psi_i(\vec{r}) = \varepsilon_i\psi_i(\vec{r})$

$\downarrow$

Step 4:
Calculate new $n^{out}(\vec{r}) = \sum_i |\psi_i(\vec{r})|^2$
Obtain difference $\delta n = n^{out}(\vec{r}) - n^{in}(\vec{r})$
Is $\delta n \leq$ tolerance?

$\downarrow$

No.	Yes.
Construct $n_{i+1}^{in} = \alpha n_i^{out} + (1-\alpha)n_i^{in}$	Self-consistency has been reached.
Go back to Step 2	Calculate the total energy.
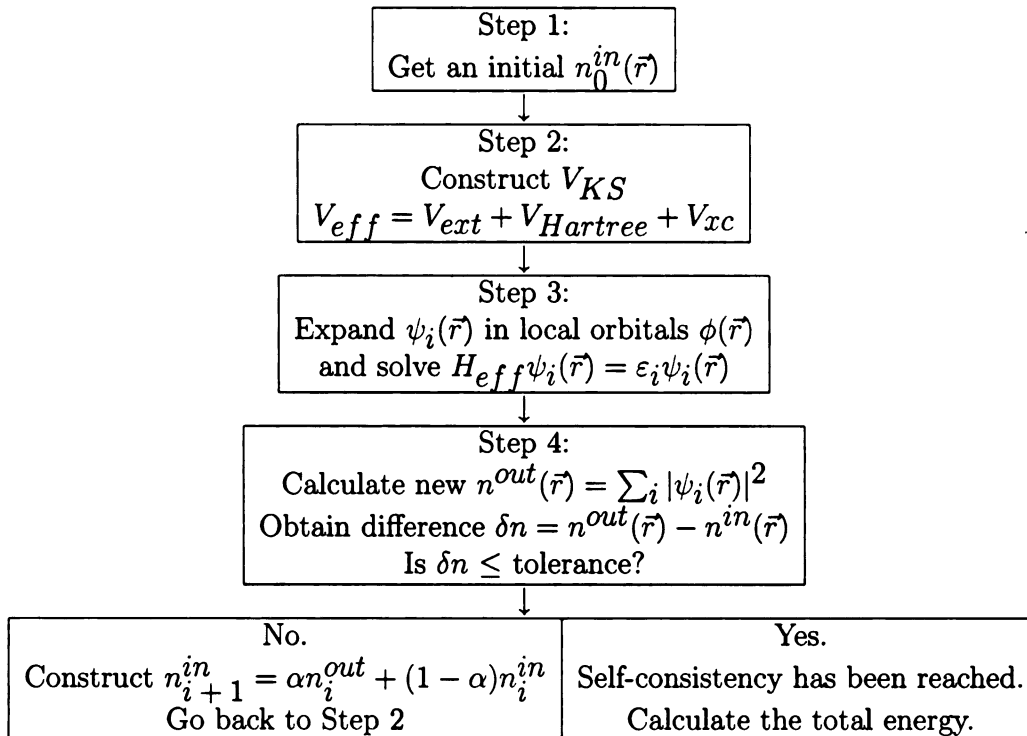
Table 2.1: The self-consistency procedure.

space, whereas in an infinite periodic system, we will benefit computationally from using reciprocal space to expand the Bloch states and to diagonalize the Kohn-Sham matrix. To accelerate convergence, only fraction α of the output charge density n_i^{out} is typically mixed with the input charge density n_i^{in}, with $\alpha \lesssim 5\%$. Once we find that the output charge density is nearly equal to the input density, which typically requires several itineraries, we have reached self-consistency and can determine the total energy and related quantities. In the next sub-section, I will introduce an important simplification that will reduce the computational effort significantly.

2.2.2 Norm-conserving *ab initio* pseudopotentials

Besides the Born-Oppenheimer approximation for the separation of the electronic and ionic motion and the Local Density or Generalized Gradient Approximation for the exchange and correlation energy terms, we introduce pseudopotentials as a useful

concept to separate the interesting valence electrons from the relatively inert core electrons.

The core electrons play a negligible role in the physical properties of solids. Consequently, it is convenient to combine the strong nuclear Coulomb potential and the potential of the tightly bound inert core electrons into one effective pseudopotential acting on valence electrons. Parameter-free pseudopotentials can be generated from atomic calculations and used without any modifications to describe valence electrons in molecules or solids. While not unique, pseudopotentials need to accurately represent the scattering of valence electrons from the ion cores. *Ab initio* pseudopotentials are typically non-local and energy dependent (i.e. they depend on the quasi-electron wave function and energy eigenvalue). Norm-conserving pseudopotentials [88] generate valence electron pseudo-wavefunctions with the same norm (total charge inside a finite-size sphere) as all-electron atomic wave functions outside a cutoff radius. Pseudopotentials should furthermore be transferrable, i.e. they should reproduce well the DFT energy eigenvalues in atoms with different electronic configurations. Unlike the standard Hamann-Schluter-Chiang [88] or Troullier-Martins [89] pseudopotentials, "ultrasoft" pseudopotentials [90] are also energy dependent.

Most calculations in this Thesis are performed using LDA. I construct norm-conserving non-local Troullier-Martins pseudopotentials [88, 89] using the Ceperley-Alder exchange-correlation functional [91] in LDA. As in Hamann-Schluter-Chiang pseudopotentials of the same type, non-locality is expressed in terms of a dependence of the pseudopotential on the orbital angular momentum l. The generation of a pseudopotential involves the following steps.

(1) Valence electron eigenvalues ε_l and eigenfunctions $\phi_l(\vec{r})$ are obtained by performing an all-electron calculation for an atom in the ground state and selected excited or charged states, using a given exchange-correlation density functional.

(2) For each angular momentum l, a pseudo-wavefunction $\phi_l^{PS}(\vec{r})$ with no radial

nodes is generated such that the norm $Q(r) = \int_0^r d^3r \, ' \phi_l^{PS*}(\vec{r}\,') \phi_l^{PS}(\vec{r}\,')$ of the pseudo-wavefunction $\phi_l^{PS}(\vec{r})$ equals that of the all-electron wavefunction $\phi_l(\vec{r})$ for $r > r_C$. In general, reducing the value of r_C leads to more "transferable" [82], but deeper pseudopotentials, associated with less smooth pseudo-wavefunctions [72].

(3) Inverting the Kohn-Sham equations, leads to a total "screened" pseudopotential,

$$V_{l,\,total}(r) = \varepsilon - \frac{\hbar^2}{2m_e}\left[\frac{l(l+1)}{2r^2} - \frac{\frac{d^2}{dr^2}\phi_l^{PS}(r)}{\phi_l^{PS}(r)}\right].$$

The ionic pseudopotential is then obtained by subtracting the Hartree term $V_{Hartree}^{PS}(r)$ and exchange-correlation term $V_{xc}^{PS}(r)$ from $V_{l,\,total}$, yielding

$$V_l(r) = V_{l,\,total}(r) - V_{Hartree}^{PS}(r) - V_{xc}^{PS}(r).$$

As will be shown later on, it is convenient to decompose $V_l(r)$ into a l-independent local term and a non-local part,

$$V_l(r) = V_{local}(r) + \delta V_l(r).$$

$V_{local}(r)$ includes all the long-range effects of the Coulomb potential, and $\delta V_l(r)$ is a non-local l-dependent pseudopotential.

(4) A convenient nonlocal form, proposed by Kleinman and Bylander (KB) [92], reduces the computational effort by requiring only products of projection operators,

$$\hat{V}_{NL} = V_{local}(r) + \hat{V}_{NL}^{KB},$$

$$\hat{V}_{NL}^{KB} = \sum_{l=0}^{l_{max}^{KB}} \sum_{m=-l}^{l} \frac{|\delta V_l(r)\psi_{lm}^{PS}><\psi_{lm}^{PS}\delta V_l(r)|}{<\psi_{lm}^{PS}|\delta V_l(r)|\psi_{lm}^{PS}>}.$$

The $\hat{V}_{NL}^{KB}$ operator is computationally rather inexpensive as l_{max}^{KB} is typically small. I usually use a $l_{max}^{KB} = l_{max} + 1$ [87] in SIESTA calculations, where ψ_{lm}^{PS} is the atomic pseudo-wavefunction and l_{max} is the maximum angular momentum used in the basis.

2.2.3 Orbital basis

In a periodic solid with an infinite number of electrons and ions, we use Bloch's theorem to expand electronic eigenfunctions in plane waves on the grid of reciprocal lattice vectors $\vec{G}$ as

$$\psi_{i,\,k}(\vec{r}) = e^{i\vec{k}\cdot\vec{r}}\left(\sum_{\vec{G}} c_{i,\,\vec{G}} e^{i\vec{G}\cdot\vec{r}}\right) = \sum_{\vec{G}} c_{i,\,\vec{k}+\vec{G}} e^{i(\vec{G}+\vec{k})\cdot\vec{r}}, \qquad (2.11)$$

where i denotes the state and $\vec{k}$ the Bloch wave vector.

The Fourier representation of $\psi_{i,\,k}$ is dominated by components with a low wave number $\vec{k} + \vec{G}$. Therefore, it is common practice to ignore high-frequency Fourier components, setting $c_{i,\,\vec{k}+\vec{G}} = 0$ if $E = (\hbar^2/2m)/|\vec{k}+\vec{G}|^2 > E_{cutoff}$. The value of E_{cutoff} determines the accuracy of the total energy. Since pseudopotentials suppress nodes in atomic wavefunctions, also the electronic wavefunctions in a solid are rather smooth and require a low value of E_{cutoff} for convergence.

The size of the plane wave basis set decided by the kinetic energy cutoff E_{cutoff} determines the size of Hamilton matrix. Finally the problem of dealing with an infinite number of electronic wave functions has been transformed into calculating a finite number of electronic wave functions at an infinite number of k-points within the finite Brillouin zone [82]. In most instances, sampling the Brillouin zone by a finite set of k-points instead of performing an integration over the Brillouin zone is the most convenient procedure.

Distinct from codes using a plane wave basis set, SIESTA has a lower requirement

on "smoothness" and uses localized numerical atomic orbitals (NAOs) as a basis. NAOs are strictly confined in space, but non-orthogonal. Still, the resulting Kohn-Sham and overlap matrices are sparse, enabling linear scaling of the computations. The level of confinement is defined by a quantity called "energy shift", corresponding to the energy increase associated with the localization of the orbital. The radial and angular flexibility of atomic orbitals can be increased by increasing the basis size (i.e. by changing what is called a single-ζ to a double-ζ and triple-ζ basis, with increasing number of basis functions, and by adding polarization orbitals with a higher angular momentum [93]). A basis set can be optimized by varying the basis size, the confinement range and the shape of the basis functions. I found the NAOs basis sets with double-ζ polarized orbitals (DZP) to provide dependable results for most systems studied here. Still, a localized basis set is always inferior to a plane-wave basis that is free of prejudice. Selecting an atomic orbital basis causes a degree of arbitrariness in terms of location of the basis functions and introduces basis-set superposition-errors (BSSE) due to the non-orthogonality of the basis. To limit those errors, we use the counterpoise method [94] and compare our results to more involved calculations using plane-wave basis sets.

2.2.4 Hamiltonian matrix elements

The standard Kohn-Sham one-electron operator may be written as

$$\hat{H}_{KS} = \hat{T}_0 + \sum_i \hat{V}_{NL}^{KB}(\vec{r} - \vec{R}_i) + \sum_i \hat{V}_{local}(\vec{r} - \vec{R}_i) + V_{Hartree}(\vec{r}) + V_{xc}(\vec{r}), \quad (2.12)$$

where $\hat{T}_0$ is the kinetic energy operator, R_i is the position of ion i, $\hat{V}_{NL}^{KB}$ and $\hat{V}_{local}$ are the nonlocal and local pseudopotentials of ion i, respectively, and $V_{Hartree}(\vec{r})$ and $V_{xc}(\vec{r})$ are the total Hartree and exchange-correlation potentials.

The Kohn-Sham Hamiltonian H_{KS} has eigenfunctions $\psi_i(\vec{r})$ with corresponding

eigenvalues ε_i. We can expand $\psi_i(\vec{r})$ in the orbital basis $\phi_\mu(\vec{r})$ as

$$\psi_i(\vec{r}) = \sum_\mu c_{i\mu} \phi_\mu(\vec{r}). \qquad (2.13)$$

Then, finding eigenfunctions and eigenvalues of H_{KS} is reduced to diagonalizing the matrix $\left(\hat{H}_{\mu\nu} - \varepsilon_i \hat{S}_{\mu\nu} \right)$. In the following, I describe the way to determine this matrix.

In a crystal, the potential $V_{eff}(\vec{r})$ is periodic and can be described as a sum of Fourier components,

$$V_{eff}(\vec{r}) = \sum_n V_{eff}(\vec{G}n) e^{i\vec{G}n \cdot \vec{r}}, \qquad (2.14)$$

where

$$V_{eff}(\vec{G}) = \frac{1}{\Omega_{cell}} \int_{\Omega_{cell}} V_{eff}(\vec{r}) e^{-i\vec{G} \cdot \vec{r}} d\vec{r} \qquad (2.15)$$

and where Ω_{cell} is the volume of the primitive unit cell. When plane-wave basis states $|\vec{q}>$ (or $\phi_q(\vec{r}) = e^{i\vec{q} \cdot \vec{r}}$) are used to expand $\psi_i(\vec{r})$, the matrix elements for the potential become

$$< \vec{q}\,'|V_{eff}(\vec{r})|\vec{q} >= \sum_n V_{eff}(\vec{G}n) \delta_{\vec{q}\,' - \vec{q}, \vec{G}_n}. \qquad (2.16)$$

If we define $\vec{q} = \vec{k} + \vec{G}_m$ and $\vec{q}\,' = \vec{k} + \vec{G}_{m'}$, we can rewrite the Kohn-Sham matrix as

$$\sum_{m'} \left(H_{m,m'}(\vec{k}) - \varepsilon_i(\vec{k}) \delta_{m,m'} \right) c_{i,m'}(\vec{k}) = 0, \qquad (2.17)$$

where

$$H_{m,m'}(\vec{k}) = \frac{\hbar^2}{2m_e} \left| \vec{k} + \vec{G}m \right|^2 \delta_{m,m'} + V_{eff}(\vec{G}m - \vec{G}_{m'}). \qquad (2.18)$$

The reciprocal space representation makes the calculation of the matrix elements equivalent to determining the Fourier components of the effective potential. The

kinetic energy terms contribute only diagonal elements to the Kohn-Sham matrix.

In SIESTA calculations, we distinguish in the calculation of matrix elements of the Kohn-Sham one-particle Hamiltonian (2.12) between elements that involve either two-center integrals or grid integrals, as described in the following.

2-center integrals

The matrix elements of the overlap matrix $S_{\mu\nu} = <\phi_\mu | \phi_\nu>$ are given by

$$S_{\mu\nu}(\vec{R}) \equiv \int \phi_\mu^*(\vec{r})\phi_\nu(\vec{r} - \vec{R})d\vec{r}. \tag{2.19}$$

The orbital wavefunctions ϕ_ν and ϕ_μ can be expanded in spherical harmonics as

$$\phi_\mu(\vec{r}) = \sum_{l=0}^{l_{max}} \sum_{m=-l}^{l} a_{lm}^\mu(r)Y_{lm}(\hat{r}), \tag{2.20}$$

where

$$a_{lm}^\mu(r) = \int_0^\pi \sin(\theta)d\theta \int_0^{2\pi} d\varphi Y_{lm}^*(\theta,\varphi)\phi_\mu(r,\theta,\varphi). \tag{2.21}$$

Using the Fourier transform $\phi_\mu(\vec{r}) = \frac{1}{(2\pi)^{3/2}} \int \phi_\mu(\vec{k})e^{i\vec{k}\cdot\vec{r}}d\vec{k}$ leads to an alternate expression in reciprocal space,

$$S_{\mu\nu}(\vec{R}) = \int \phi_\mu^*(\vec{k})\phi_\nu(\vec{k})e^{-i\vec{k}\cdot\vec{R}}d\vec{k}. \tag{2.22}$$

We can furthermore make use of expanding a plane wave as

$$e^{i\vec{k}\cdot\vec{R}} = \sum_{l=0}^{\infty} 4\pi i^l j_l(kR)Y_{lm}^*(\hat{k})Y_{lm}(\hat{R}), \tag{2.23}$$

where $j_l(kr)$ is the Bessel function, and expand

$$\phi_\mu(\vec{k}) = \sum_{l=0}^{l_{max}} \sum_{m=-l}^{l} b_{lm}^\mu(k) Y_{lm}(\hat{k}), \qquad (2.24)$$

with

$$b_{lm}^\mu(k) = \sqrt{\frac{2}{\pi}}(-i)^l \int_0^\infty r^2 dr j_l(kr) a_{lm}^\mu(r). \qquad (2.25)$$

Substituting expressions in Eq. (2.23) and (2.24) into Eq. (2.22) leads to

$$S_{\mu\nu}(\vec{R}) = \sum_{l=0}^{2l_{max}} \sum_{m=-l}^{l} \left[\sum_{l_\mu m_\mu, l_\nu m_\nu} G_{lm}^{l_\mu m_\mu, l_\nu m_\nu} S_l^{l_\mu m_\mu, l_\nu m_\nu}(R) \right] Y_{lm}(\hat{R}), \qquad (2.26)$$

with

$$G_{lm}^{l_\mu m_\mu, l_\nu m_\nu} = \int d\Omega Y_{l_\mu m_\mu}^*(\Omega) Y_{l_\nu m_\nu}(\Omega) Y_{lm}^*(\Omega), \qquad (2.27)$$

and

$$S_l^{l_\mu m_\mu, l_\nu m_\nu}(R) = 4\pi i^{l_\mu - l - l_\nu} \int_0^\infty k^2 dk j_l(kR) b_{l_\mu m_\mu}^{*\mu}(k) b_{l_\nu m_\nu}^\nu(k). \qquad (2.28)$$

The Gaunt coefficients $G_{lm}^{l_\mu m_\mu, l_\nu m_\nu}$, which express angular momentum conservation rules, can be calculated by recursion from Clebsch-Gordan coefficients and be stored once and for all [95]. The overlap coefficients $S_l^{l_\mu m_\mu, l_\nu m_\nu}(R)$ depend on the internuclear distance R and vanish for $R > (r_\mu^{cutoff} + r_\nu^{cutoff})$, where r_μ^{cutoff} denotes the confinement of the basis wavefunction $\phi_\mu(\vec{r})$.

The kinetic operator matrix elements $T(\vec{R})$ can be evaluated similarly to $S(\vec{R})$, except for including an additional factor $k^2/2$ within integral (2.28), as

$$T_l^{l_\mu m_\mu, l_\nu m_\nu}(R) = 4\pi i^{l_\mu - l - l_\nu} \int_0^\infty \frac{1}{2} k^4 dk j_l(kR) b_{l_\mu m_\mu}^{*\mu}(k) b_{l_\nu m_\nu}^\nu(k). \qquad (2.29)$$

23

The angular integral in Eq. (2.27) is performed by a Gaussian quadrature and the radial integrals in Eq. (2.25), (2.28) and (2.29) are calculated using fast Fourier transform (FFT) along the radial direction.

Grid integrals

Matrix elements of the remaining three terms in the Kohn-Sham Hamiltonian (2.12) can be calculated on a real-space grid. The grid spacing is controlled by the energy cutoff in the plane-wave expansion of the potential, called "MeshCutoff" [78] in SIESTA code. We use this real-space grid to evaluate matrix elements of the potential

$$\hat{V}'(\vec{r}) = \sum_i \hat{V}_{local}(\vec{r} - \vec{R}_i) + V_{Hartree}(\vec{r}) + V_{xc}(\vec{r}). \qquad (2.30)$$

To eliminate the large computational cost associated with the long range of the local pseudopotential $\hat{V}_{local}(\vec{r} - \vec{R}_i)$, we rearrange the potential $\hat{V}'$ by introducing neutral-atom potentials [96] as

$$V_{NA}(\vec{r} - \vec{R}_i) = V_{local}(\vec{r} - \vec{R}_i) + \int d\vec{r}\,' \frac{n_{atom}(\vec{r} - \vec{R}_i)}{|\vec{r} - \vec{r}\,'|}. \qquad (2.31)$$

This new potential is constructed by populating the localized basis functions with appropriate valence charges to cancel the pseudonuclear charge inside the radius r_{cutoff}. Consequently, $V_{NA}(\vec{r})$ vanishes for $r > r_{cutoff}$, which greatly reduces the number of non-zero matrix elements [96]. The difference $\delta n(\vec{r})$ between the self-consistent electron density $n(\vec{r})$ and $n_{atom}(\vec{r})$ reflects formation of covalent bonds and is determined by a "Hartree-like" potential $\delta V_{Hartree}(\vec{r})$, obtained by solving the Poisson equation

$$\delta n(\vec{r}) = -\frac{1}{4\pi e} \nabla^2 \delta V_{Hartree}(\vec{r}). \qquad (2.32)$$

Using the above expressions, the potential $V'(\vec{r})$ can be rewritten as

$$\hat{V}'(\vec{r}) = \sum_i V_{NA}(\vec{r} - \vec{R}_i) + \delta V_{Hartree}(\vec{r}) + V_{xc}(\vec{r}). \qquad (2.33)$$

Following the initial guess of the charge density $n(\vec{r})$ on each grid point $\vec{r}$, we evaluate $\delta V_{Hartree}(\vec{r})$ by solving the Poisson equation with the help of an FFT. We then evaluate $V_{xc}(\vec{r})$ using LDA or GGA and determine $\sum_i V_{NA}(\vec{r} - \vec{R}_i)$. The sum of these terms yields the desired value of $V'(\vec{r})$ on the grid. To obtain the matrix element $H_{\mu\nu} = <\phi_\mu|H_{KS}|\phi_\nu>$ of the Kohn-Sham Hamiltonian, we sum up the contributions $\phi_\mu^*(\vec{r})V'(\vec{r})\phi_\nu(\vec{r})\Delta\vec{r}^3$ over the unit cell size. We need to point out that the $\vec{G} = 0$ component is not determined using FFT when determining potentials such as the Hartree potential in periodic charge neutral systems, but rather using sum rules. Charge neutrality must be enforced to avoid divergence of the $\vec{G} = 0$ component.

2.3 Total energy

Once we determine the eigenvalues and eigenfunctions of the Kohn-Sham Hamiltonian, we may continue with the evaluation of the total energy,

$$E_{total} = T[n] + E_{ext} + E_{Hartree} + E_{xc} + E_{II}. \qquad (2.34)$$

Here, E_{II} describes inter-ion interaction

$$E_{II} = \frac{1}{2} \sum_{\vec{R},m} \sum_{\vec{R}',m'}{}' \frac{Z_m Z_{m'}}{\left|\vec{R} + \vec{\tau}_m - \vec{R}' + \vec{\tau}_{m'}\right|}, \qquad (2.35)$$

where $\vec{R}$ is the Bravais lattice vector, $\vec{\tau}$ is the atomic positions within the unit cell and Z_m is the valence charge of ion at position $\vec{R}$ [72, 97].

Using Eq.(2.9) we evaluate the kinetic energy functional as

$$T[n] = \sum_i \langle \psi_i | \epsilon_i - V_{KS} | \psi_i \rangle. \tag{2.36}$$

Combining Eqs.(2.36) and (2.34), we obtain the total energy expression

$$E_{total} = \sum_i \epsilon_i - \frac{1}{2} \int d^3r d^3r' \frac{n(\vec{r})n(\vec{r}\,')}{|\vec{r} - \vec{r}\,'|} + \int d^3r [\epsilon_{xc}(\vec{r}) - V_{xc}(\vec{r})]n(\vec{r}) + E_{II}. \tag{2.37}$$

where $E_{xc} = \int d^3r \epsilon_{xc}(\vec{r})n(\vec{r})$.

For an infinite periodic system, we will again benefit from performing the integration in reciprocal space, using Fourier transforms of the quantities of interest. We find

$$E_{total} = \sum_i \epsilon_i - \frac{\Omega_c}{2} \sum_{\vec{G} \neq 0} n^*(\vec{G}) \frac{8\pi n(\vec{G})}{G^2} + \Omega_c \sum_{\vec{G}} [\epsilon_{xc}(\vec{G}) - V_{xc}(\vec{G})]n^*(\vec{G}) + E_{II},$$

$$\tag{2.38}$$

where Ω_c is the volume of the unit cell. Here, we have excluded the $\vec{G} = 0$ components, as they would cause divergence in the numerical evaluation of E_{total}. Physically, the divergence in the Hartree energy is compensated by a divergence in E_{II} and external potential energy. These diverging terms, given by

$$E_{total,\,div} = \lim_{\vec{G} \to 0} \Omega_c \left[\frac{1}{2} \frac{8\pi n(\vec{G})}{G^2} + \sum_m v_{ext}^m(\vec{G}) \right] n(\vec{G}) + \frac{1}{2} \sum_{\vec{R},m} \sum_{\vec{R}',m'} {}' \frac{Z_m Z_{m'}}{\left| \vec{R} + \vec{\tau}_m - \vec{R}' - \vec{\tau}_{m'} \right|},$$

$$\tag{2.39}$$

are treated separately.

First, we note that the $v_{ext}^m(\vec{G})$ and $n(\vec{G})$ terms can be expanded close to $\vec{G} = 0$ as

$$v_{ext}^m(\vec{G}) = -\frac{8\pi Z_m}{\Omega_c G^2} + \alpha_m + O(\vec{G}), \tag{2.40}$$

26

where Z_m and α_m are expansion coefficients and

$$n(\vec{G}) = \frac{\sum_m Z_m}{\Omega_c} + \beta G^2 + O(\vec{G}). \qquad (2.41)$$

Substituting the expressions in Eqs.(2.40) and (2.41) back into Eq.(2.39), and dropping negligible higher-order terms, we get for the $\vec{G} = 0$ contribution to E_{total}

$$E_{total,\,div} = \lim_{\vec{G} \to 0} \Omega_c \left[\frac{1}{2} \frac{8\pi n(\vec{G})}{G^2} - \frac{8\pi \sum_m Z_m}{\Omega_c G^2} + \sum_m \alpha_m \right] n(\vec{G})$$
$$+ \frac{1}{2} \sum_{\vec{R},m} \sum_{\vec{R}',m'} {}' \frac{Z_m Z_{m'}}{\left| \vec{R} + \vec{\tau}_m - \vec{R}' - \vec{\tau}_{m'} \right|}. \qquad (2.42)$$

This expression can be further simplified to

$$E_{total,\,div} = \sum_m \alpha_m \sum_{m'} Z_{m'} + \frac{1}{2} \sum_{\vec{R},m} \sum_{\vec{R}',m'} {}' \frac{Z_m Z_{m'}}{\left| \vec{R} + \vec{\tau}_m - \vec{R}' - \vec{\tau}_{m'} \right|} - \frac{1}{2} \frac{8\pi (\sum_m Z_m)^2}{\Omega_c G^2}.$$
$$(2.43)$$

The last two terms include the diverging Hartree, external potential and inter-ion Coulomb repulsion energies. They are treated using a technique due to Ewald [98], which accelerates convergence by treating a charge neutral sub-system in reciprocal space and performing the remainder in real space using the identity

$$\sum_{m,m'} \frac{1}{\left| \vec{R} + \vec{\tau}_m - \vec{R}' + \vec{\tau}_{m'} \right|} = \frac{2}{\sqrt{\pi}} \sum_{m,m'} \int_\eta^\infty dx \; e^{-\left| \vec{R} + \vec{\tau}_m - \vec{R}' - \vec{\tau}_{m'} \right|^2 x^2}$$
$$+ \frac{2\pi}{\Omega_c} \sum_{\vec{G}} \int_0^\eta dx \; e^{-\frac{|\vec{G}|^2}{4x^2}} e^{i(\vec{R} - \vec{R}') \cdot \vec{G}} \frac{1}{x^3}. (2.44)$$

Ewald formulates the charge neutral sub-system by superposing a virtual compensative Gaussian charge distribution of width η at each ion, which renders the

27

system charge neutral. This convergent energy sum is evaluated in reciprocal space. The virtual charge distribution is subsequently subtracted and evaluated in real space with accelerated convergence for a finite value of η. Ewald's final expression for the total energy of the ions is [99]

$$
E_{II} = \frac{1}{2} \sum_{m,\,m'} Z_m Z_{m'} \sum_{l} \frac{erfc(\eta x)}{x} - \frac{2\eta}{\sqrt{\pi}} \delta_{m,\,m'}
$$

$$
+ \frac{4\pi}{\Omega_c} \sum_{\vec{G} \neq 0} \frac{1}{|\vec{G}|^2} \, e^{-\frac{|\vec{G}|^2}{4\eta^2}} \cos[(\vec{R} - \vec{R}') \cdot \vec{G}] - \frac{\pi}{\eta^2 \Omega_c}, \qquad (2.45)
$$

independent of η. In practice, the value of η is varied to minimized computational effort both in real and in reciprocal space.

Chapter 3

Interplay between structure and magnetism in $Mo_{12}S_9I_9$ nanowires

The following discussion is closely related to a publication by Teng Yang, Shinya Okano, Savas Berber, and David Tománek, Phys. Rev. Lett. **96**, 125502 (2006) [35].

3.1 Introduction

One of the major challenges in the emerging field of molecular electronics is to identify conducting nanostructures with desired electronic properties, which are stable and easy to manipulate. Due to their high stability and favorable electronic properties [1], carbon nanotubes [2] have been discussed extensively as promising candidates for molecular electronics applications. A major drawback is our current inability to synthesize or to isolate nanotubes with a given diameter and chiral angle, which determine their metallic or semiconducting nature. Moreover, single-wall carbon nanotubes are hard to isolate from stable bundles, which form spontaneously during synthesis [3]. In this respect, recently synthesized nanowires based on Mo chalcohalides, such as $Mo_{12}S_9I_9$, seem to offer several advantages by combining uniform metallic behavior, atomic-scale perfection and easy dispersability [5, 6].
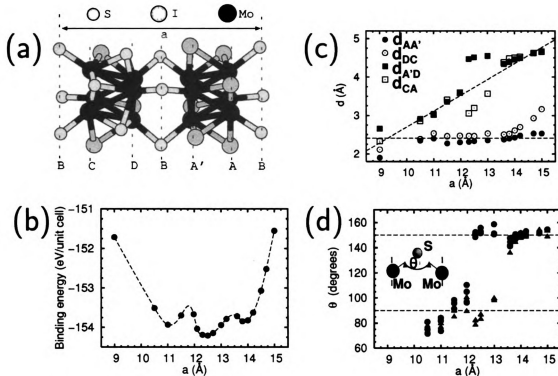
Figure 3.1: Structural properties of $Mo_{12}S_9I_9$ nanowires. (a) Atomic arrangement within a unit cell. Planes normal to the wire axis are denoted by A, A', B, C, D. (b) Binding energy as a function of the lattice constant a. (c) Optimized inter-plane distances as a function of a. (d) Optimum values of the Mo-S-Mo bond angle Θ as a function of a. Values in the two sulphur bridges per unit cell are distinguished by different symbols. Dashed lines in (b-d) are guides to the eye.

Using *ab initio* density functional calculations, I study the suitability of $Mo_{12}S_9I_9$ nanowires as potential building blocks of electronic nanocircuits. In terms of binding energy per atom, I find these nanowires to be almost as stable as carbon nanotubes. The nanowire skeleton consists of rigid, functionalized Mo octahedra, connected by flexible, bi-stable sulphur bridges. I find this structural flexibility to translate into an unusual capability to stretch up to $\approx 20\%$ at virtually no energy cost, as a nanostructured counterpart of an accordion. My calculations suggest that the nanowires change from conductors to narrow-gap magnetic semiconductors in one of their structural isomers.

To gain insight into structural and electronic properties of these unusual systems,

I optimized the geometry of infinite $Mo_{12}S_9I_9$ nanowires as well as selected structural building blocks using density functional theory (DFT). I used the Perdew-Zunger [100] form of the exchange-correlation functional in the local density approximation (LDA) to DFT, as implemented in the SIESTA code [87]. The behavior of valence electrons was described by norm-conserving Troullier-Martins pseudopotentials [89] with partial core corrections in the Kleinman-Bylander factorized form [92]. I used a double-zeta basis, including initially unoccupied $Mo5p$ orbitals. I arranged the nanowires on a tetragonal lattice, with one side of the unit cell given by the lattice constant a. The other sides of the unit cell were taken to be 19.7 Å long, about twice the nanowire diameter, to limit inter-wire interaction. I sampled the rather short Brillouin zone of these 1D structures by 6 k-points [101]. The charge density and potentials were determined on a real-space grid with a mesh cutoff energy of 150 Ry, which was sufficient to achieve a total energy convergence of better than 2 meV/atom during the self-consistency iterations.

Magnetic ordering in the nanostructures was investigated using the Local Spin Density Approximation (LSDA) within the SIESTA code [87]. Even though LSDA may be considered less rigorous and dependable than LDA, I use it here as a systematic way to estimate net magnetic moments and exchange splitting in 1D nanowires and finite segments of these systems.

3.2 Structural and Electronic Properties

3.2.1 Structural Properties

With 30 atoms per unit cell, corresponding to 84 degrees of freedom, global structure optimization is a formidable task. The initial experimental structure determination, based on Atomic-Resolution Transmission Electron Microscopy (TEM) and X-ray diffraction data [41], provided me with a useful idea of the equilibrium

structure. In spite of the significant energy gain of 50 eV with respect to the experimental structure during the initial structure optimization, the calculated atomic arrangement within the $Mo_{12}S_9I_9$ unit cell, depicted in Fig. 3.1(a), was found to lie very close to the experimental structure.

I found it useful to assign atoms to planes normal to the wire axis. I label these atomic layers A, A', B, C, and D in Fig. 3.1(a). Layers A and A' are structurally identical in terms of atomic arrangement, but rotated by 180° with respect to each other. Mo octahedra, decorated by S and I atoms, form the structural motif of the AA' and CD bilayers. As I discuss later on, these bilayers can be thought of as rigid blocks, connected by bridges formed of three S atoms, denoted as layer B.

My results for the binding energy of the system as a function of the lattice constant a are summarized in Fig. 3.1(b). For lattice constants other than the experimental value [41, 102] $a_{expt} = 11.97$ Å, the initial structures used in the optimization were based on uniformly expanded or compressed nanowires, subject to random distortions, or structures optimized using semiempirical force fields. For a given value of the lattice constant, I considered a structure as optimized when different starting geometries resulted in the same structural arrangement.

The cohesive energy of the 30-atom unit cell, displayed in Fig. 3.1(b), translates into a formidable average binding energy exceeding 5 eV per atom. I found that inclusion of $Mo5p$ orbitals provided a net stabilization of the system, but did not modify much the interatomic forces or equilibrium geometries. As indicated by my LSDA calculations, additional structure stabilization occurred due to magnetic ordering for selected geometries.

Most intriguing in these results is the presence of multiple structural minima. Since structures with optimum lattice constants $a = 11.0$ Å, 12.3 Å and 13.8 Å are very close in energy, a distribution of bonding configurations along the chain axis will likely occur in order to maximize configurational entropy, resulting in the loss

of long-range order. Identifying structures with very similar energies in a range of lattice constants also implies the possibility to stretch the nanowire by 20% at virtually no energy cost, similar to an accordion. The remarkable ability of $Mo_6S_xI_y$ to expand easily by nearly 30% has been previously noted in Atomic Force Microscope experiments on closely related systems [103]. This uncommon flexibility of an inorganic nanowire may explain in retrospect, why the observed lattice constant [41, 102] $a_{expt} = 11.97$ Å may differ from the structural minima in Fig. 3.1(b).

Trying to understand the origin of the unusual elastic behavior of $Mo_{12}S_9I_9$ nanowires, I first investigated the inter-layer spacings as a function of the lattice constant. Analysis of my data, presented in Fig. 3.1(c), suggests that interatomic spacing within AA' and CD bilayers changes very little with increasing lattice constant. The motif of the bilayers is formed of six Mo atoms in near-octahedral arrangement, with Mo-Mo bond lengths close to 2.6 Å within the layers and 3.0 Å along the wire axis. In the following, I consider these decorated octahedra as rather rigid building blocks of the nanowires. I found the decoration order by I and S atoms to be non-random, since an interchange of these atoms within the unit cell raised the total energy by more than 0.5 eV.

Most importantly, results in Fig. 3.1(c) suggested that virtually all structural changes are accommodated by the sulfur bridges, which form the A'-D and C-A connections. I found that most changes occurred in the Mo-S-Mo bond angle Θ, whereas the Mo-S bond lengths remained nearly constant. My results for Θ as a function of the lattice constant a, shown in Fig. 3.1(d), suggest that the expectation values of Θ do not change uniformly, but rather group around 90° and 150°. In the following, I will call the corresponding structural arrangements "short" and "long" bridges. Similar metastable structures have also been reported for 1D wires of group IV elements [104]. In the case of isolated sulphur chains and S_3 molecules, I have also observed a preference for similar bond angles as in Fig. 3.1(d). In analogy with

similar preferential bond angles found in different allotropes of C and Si, I associate the short bridge with sp^3 and the long bridge with sp^2 hybridization.

In the case of $Mo_{12}S_9I_9$ nanowires, I find two such sulphur bridges in each unit cell. Local minima in the cohesive energy, plotted in Fig. 3.1(b), are found at the lattice constants $a = 11.0$ Å, 12.3 Å, and 13.8 Å. The fact that only three minima are found, and that $a = 12.3$ Å is close to the average of the other two lattice constants, supports my conclusion that there are only two types of S-mediated bonds connecting the blocks, which are decoupled within the unit cell. The three local minima in Fig. 3.1(b) thus correspond to a short-short, short-long (or long-short), and a long-long bridge configuration.

To verify that the optimum structures are not influenced by the constraints of a periodic lattice with a fixed unit cell size, I independently optimized the structure of the Mo-based building blocks with the proper decoration by S and I atoms, with sulphur bridge trimers attached at both sides. With the exception of the bridge atoms, which changed their positions, I found the atomic arrangement in $Mo_6S_6I_6$, modelling the AA' bilayer, and $Mo_6S_9I_3$, modelling the CD bilayer, to lie close to globally optimized nanowire structures, discussed in Fig. 3.1.

Comparing the binding energies of the bilayer clusters, $E_{coh}(AA') = -81.0$ eV and $E_{coh}(CD) = -89.2$ eV, I conclude that the binding of sulphur atoms to the cluster is significantly stronger than that of iodine atoms. I also found that the isolated CD cluster acquires a net magnetic moment $\mu(CD) = 1.00~\mu_0$. As I discuss in the following, not only finite nanostructures with dangling bonds, but also infinite nanowires may develop a net magnetic moment.

3.2.2 Electronic structure

I found the infinite $Mo_{12}S_9I_9$ nanowires to generally behave as conductors in the lattice constant range 9 Å$< a < 15$ Å, with the exception of the metastable structure

34
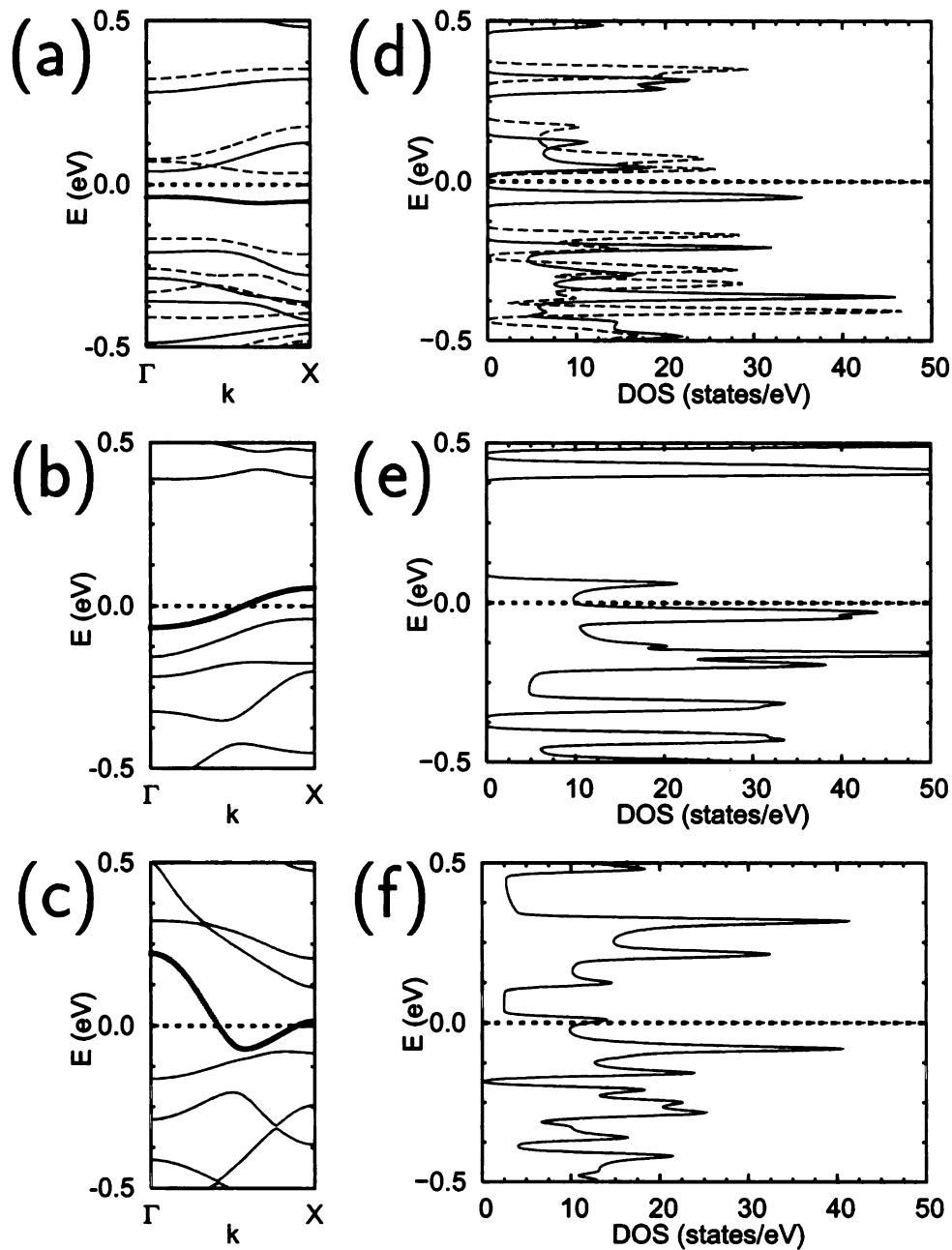
Figure 3.2: Electronic band structure $E(k)$ of $Mo_{12}S_9I_9$ nanowires with lattice constants (a) $a = 11.0$ Å, (b) $a = 12.3$ Å, and (c) $a = 13.8$ Å. Solid lines represent majority and dashed lines minority spin bands. Bands crossing the Fermi level are emphasized by heavy lines. Densities of states of nanowires with (d) $a = 11.0$ Å, (e) $a = 12.3$ Å, and (f) $a = 13.8$ Å, convoluted with 0.01 eV wide Gaussians. The Fermi level lies at $E_F = 0$.

at $a{\approx}11$ Å discussed below. In Fig. 3.2 I present results for the electronic structure at $a = 11.0$ Å, 12.3 Å, and 13.8 Å, corresponding to the equilibrium structures indicated in Fig. 3.1(b). The interactions along the nanowire, causing band dispersion, depend crucially on the hybridization near the sulphur bridges. As discussed earlier, changing the lattice constant does not affect interatomic distances, but rather modifies the Mo-S-Mo bond angle Θ, thus changing the hybridization of directional orbitals. An increase in band dispersion, caused by increased hybridization, may be counter-acted by band repulsion in complex systems.

The interplay between lattice constant and band structure is depicted in Figs. 3.2(a-c). My results in Figs. 3.2(b-c) suggest that the metallic character of the wires derives from a rather dispersionless band, which crosses the Fermi level. As shown in Fig. 3.2(a), this band becomes very flat and even changes its slope at $a{\approx}11.0$ Å due to the changed hybridization associated with Mo-S-Mo bond bending. Consequently, the density of states develops a peak at E_F, which subsequently splits due to a magnetic instability, as shown in Fig. 3.2(d). This splitting opens up a fundamental gap of 73 meV, accompanied by a net magnetic moment of 1.00 μ_0 per unit cell. This magnetic moment is obtained using the LSDA densities of states as $\mu = \int_{-\infty}^{E_F} dE(n_{\uparrow}(E) - n_{\downarrow}(E))$. At other lattice constants, the dispersion of this partly filled band increases, as seen in Figs. 3.2(b) and (c). Consequently, as seen in Figs. 3.2(e) and (f), the density of states at the Fermi level is lower, suppressing the magnetic instability.

A more detailed discussion of the electronic structure in the system with a net magnetic moment, at $a = 11.0$ Å, is presented in Fig. 3.3. The charge distribution in the $Mo_{12}S_9I_9$ nanowire, depicted in Fig. 3.3(a), is very similar to the superposition of atomic charge densities. This is better seen in Fig. 3.3(b), which displays the charge redistribution within the system with respect to isolated atoms, given by $\Delta\rho(\mathbf{r}) = \rho(\mathbf{r}) - \Sigma\rho_{atom}(\mathbf{r})$. As expected based on electronegativity differences, I observe a
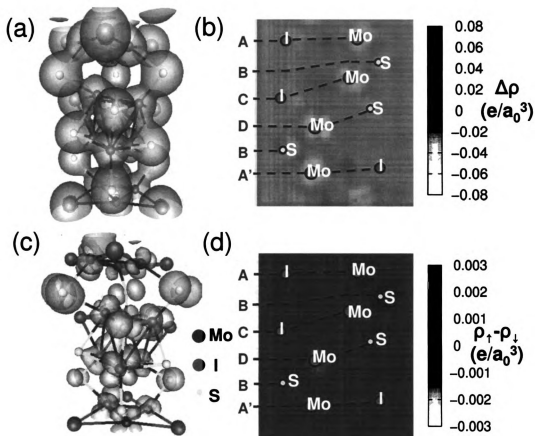
Figure 3.3: Contour plots depicting the charge distribution in a $Mo_{12}S_9I_9$ nanowire at $a = 11.0$ Å. (a) Total charge density contour at $\rho = 0.05$ el/a_0^3. (b) Difference charge density $\Delta\rho(\mathbf{r})$, indicating regions of charge depletion and excess with respect to the superposition of isolated atoms. (c) $\rho = 1.0 \times 10^{-3}$ el/a_0^3 charge density contour associated with states close to the Fermi level, $E_F - 0.05$ eV$< E < E_F + 0.05$ eV. (d) Difference spin density $\rho_\uparrow(\mathbf{r}) - \rho_\downarrow(\mathbf{r})$, showing regions of excess majority spin $\uparrow$. Contour plots (b) and (d) are depicted in a plane, which contains the wire axis.

small amount of charge, stemming mostly from Mo4d orbitals, to be transferred to the region within the Mo octahedra, in particular to Mo-Mo bonds and sulphur atoms. The decorating iodine atoms do not experience a change in their charge distribution due to their presence in the nanowire structure. More interesting than information about all populated levels is the spatial distribution of states close to the Fermi level, which form the valence and conduction band. My results, shown in Fig. 3.3(c), suggest that these states are rather delocalized. Together with the band structure results of Fig. 3.2, I conclude that the nanowires considered here should be conducting at room temperature, in agreement with experimental observations [5, 6].

Spatially resolved information about the magnetic structure of the nanowire at $a = 11.0$ Å is presented in Fig. 3.3(d). Associating up-spin with the majority and down-spin with the minority states, the plotted quantity $\rho_\uparrow(\mathbf{r}) - \rho_\downarrow(\mathbf{r})$ allows us to identify spatial regions with a net magnetic moment. Based on the results in Fig. 3.3(d) and a set of 3D spin density contours, not shown here, I find the majority spin to be localized mostly on the bridging sulphur atoms, in their non-bonding $2p$ orbitals normal to the wire axis, and to a smaller degree on adjacent Mo atoms.

Since magnetism occurs in selected structural isomers of the infinite $Mo_{12}S_9I_9$ nanowires as well as in isolated building blocks, I expect the possibility of modifying the magnetic structure by locally stretching or expanding the nanowires. Since such structural changes may be induced locally at negligible energy cost, various magnetic patterns could possibly be obtained by mechanical manipulation of $Mo_{12}S_9I_9$ nanowires, possibly using an Atomic Force Microscope. Since magnetic ordering will likely affect spin transport in these systems, $Mo_{12}S_9I_9$ nanowires may be viewed as spin valves, which could change their state by applying local stress.

3.3 Summary

I note that the overall metallic behavior of $Mo_{12}S_9I_9$ nanowires is rather unusual among chalcogenide structures. Significant interest has been devoted in the past to the ability of layered semiconductors, such as MoS_2, to form fullerene- and nanotube-like structures [105, 106, 107]. Similar to their bulk counterparts, MoS_2 nanotubes were found to be semiconducting, unless intercalated with iodine to enhance conductance [108, 109]. MoS_2-based fullerenes and nanotubes, often containing iodine, were noted in particular for their favorable tribological properties [105, 107, 39]. At other stoichiometries, such as $Mo_6S_3I_6$ or $Mo_6S_4I_5$, self-assembled nanowires have been reported to form with either semiconducting or semi-metallic behavior [20, 21]. In the particular $Mo_{12}S_9I_9$ stoichiometry studied here, the rich behavior of molybdenum chalcogenides is complemented by new properties, such as high structural flexibility, metal-semiconductor transition, and magnetism. I propose to use these systems as unique building blocks in hierarchically assembled nanostructured electronic circuits.

Chapter 4

Unique structural and transport properties of molybdenum chalcohalide nanowires

The following discussion is closely related to a publication by Igor Popov, Teng Yang, Savas Berber, Gotthard Seifert and David Tománek, Phys. Rev. Lett. **99**, 085503 (2007) [110].

4.1 Introduction

Chalcohalides of molybdenum and other transition metals are known to form stable, intriguing 2- and 1-dimensional structures [7] with an unusual combination of electronic properties [8] including good conductance, superconductivity, magnetism, and nonlinear polarizability. These layered or filamentous substances are known as catalysts [9] and, to a much larger degree, as excellent solid lubricants [10, 11, 9]. Their potential to become unique building blocks of nano-devices has barely been noticed so far [9], in stark contrast to popular carbon nanotubes [12]. Recent progress in the synthesis of $Mo_xS_yI_z$ nanowires [13] suggests that these monodisperse, self-

supporting nanostructures may nicely complement carbon nanotubes by avoiding their shortcomings such as a strong dependence of conductivity on the nanotube structure and difficulty to separate bundled tubes [12].

Here I combine *ab initio* density functional theory [76, 77] and quantum transport calculations based on the nonequilibrium Green's function formalism [111, 112] to compare structural, electronic, and transport properties of $Mo_6S_{6-x}I_x$ nanowires (NWs) to those of carbon nanotubes (CNTs). I find systems with $x = 2$ to be particularly stable and rigid, with their electronic structure and conductance close to that of metallic $(13, 13)$ single-wall carbon nanotubes. $Mo_6S_{6-x}I_x$ nanowires are conductive irrespective of their structure and capable of forming ideal contacts to Au leads through thio-groups. Due to the weak inter-wire interaction, $Mo_6S_{6-x}I_x$ systems should be more easily separable than carbon nanotubes.

As mentioned before, chalcogenide compounds containing Mo and S have been studied for a long time [7, 14]. Whereas the best known allotropes, including MoS_2, are insulating and form layered compounds, more interesting structures often occur at lower sulfur concentrations. Well known are Chevrel phases, characterized as cluster compounds with Mo_6S_8 subunits, furthermore finite clusters with a similar structure, and needle-like quasi-1D compounds [15]. All these interesting structures necessitate the presence of metal counter-ions for their synthesis. Besides providing structural stability, the main role of the counter-ions is to transfer electrons into the chalcogenide substructures [16, 17], thereby forming an ionic crystal [18]. In their most stable electronic configuration, many of these compounds contained $(Mo_6S_6)^{2-}$ building blocks[14].

The idea behind this work is to study the possibility of stabilizing Mo-based nanowires by substituting the divalent sulfur by a monovalent halogen (I) with a similar electronegativity. In this way, the "magic" electronic configuration could be preserved, while maintaining a covalent character of the system and avoiding the for-

41

mation of an ionic crystal, where electron correlations would dominate the electronic structure. In the following, I study the properties of $Mo_6S_{6-x}I_x$ nanowires, where iodine was used to substitute for sulfur.

4.2 Structural and Electronic Properties

4.2.1 Structural and Chemical Stability

To gain insight into structural and electronic properties of the proposed systems, I optimized the geometry of infinite $Mo_6S_{6-x}I_x$ nanowires for $x = 0 - 6$ using density functional theory (DFT). I used the Perdew-Zunger [100] form of the exchange-correlation functional in the local density approximation (LDA) to DFT, as implemented in the SIESTA code [87]. The behavior of valence electrons was described by norm-conserving Troullier-Martins pseudopotentials [89] with partial core corrections. I used a double-zeta basis, including initially unoccupied $Mo5p$ orbitals.

The numerical results were obtained for the primitive unit cell of length a, containing 12 atoms, depicted in Fig. 4.1(a). For selected structures, I also compared my results to those for a double unit cell with 24-atoms. To describe isolated nanowires while using periodic boundary conditions, I arranged them on a tetragonal lattice with a large inter-wire separation of 20 Å. I sampled the rather short Brillouin zone of these 1D structures by at least 8 k-points. The charge density and potentials were determined on a real-space grid with a mesh cutoff energy of 150 Ry, which was sufficient to achieve a total energy convergence of better than 2 meV/atom during the self-consistency iterations.

To accelerate the global structure optimization of the nanowires with 36-72 degrees of freedom per unit cell, I first explored the configurational space and pre-optimized the systems using the faster density functional based tight binding (DFTB) method [113, 114], which had been used successfully to describe the deformation of
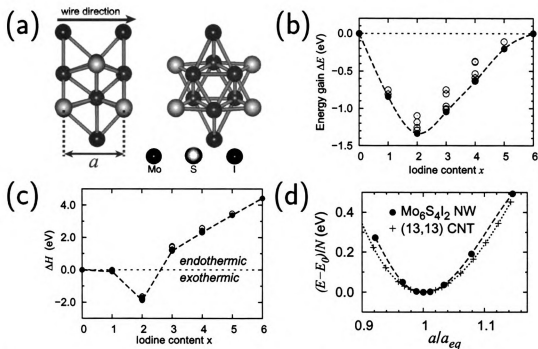
Figure 4.1: (a) Schematic structure of a $Mo_6S_{6-x}I_x$ nanowire in side and end-on view. (b) Energy gain $\Delta E(x)$ with respect to the average binding energy and (c) energy $\Delta H(x)$ of the substitution reaction in Eq. (4.1) leading to the formation of a $Mo_6S_{6-x}I_x$ nanowire as a function of composition. Among the data points for all structural isomers (○), the most stable structures are identified by the solid circles (●). (d) Deviation from the equilibrium binding energy E_0 as a function of the relative unit cell size a/a_{eq}, for a segment of the "magic" $Mo_6S_4I_2$ nanowire containing N Mo atoms, and for an N-atom segment of the $(13,13)$ carbon nanotube.

MoS_2 layers to tubular structures [115].

The optimized structure of $Mo_6S_{6-x}I_x$ nanowires, shown in Fig. 4.1(a), consists of a Mo backbone decorated by S and I ligands. The Mo core structure is formed by Mo trimers of alternating orientation forming a chain. There is one Mo_6 octahedron per unit cell, surrounded by $(6-x)$ sulfur atoms and x iodine atoms. For each value of x I performed an exhaustive isomer search and a global structure optimization. In general, I find the Mo-Mo bond length to increase from ≈ 2.6 Å when close to sulfur to ≈ 2.7 Å when close to the larger iodine. Introduction of iodine also causes an increase of the equilibrium lattice constant from $a_{eq}(Mo_6S_6) = 4.34$ Å to $a_{eq}(Mo_6I_6) = 4.55$ Å.

43

I find $Mo_6S_{6-x}I_x$ nanowires to be rather stable, with an average binding energy per atom ranging from 5.0 eV in Mo_6I_6 to 6.3 eV in Mo_6S_6 with respect to isolated atoms. The nanowires thus rival the stability of graphite with 7.3 eV/atom, and the slightly less stable carbon nanotubes. Changing the iodine content x in $Mo_6S_{6-x}I_x$ nanowires, I could naïvely expect the binding energy E to vary linearly between that of Mo_6S_6 and Mo_6I_6, showing no dependence on the particular structural isomer. In reality, deviations from this linear behavior [116], depicted as ΔE in Fig. 4.1(b), are substantial, suggesting that the stability of the various structural isomers at a particular composition varies by up to a large fraction of an eV. Focussing on the most stable isomers, I find a general tendency to selectively stabilize particular chalcohalide stoichiometries, such as $Mo_6S_4I_2$. As I will show below, this "magic" composition optimizes the electronic configuration of the building blocks to agree with the optimum charge state identified above using heuristic arguments.

Among the many structural isomers of $Mo_6S_{6-x}I_x$, I generally found structures with the largest separation between iodine atoms to be most stable. When increasing the variational freedom in the arrangement of iodine atoms by doubling the unit cell size, I identified geometries that further stabilize the structures by providing energy gain per unit cell ranging from 0.09 eV for $x = 1$ to 0.29 eV for $x = 3$.

The selectivity of a possible synthesis pathway becomes apparent, when studying the reaction energy ΔH of the substitution reaction

$$Mo_6S_6 + \frac{x}{2}I_2 \xrightarrow{\Delta H} Mo_6S_{6-x}I_x + \frac{x}{8}S_8 \,, \qquad (4.1)$$
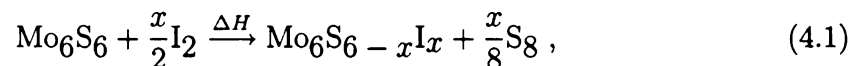
depicted in Fig. 4.1(c). Clearly, substitution of sulfur in Mo_6S_6 by gas-phase iodine is only exothermic for the "magic" iodine content $x = 2$.

In the following, I will compare various properties of $Mo_6S_{6-x}I_x$ nanowires to those of carbon nanotubes. As will become clear later on, the electronic structure of
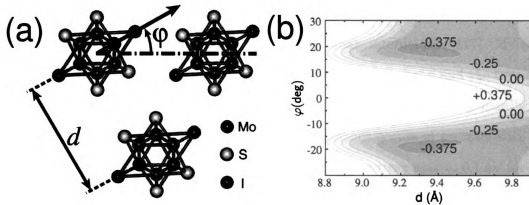
Figure 4.2: (a) Structure of $Mo_6S_4I_2$ nanowires arranged on a simple hexagonal lattice in a plane normal to the wire axes. (b) Contour plot of the nanowire binding energy in this lattice as a function of the wire orientation φ and separation d. The energy is given in eV per formula unit.

the chalcohalide nanowires matches well that of a conducting $(13, 13)$ carbon nanotube with a diameter of 17.6 Å. The equilibrium unit cell size $a_{eq}(13, 13) = 2.46$ Å of the armchair nanotube is about half the value of the "magic" nanowire, $a_{eq}(Mo_6S_4I_2) = 4.45$ Å.

The axial stiffness of a $Mo_6S_4I_2$ nanowire in comparison to that of a $(13, 13)$ carbon nanotube can be inferred from Fig. 4.1(d). I feel that in a fair comparison between the different systems, the energy investment upon axial strain should be normalized by the number of Mo backbone atoms in the nanowire and number of C atoms in the nanotube. Inspection of my results in Fig. 4.1(d) suggests that the high axial stiffness, based on the above definition, is nearly the same in the two systems. Thus, the $Mo_6S_4I_2$ nanowire differs significantly in its rigidity from the accordion-like behavior identified recently in the "floppy" $Mo_6S_{4.5}I_{4.5}$ nanowire [35].

4.2.2 Dispersability

Contrasting with the high stability and axial stiffness of the $Mo_6S_4I_2$ nanowires is their lateral inter-wire interaction, discussed in Fig. 4.2. I calculated the binding

energy of straight nanowires on a simple hexagonal lattice with respect to isolated nanowires using DFTB, augmented by Van der Waals interactions [117]. My results for the binding energy as a function of the inter-wire separation d and the wire orientation φ are presented in Fig. 4.2(b). I find the binding energy to be generally weak and strongly anisotropic. The most stable arrangement occurs at an inter-wire separation $d = 9.3$ Å. The binding energy in this geometry corresponds to 0.1 eV for a 1 Å long nanowire segment and equals that of a corresponding segment of bundled $(10, 10)$ CNTs [118]. In realistic bundles, individual nanowires and nanotubes are likely to be twisted rather than being perfectly straight over long distances [119]. Then, their effective interaction should be closer to an average over all possible orientations. Due to its anisotropy, seen in Fig. 4.2(b), the effective attraction between $Mo_6S_4I_2$ nanowires is strongly reduced or changes to repulsion when averaging over φ, whereas the rather isotropic interaction between nanotubes does not affect their strong binding [118]. This explains the observation that bundled chalcohalide nanowires are much easier to separate than bundled carbon nanotubes.

4.2.3 Electronic Structure

Among the different properties of $Mo_6S_{6-x}I_x$ nanowires, I find their electronic structure to be most intriguing. In Fig. 4.3 I compare the band structure $E(k)$, the density of states (DOS), and ballistic conductance of isolated $Mo_6S_{6-x}I_x$ nanowires to those of an isolated (n, n) single-wall carbon nanotube. Independent of composition, I find all $Mo_6S_{6-x}I_x$ nanowires to be metallic or semi-metallic. This is appealing in view of the fact that carbon nanotubes may be conducting or semiconducting, depending on their chiral index (n, m) [12].

In Fig. 4.3(a-f), the electronic properties of the $Mo_6S_4I_2$ and the Mo_6S_6 nanowires can be compared side-by side. External gating or doping can furthermore be used to shift the Fermi level of the chalcohalide NWs, as indicated by the dotted lines

in Fig. 4.3. Similar to conducting (n, n) carbon nanotubes, I find an energy range with a constant DOS also near the Fermi energy of the gated chalcohalide NWs, suggesting high electron mobility, which is flanked by a pair of van Hove singularities. As can be seen by comparing Figs. 4.3(e) and (h), the energy separation of the van Hove singularities in the Mo_6S_6 nanowire is best matched by the metallic $(13, 13)$ carbon nanotube, which I consider here. For the sake of easy comparison with carbon nanotubes, I will focus on externally gated/doped chalcohalide NWs in the following.

The band dispersion of gated $Mo_6S_{6-x}I_x$ nanowires and the $(13, 13)$ carbon nanotube are compared in the left panels of Fig. 4.3. In all three systems considered I can identify nearly free-electron bands in the vicinity of E_F. Whereas the constant DOS near E_F in the $(13, 13)$ carbon nanotube, shown in Fig. 4.3(h), derives from bands of $C2p_\pi$ character, a very similar constant DOS of Mo_6S_6 in Fig. 4.3(e) derives from a_2 bands [14] with predominant $Mo4d\sigma$ character. In general, I expect the stability of any system to increase when populating bonding or depopulating antibonding states. In $Mo_6S_{6-x}I_x$ nanowires, the optimum stabilization is achieved by filling the $Mo4d$-derived a_2 band up to the folding point at X.

As suggested by comparing Fig. 4.3(a,d), (b,e), I find that the main effect of changing the composition of $Mo_6S_{6-x}I_x$ nanowires by iodine substitution prior to gating is to electronically dope the system by shifting the Fermi level. This finding agrees qualitatively with that in $Li_xMo_6S_6$ nanowires [18], where the most stable composition $x = 2$ has been associated with the "magic" $(Mo_6S_6)^{2-}$ complexes. As suggested above, stabilization of the system should depend on the oxidation state of the Mo backbone. In that case, initial withdrawal of 12 electrons from Mo_6 by divalent sulfur ligands, followed by adding two electrons to Mo_6 in the "magic" $(Mo_6S_6)^{2-}$ complexes, should be equivalent to withdrawing only 10 electrons from Mo_6 in the first place, by substituting two divalent sulfurs by monovalent iodines. Further increase in the concentration of Li or I should increase the population of the antibonding levels
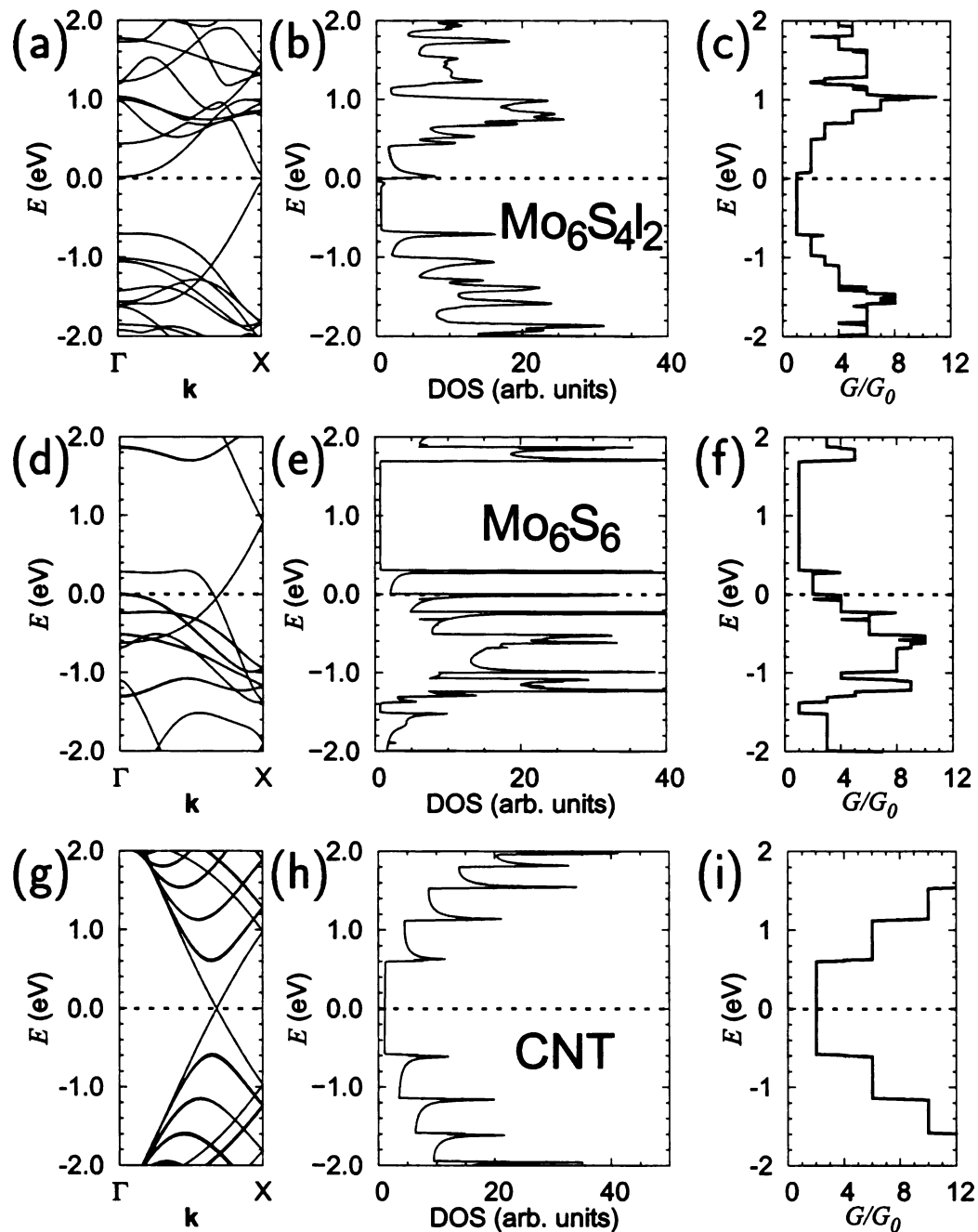
Figure 4.3: Electronic properties of a $Mo_6S_{6-x}I_x$ nanowire (a-f) in comparison to a $(13,13)$ carbon nanotube (g-i). Displayed is the band structure $E(k)$ of the $Mo_6S_{6-x}I_x$ nanowires in (a,d), their density of states (DOS) in (b,e), and quantum conductance $G(E)$ in units of the conductance quantum G_0 (c,f). The corresponding quantities for the $(13,13)$ carbon nanotube are shown in (g-i). $E = 0$, given by the dashed lines, corresponds to the Fermi level in (a,b,d,e,g,h), and to zero source-drain voltage in (c,f,i). The dotted lines show the position of E_F in externally gated/doped chalcohalide nanowires resembling carbon nanotubes.

48

and thus destabilize the system. I find this reasoning confirmed by the observed unusual stability of $Li_2Mo_6S_6$ and $Mo_6S_4I_2$, both of which should display a similar electronic configuration of the Mo backbone.

As seen in Fig. 4.3(a,d), substituting sulfur by iodine atoms in $Mo_6S_4I_2$ not only shifts the Fermi level, but also opens a narrow band gap, while introducing a new band above E_F. This nearly free-electron band of predominantly Mo4d character is also observed in the Li doped Mo_6S_6 system [18] and caused by locally changing the crystal potential along the chains of I or Li atoms in the crystal. I find the position of this band to depend sensitively on the lattice constant, suggesting the possibility to modify the electronic structure by axial deformation.

Addressing the usefulness of $Mo_6S_{6-x}I_x$ nanowires as ballistic conductors, I calculated their quantum conductance G as a function of the carrier injection energy E using the nonequilibrium Green's function approach [111, 112]. The conductance results for $x = 2$ and $x = 0$, presented in Fig. 4.3(c) and (f), are compared to those for a $(13, 13)$ carbon nanotube in Fig. 4.3(i). In the gated chalcohalide NWs, the Mo4d character of the states near E_F suggests that conduction involves mostly the Mo backbone and not the ligands.

Since all these systems are metallic, with a constant density of states near E_F, I observe similarities in the conductance spectra of gated $Mo_6S_{6-x}I_x$ nanowires and metallic carbon nanotubes. A major advantage of $Mo_6S_{6-x}I_x$ nanowires is the natural termination of finite segments by sulfur atoms, which are known to bind to Au electrodes as thio-groups in a well-defined way.

4.3 Summary

In conclusion, I combined *ab initio* density functional and quantum transport calculations to compare structural, electronic, and transport properties of $Mo_6S_{6-x}I_x$

nanowires with carbon nanotubes. I find that the $Mo_6S_4I_2$ system may form particularly stable, free-standing quasi-1D nanowires with electronic structure and conductance close to that of metallic $(13, 13)$ single-wall carbon nanotubes. $Mo_6S_{6-x}I_x$ nanowires have favorable properties in comparison to carbon nanotubes by being conductive irrespective of their structure, more easily separable, and capable of forming ideal contacts to Au leads through thio-groups.

Chapter 5

Compositional ordering and quantum transport in $Mo_6S_{9-x}I_x$ nanowires

The following discussion is closely related to a publication by Teng Yang, Savas Berber and David Tománek, Phys. Rev. B **77**, 165426 (2008) [120].

5.1 Introduction

Combining sub-nanometer diameter with structural stability and interesting electronic properties, transition metal chalcogenide nanowires have been discussed as a potentially viable alternative to carbon nanotubes [19] for many applications. In particular, $Mo_6S_{9-x}I_x$ nanowires have been studied extensively both experimentally [20, 21, 22, 6, 5, 23, 24, 25, 26, 27, 28, 29, 30, 31, 32, 33, 34] and theoretically [35, 36, 37]. In contrast to other nanowires and nanotubes, $Mo_6S_{9-x}I_x$ are believed to be metallic independent of their structure [35, 36, 21] and can be synthesized [38], dispersed [6, 5], and functionalized [23] in a straight-forward manner. Nano-mechanical studies indicate a very low shear modulus of the bundled

nanowires [26], suggesting self-lubricating properties and potential applications in nano-tribology [39]. Sulfur terminators act as "alligator clips", providing optimum contact to gold leads for molecular electronics applications.

In spite of the numerous studies, several questions about $Mo_6S_{9-x}I_x$ nanowires still await a definitive answer. There is a consensus that the skeleton of these systems consists of Mo octahedra, which are functionalized by S and I adsorbates and connected by bridges containing S or I atoms. Still, there is an open controversy about the atomic arrangement in nanowires with $x = 4.5$ and $x = 6$, which have been observed as stable compounds. X-Ray Diffraction (XRD) [21] and Extended X-ray Absorption Fine Structure (EXAFS) [40] studies agree in the identification of Mo octahedra as stable building blocks of the nanowires, but disagree about the precise positions of sulfur and iodine. In particular, both iodine [21, 40] and sulfur [33, 35, 36] have been proposed as constituents of the bridges connecting the Mo octahedral building blocks. Additional uncertainty exists, whether the connecting bridges contain three [41, 35] or four [26, 40] atoms.

Obviously, the atomic structure plays a key role in determining the stability and conductance of the nanowires. [110] In spite of apparent interest in the topic, no conductance data are available that would illustrate the potential of $Mo_6S_{9-x}I_x$ nanowires, sandwiched between gold leads, for molecular electronics applications. Besides available structural results for nanowires with $x = 4.5$ and $x = 6$ stoichiometries, which were assumed to be homogeneous, nothing is known about structural properties of nanowires with other compositions, which may phase separate into iodine-rich and iodine-depleted segments. Lack of precise structural information also offers a plausible explanation for the apparent discrepancy between the measured and calculated Young's modulus of $Mo_6S_{9-x}I_x$ nanowires [26] with $x = 4.5$ and $x = 6$.

To address these open points, I combined *ab initio* density functional theory [76, 77] and quantum transport calculations based on the nonequilibrium Green's function
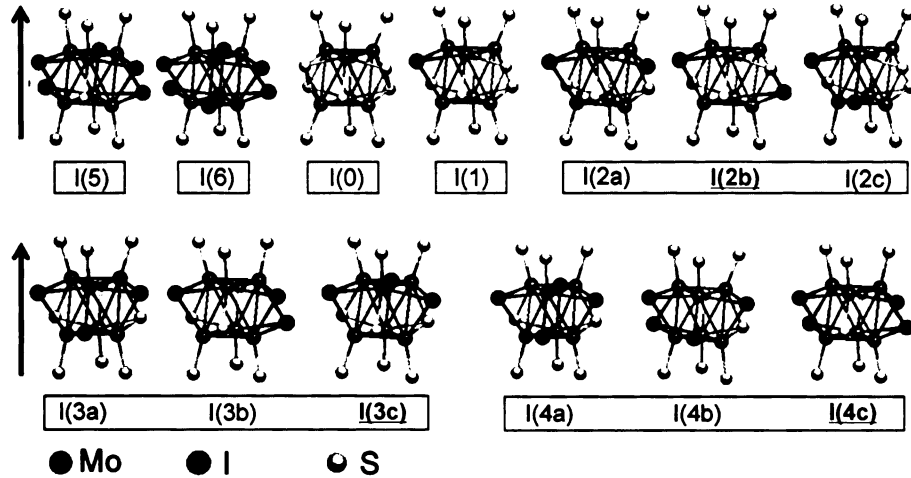
Figure 5.1: Optimized atomic arrangements within finite building blocks of $Mo_6S_{9-x}I_x$ nanowires. The structures are labelled according to the number of iodine atoms, and structural isomers with the same stoichiometry are distinguished by lowercase Latin characters. The finite clusters have been terminated by S atoms on both sides along the wire direction, indicated by the arrows. The most stable isomers for each stoichiometry are underlined and marked in red.

formalism [111, 112] to determine stability, equilibrium structure, electronic, and transport properties of $Mo_6S_{9-x}I_x$ nanowires in the full composition range. I found the $Mo_6S_6I_3$ nanowire to be particularly stable and identify stoichiometries, where separation into two phases, one of them being $x = 3$, is energetically favorable. Sulfur-terminated wire segments are known to form optimum contacts to gold leads. I find that sulfur forms the most stable bridges connecting the functionalized Mo octahedra and determine the relative stability of bridges containing three or four sulfur atoms. Finally, I determine the conductance of $Mo_6S_{9-x}I_x$ nanowires with $x = 3$ and $x = 4.5$, sandwiched between two gold leads.

5.2 Theory

To determine the optimum geometry, relative stability and ground-state electronic structure of the nanowires, I used the density functional theory (DFT) [76, 77], as implemented in the SIESTA code [87]. I used the Perdew-Zunger [100] form

of the exchange-correlation functional in the local density approximation (LDA) to DFT. The behavior of valence electrons was described by norm-conserving Troullier-Martins pseudopotentials [89] with partial core corrections in the Kleinman-Bylander factorized form [92]. I used a double-zeta basis, including initially unoccupied Mo$5p$ orbitals. I studied the possibility of spin polarization using the Local Spin Density Approximation (LSDA) and found all the nanowires investigated here to be nonmagnetic.

To test the usefulness of these systems as ballistic conductors, I calculated the quantum conductance G of $Mo_6S_{9-x}I_x$ nanowires sandwiched between two Au(111) surfaces as a function of the carrier injection energy E. My calculations were performed using the nonequilibrium Green's function approach [111], as implemented in the TRAN-SIESTAC code [112], and the localized basis set described above.

My studies focus both on the infinite nanowires and their building blocks, depicted in Fig. 5.1. Infinite nanowires are represented by a periodic arrangement of unit cells of length a containing two formula units of the compound. To describe isolated nanowires while using periodic boundary conditions, I arranged them on a tetragonal lattice with a large inter-wire separation of 30 Å. I sampled the rather short Brillouin zone of these 1D structures by 6 k-points. The charge density and potentials were determined on a real-space grid with a mesh cutoff energy of 150 Ry, which was sufficient to achieve a total energy convergence of better than 2 meV/atom during the self-consistency iterations.

5.3 Results

5.3.1 Optimum functionalization of the building blocks in nanowires

To get a better understanding of the optimum arrangement of iodine and sulfur ligands on the Mo_6 octahedral building blocks in the nanowires, I optimized the structure of all possible ligand arrangements in $Mo_6S_{12-x}I_x$ systems. To avoid complications caused by stoichiometry-dependent unit cell sizes, I first considered finite nanowire segments. The wire segments were terminated on both sides by sulfur trimers as reference ligands, which act as bridge connectors in the infinite nanowire. Such chalcohalide clusters have been observed in cluster compounds, with a particular oxidation state stabilized by counter-ions [121]. Even though I consider charge neutral wire segments, the electron count on the Mo_6 octahedra may differ from the infinite nanowire due to the presence of ligands on both sides, causing minor structural and energetic changes. My results for the equilibrium structure of these finite building blocks with the composition $0 \leq x \leq 6$ are shown in Fig. 5.1. For the sake of fair comparison, I oriented the Mo_6 clusters along the nanowire direction, indicated by the arrows, and grouped visually the different structural isomers with the same composition.

The choice of using sulfur reference ligands is inspired by the results of the combined scanning transmission electron microscopy (STEM) and X-ray photoelectron spectroscopy (XPS) study of $Mo_6S_3I_6$ nanowires [33], suggesting that all bridges connecting Mo_6 octahedra, covered by iodine ligands, contain only sulfur atoms.

To interpret my results, I represent the structures of Fig. 5.1 schematically in Fig. 5.2. In the representation of Fig. 5.2, I first lay down the molybdenum octahedra onto one of their faces, to be considered the projection plane. Next, I consider the position of ligands decorating all faces except those parallel to the projection plane.
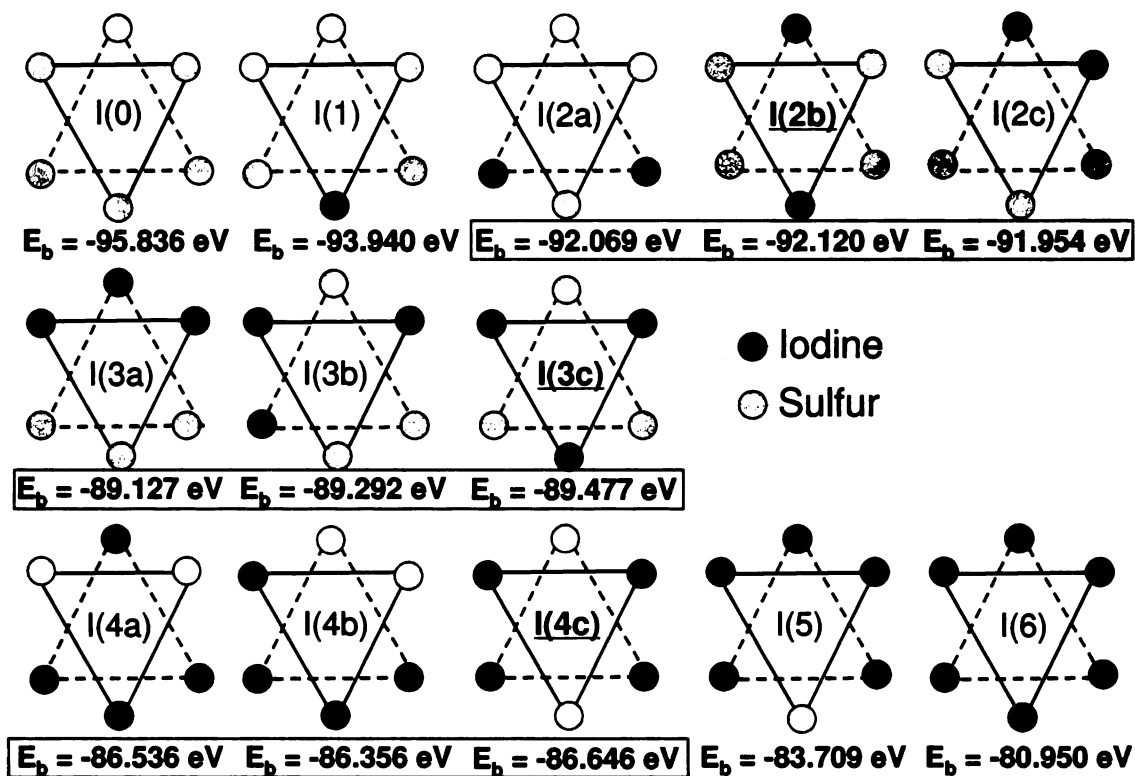
Figure 5.2: Schematic arrangement of sulfur and iodine ligand atoms in the structures of Fig. 5.1, along with the binding energy values E_b with respect to isolated atoms. The most stable isomers for each stoichiometry are underlined and marked in red.

Of the six ligands, two triplets will form two equilateral triangles, rotated by 180° with respect to each other, in planes parallel to the projection plane. These triangles, with the corners corresponding to ligand positions, are depicted in Fig. 5.2. Clearly, structures with $x = 0, 1, 5, 6$ iodine atoms have only one structural isomer, labeled as I(x) in Fig. 5.1 and Fig. 5.2. Structures with $x = 2, 3, 4$ iodine atoms have three structural isomers each. My binding energy results in Fig. 5.2 suggest that the relative stability of these structural isomers can differ up to ≈ 0.35 eV. I find that the most stable isomer for each stoichiometry, marked by an underlined red label, also has the highest symmetry. Since the inter-iodine distance is maximized in the favored structures, energy stabilization of the symmetric structures can be understood in terms of minimizing Coulomb repulsion.

$\Delta E = -0.65$ eV

● Mo   ● I   ○ S
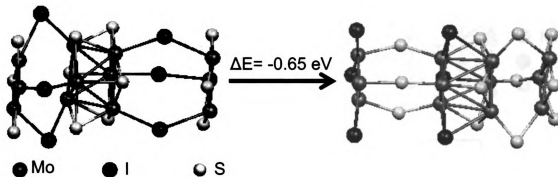
Figure 5.3: Optimized structure of two isomers with the same stoichiometry $Mo_6S_6I_3$ representing the connection between functionalized Mo_6 building blocks in nanowires by iodine (left) and sulfur (right) bridges.

5.3.2   Connection between building blocks in nanowires

In previous studies, both sulfur [33, 35, 36] and iodine [21, 40] have been postulated to form connecting bridges between functionalized Mo_6 building blocks in $Mo_6S_{9-x}I_x$ nanowires. Furthermore, the stability of sulfur- and iodine-based connections has been claimed to be nearly the same [36]. To identify the nature of energetically preferred bridges, I considered two structural isomers of infinite $Mo_6S_6I_3$ nanowires, one with iodine and the other with sulfur bridges connecting the Mo_6-based building blocks. A unit cell of the optimized structures, containing 30 atoms, is shown in Fig. 5.3. I performed a global structure optimization, including the relaxation of the unit cell size, and found the nanowire connected with sulfur bridges to be energetically more stable by 0.65 eV per 30 atoms, providing further support for the presence of sulfur bridges.

5.3.3   Elastic properties of nanowires

In bundles of nanowires, the Young's modulus can be determined from the stress/strain ratio in the wire direction. Experimental observations [26] of high Young's modulus values near 420 GPa in $Mo_{12}S_9I_9$ and $Mo_{12}S_6I_{12}$ suggest that these nanowires should be very rigid in the axial direction. To explain this high
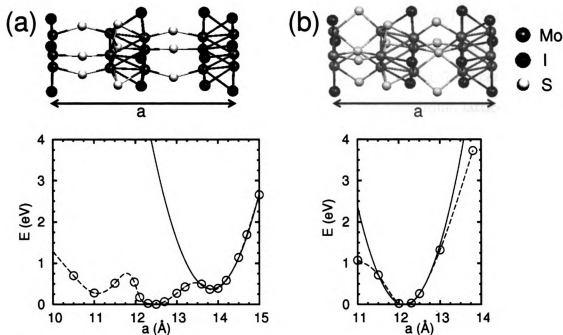
Figure 5.4: Equilibrium structure and axial rigidity in (a) $Mo_{12}S_9I_9$ and (b) $Mo_{12}S_{11}I_9$ nanowires. The main difference between the compounds is an additional S atom in (b) inserted inside each of the S_3 bridges in (a). E denotes the total energy relative to the optimum structure and a is the lattice constant. Dashed lines are guides to the eye, connecting the data points. Quadratic fits to the data points near the equilibrium, related to the axial rigidity, are given by the solid lines.

rigidity, the bi-stable S_3 bridges [41, 35], connecting the Mo-based building blocks, were postulated to contain one extra atom in the middle [26, 40]. To understand the difference between S_3 and S_4 bridges in terms of axial rigidity, I determined the stability of $Mo_{12}S_9I_9$ and $Mo_{12}S_{11}I_9$ as a function of the lattice constant. Optimized equilibrium structures and binding energies of these systems are presented in Fig. 5.4. As seen in Fig. 5.4(a), owing to the bi-stability of the two S_3 bridges, the $E(a)$ graph exhibits three minima, the most stable of them corresponding to one short and one long sulfur bridge. In the finite lattice constant range between the different minima, stretching and compression of the nanowire occurs at minimum energy cost. This is no longer true, however, when considering additional compression of a completely compressed or additional stretching of a completely extended nanowire. A quadratic

fit of the $E(a)$ plot near the minima, depicted by the solid lines in Fig. 5.4, suggests that there is little difference in the spring constant $k = \partial^2 E/\partial a^2$ of the nanowires represented in Figs. 5.4(a) and 5.4(b). Using the quadratic fits of Fig. 5.4, I can calculate the Young's modulus as $Y = k(a_{eq}/A)$, where a_{eq} is the equilibrium lattice constant and A is the cross section of the nanowire. The cross-section area per nanowire in an infinite bundle, where the inter-wire distance has been optimized [110] to be 9.4 Å, is $A = 76.5$ Å^2. This allows us to determine the Young's modulus of $Mo_{12}S_9I_9$ with S_3 bridges as $Y = 99$ GPa, and that of $Mo_{12}S_{11}I_9$ with S_4 bridges as $Y = 109$ GPa. Thus, I conclude that the central atom in the S_4 bridges does not necessarily increase the axial rigidity of the nanowires.

My results are well within the wide range of reported theoretical and experimental values of the Young's modulus in $Mo_{12}S_xI_y$ nanowires, with calculated data being generally much softer than observed values [26, 36, 122]. The calculated value [26] $Y = 45$ GPa in $Mo_{12}S_6I_{12}$ nanowires is much smaller than other reported theoretical values [36] $Y = 82$ GPa and $Y = 94$ GPa in this system, which contains bi-stable S_3 bridge connectors, and the $Y = 114$ GPa value in $Mo_{12}S_8I_{12}$ nanowires with S_4 bridges [36]. An even larger value $Y = 320$ GPa has been predicted for Mo_6S_6 nanowires [122]. Comparing all available data, I conclude that the Young's modulus may depend sensitively on the stoichiometry.

5.3.4   Compositional ordering and phase separation in nanowires

Since the synthesis of $Mo_6S_{9-x}I_x$ nanowires occurs in a single-step reaction directly from the elements [38], I explore the intriguing possibility of forming nanowires with an arbitrary iodine concentration. To account for phase separation, which may be expected in this case, I consider coexistence of domains with different compositions. In the simplest scenario, I consider domains with only two different compositions, identified by the iodine concentration x_1 and x_2. My objective is to determine
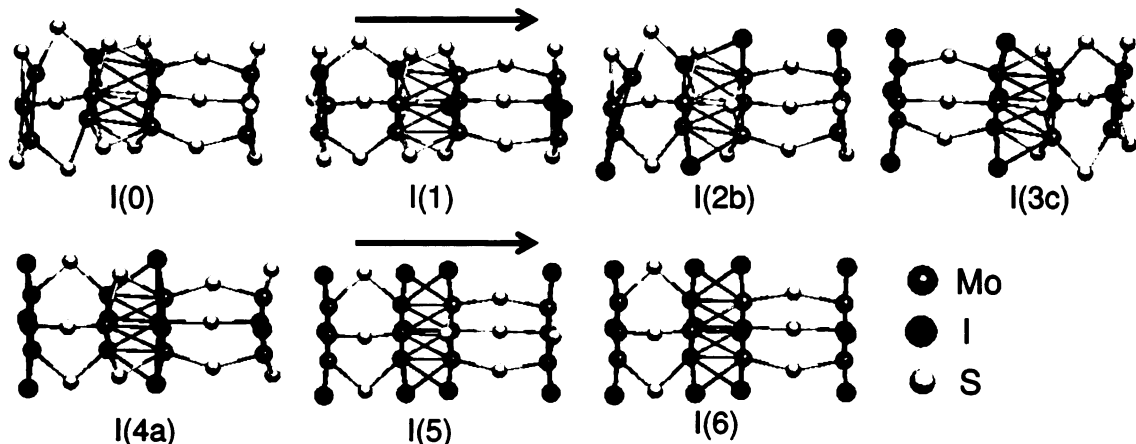
Figure 5.5: Optimized atomic arrangement in double unit cell of infinitely long $Mo_6S_{9-x}I_x$ nanowires for $0 \leq x \leq 6$. Only the most stable isomers for each stoichiometry are shown and labelled according to the number of iodine atoms x per formula unit. The nanowire direction is indicated by the arrows.

the most stable domain structure for $Mo_6S_{9-x}I_x$ nanowires with an arbitrary value of the average iodine concentration $< x >$.

Before addressing inhomogeneous nanowires, I first identify the most stable structure of homogeneous nanowires. I identified the optimum geometry and binding energy of all nanowires formed with any of the building blocks depicted in Fig. 5.1 and Fig. 5.2, considering the possibility of parallel and antiparallel alignment of asymmetric building blocks along the nanowire, and also the possibility of the bi-stable sulfur bridges being short or long. As suggested earlier, the most stable structural isomers in the infinite systems, depicted in Fig. 5.5, may deviate from those for the finite building blocks. The binding energy E_b of the most stable structural isomer, given per unit cell with respect to isolated atoms, is indicated by the data points in Fig. 5.6(a). The straight solid line, connecting the data points for structures with no iodine and with no sulfur ligands, represents the expectation value $< E_b >$ in case that there is no energy preference for specific ligand arrangements. Similar to alloys [123], deviations from the straight line for $0 < x < 6$ indicate a tendency to mix or to phase separate.

60
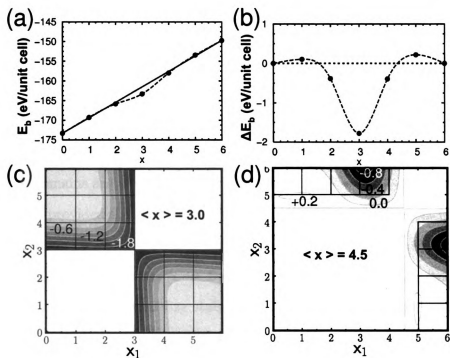
Figure 5.6: Mixing and phase separation tendency in $Mo_6S_{9-x}I_x$ nanowires. (a) Binding energy E_b as a function of the iodine concentration x. The data points refer to structures depicted in Fig. 5.5. The solid line, obtained by connecting the data points at $x = 0$ and $x = 6$, depicts the expectation value $< E_b >$. The dashed line is a guide to the eye. (b) Energy gain $\Delta E_b(x)$ with respect to $< E_b >$. The energy gain associated with phase separation into domains with iodine concentrations x_1 and x_2 is presented in contour plots for systems with $< x >= 3.0$ in (c) and $< x >= 4.5$ in (d). Quantitative results are only valid for integer values of x_1 and x_2, indicated by the grid. The contours in (c) and (d), given in units of eV/unit cell, are guides to the eye. Dark areas represent particularly stable stoichiometries.

61

To better distinguish, which structures are more stable than what would be expected for a mixture of noninteracting ligands arranged randomly along the nanowire, I show in Fig. 5.6(b) the energy difference between the optimized uniform systems and the expectation value $< E_b >$. The higher-than-average stability of nanowires with $x = 3$ suggests the corresponding stoichiometry to likely be present in one of the components in case of phase separation. On the other hand, I are unlikely to encounter dominant phases with $x = 1$ or $x = 5$.

Next, I consider a nanowire with the average composition $Mo_6S_{9-<x>}I_{<x>}$, separated into domain 1 of length L_1 with the composition $Mo_6S_{9-x_1}I_{x_1}$ and a second domain 2 of length L_2 with the composition $Mo_6S_{9-x_2}I_{x_2}$. The lengths of the domains are trivially related by $L_1 x_1 + L_2 x_2 = (L_1 + L_2) < x >$. On the other hand, provided that $x_1 \leq <x> \leq x_2$ or $x_2 \leq <x> \leq x_1$, the relative segment lengths are given by $L_1/L = (<x> - x_1)/(x_2 - x_1)$ and $L_2/L = (x_2 - <x>)/(x_2 - x_1)$ in a nanowire of length $L = L_1 + L_2$. Even though both x_1 and x_2 are integers, I find it useful to visualize stability islands using non-integer values of x_1, x_2 and interpolated energy values presented in Fig. 5.6(b). The allowable concentration range (x_1, x_2) is shown by shaded areas in Fig. 5.6(c) for $<x> = 3.0$ and in Fig. 5.6(d) for $<x> = 4.5$. These figures show the contour plot $\Delta E(x_1, x_2)$, corresponding to the energy difference between the expectation value of the binding energy for $<x>$ and the weighted average of $E_b(x_1)$ and $E_b(x_2)$. For a given value of $<x>$, the pair of integers (x_1, x_2), corresponding to the lowest value of ΔE, identifies the preferred concentrations and relative lengths of the two phases. Inspecting Figs. 5.6(c) and 5.6(d) for dark areas, corresponding to particularly stable structures, I find that at least one of the two phases occurs with $x = 3$.

In my simple energy estimates underlying Figs. 5.6(c) and 5.6(d), I ignored the energy associated with forming domain wall boundaries between regions with different compositions. In Fig. 5.7, I investigate the energy cost of domain wall boundaries
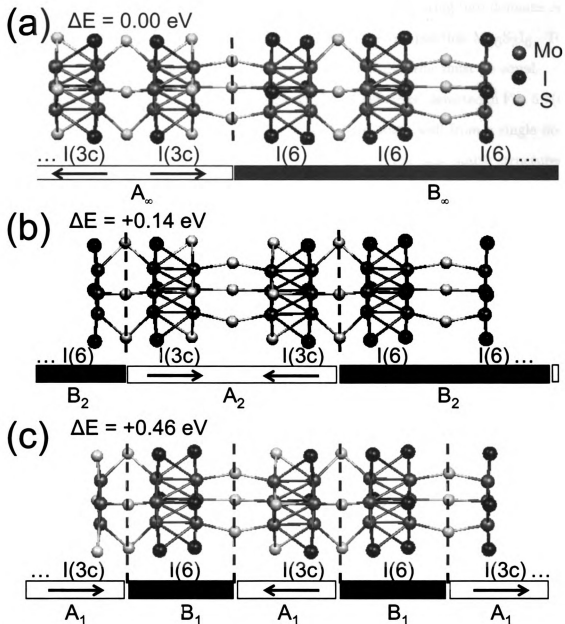
Figure 5.7: Energy cost associated with grain boundaries in $Mo_6S_{9-x}I_x$ nanowires with $<x> = 4.5$, consisting of domains **A** with $x = 3$ and domains **B** with $x = 6$. (a) Reference structure, with a single boundary separating domains A and B. (b) Double unit cells of A and B alternate along the nanowire. (c) Individual unit cells of A and B alternate along the nanowire. The energy differences ΔE are given for two formula units of $Mo_{12}S_9I_9$, containing 60 atoms.

in $Mo_6S_{9-x}I_x$ nanowires with $< x >= 4.5$, addressed in Fig. 5.6(d). Those results suggest that the nanowire will be most stable when separating into domains **A** with the composition $Mo_6S_6I_3$ and domains **B** with the composition $Mo_6S_3I_6$. To maintain the average stoichiometry, the size of **A** and **B** domains must be equal.

The reference structure of an infinite $Mo_6S_{4.5}I_{4.5}$ nanowire, depicted in Fig. 5.7(a), contains a single domain of phase **A**, separated by a domain wall from a single domain of phase **B**. As suggested in Fig. 5.4(a) and Fig. 5.5, the most stable structures of phases **A** and **B**, labeled A_∞ and B_∞ in Fig. 5.7(a), exhibit an alternating sequence of short and long sulfur bridges. Figure 5.4(a) also suggests that in phase **A**, the orientation of the I(3c) building blocks, defined in Fig. 5.1, should alternate, as indicated by the arrows in Fig. 5.7(a).

The same average stoichiometry $Mo_6S_{4.5}I_{4.5}$ can be achieved by periodically alternating double unit cells of domains **A** and **B**, labeled A_2 and B_2 in Fig. 5.7(b). The decrease in stability with respect to the structure of Fig. 5.7(a), reflected in the positive value of the energy cost ΔE, indicates that the creation of additional domain walls is energetically unfavorable. This finding is further supported by an even larger value of ΔE in the structure of Fig. 5.7(c), where the number of domain walls has doubled with respect to Fig. 5.7(b). The value of ΔE for the system of Fig. 5.7(c) is not twice the value for the system of Fig. 5.7(b), since the local atomic arrangement near the (A_1, B_1) domain boundary differs from that near the (A_2, B_2) domain boundary.

5.3.5 Quantum transport in nanowires

One of the most attractive features of $Mo_6S_{9-x}I_x$ nanowires is the presence of S_3-bridges, known to form well-defined, stable bonds to Au surfaces. I calculate quantum conductance in nanowires with the $Mo_6S_{4.5}I_{4.5}$ stoichiometry, since $Mo_6S_3I_6$ nanowires do not attach readily to Au electrodes [124]. In the following, I will consider
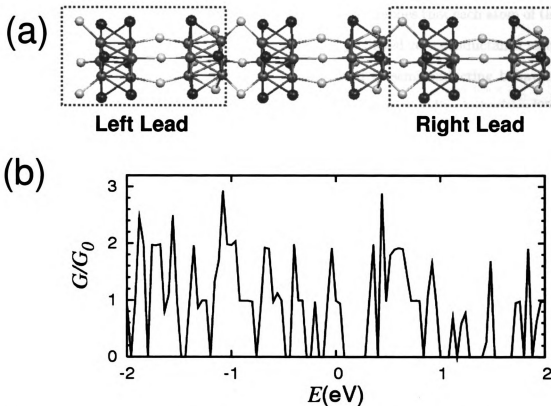
Figure 5.8: Quantum conductance of an isolated, infinitely long $Mo_6S_{4.5}I_{4.5}$ nanowire. (a) Definition of the scattering and the lead regions in an atomistic model of the nanowire. (b) Quantum conductance G of the nanowire in units of the conductance quantum G_0, calculated at zero bias using a non-equilibrium Green function formalism.

the optimized, frozen structure of infinitely long and of finite nanowires, sandwiched between gold leads, and determine the quantum conductance of this system within the Landauer-Büttiker formalism.

In the first study, I consider an infinitely long $Mo_6S_{4.5}I_{4.5}$ nanowire, shown in Fig. 5.8(a). I treat one unit cell as the scattering region and define the rest of the nanowire as the semi-infinite leads. The quantum conductance G of the infinite nanowire in units of the conductance quantum G_0 is depicted in Fig. 5.8(b). The incident energy E of the carriers is with respect to the Fermi level of the leads, which in this case refers to the entire nanowire. $G(E)$ has a nonzero value at $E = 0$, suggesting metallic conductivity at very small bias values. Its maximum value of $3G_0$,

corresponding to 3 conduction channels in the nanowire, implies that each atom of the S_3 bridge contributes one conduction channel. The predicted zero conductance value just above $E = 0$ suggests that n-doping should lead to semiconducting behavior. This explains the observed conductivity drop in nanowires with iodine impurities [25].

Next I study the quantum conductance of a finite $Mo_6S_{4.5}I_{4.5}$ nanowire segment sandwiched between Au(111) surfaces as "ideal" leads, shown in Fig. 5.9(a). I selected Au(111) leads, since gold forms stable covalent bonds with sulfur, and since the atomic structure at the Au(111) surface is very similar to that of the Mo_6 octahedra. This allows for a well-defined connection between the nanowires and the gold leads by S_3 bridges, causing negligible structural changes near the wire-lead interface. Besides the nanowire segment, I included also the topmost layers of the Au(111) surface at both sides in the scattering region, as indicated in Fig. 5.9(a), to correctly represent changes in the electronic structure in the contact region. Closer inspection of the charge density of the composite system suggested that changes in the electronic structure are very small, and that including only 2-3 topmost layers of Au(111) in the scattering region should represent the electronic properties and conductance of the system adequately.

The quantum conductance $G(E)$ of the system in units of the conductance quantum G_0 is presented in Fig. 5.9(b). Here, incident energy E of the carriers is given with respect to the Fermi level of the gold leads. The energy dependence of G suggest a good metallic conductance and closely resembles my results for the infinite nanowire, depicted in Fig. 5.8(b). The reduction from the maximum value $G = 3G_0$ in the infinite nanowire, caused by the reflection at the nanowire-gold contacts, is relatively small, confirming the high quality of contacts between sulfur-terminated nanostructures and gold. The fact that the dip in the conductance of the infinite nanowire and the sandwiched nanowire segment occurs at the same energy just above $E = 0$ suggests that the contact with gold does not change the Fermi level of the
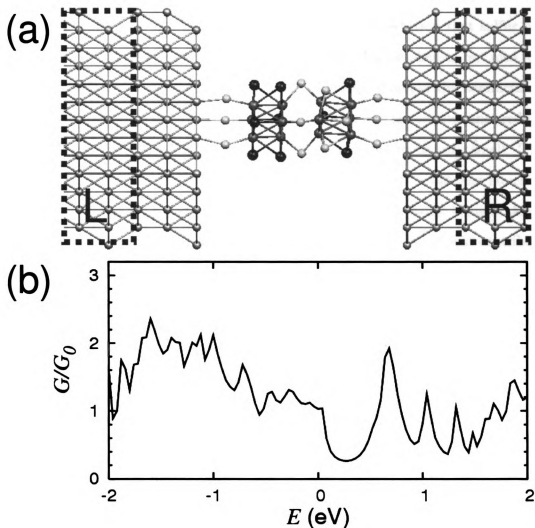
Figure 5.9: Quantum conductance of an isolated, finite $Mo_6S_{4.5}I_{4.5}$ nanowire sandwiched between Au(111) surfaces. (a) Definition of the scattering and the lead regions in an atomistic model. The left and right leads are semi-infinite gold surfaces, indicated by the dashed lines. The scattering region contains the nanowire segment connected to topmost layers of the Au(111) surface at both sides. (b) Quantum conductance G of the system in units of the conductance quantum G_0, calculated at zero bias using a non-equilibrium Green function formalism.

nanowire significantly. The filling of the conductance dip above $E = 0$ in Fig. 5.9(b) is caused by the wavefunctions of the leads, which extend into the nanowire and overlap, thus increasing the conductance of the short nanowire segment.

My conductance calculations confirm the initial expectation that sulfur atoms form not only stable bridges between functionalized Mo_6 octahedra, but also robust and electronically transparent contacts to gold leads. Whereas the conductance of nanowires is generally dominated by contact regions, I find the conductance reduction at the interface between $Mo_6S_{4.5}I_{4.5}$ nanowires and gold to be very small. This is likely to hold true also for other $Mo_6S_{9-x}I_x$ nanowires with a different stoichiometry, as long as the Mo-based building blocks are connected by sulfur bridges. Also the delocalization of conduction electrons within the Mo_6 octahedra should contribute to an excellent electrical conductance behavior of the nanowires [110], independent of the stoichiometry.

5.4 Summary and conclusions

I used *ab initio* calculations to study compositional ordering and quantum transport in $Mo_6S_{9-x}I_x$ nanowires. The skeleton of these nanowires consists of Mo octahedra, which are functionalized by S and I adsorbates and connected by flexible S_3 bridges. Optimum geometries and relative stabilities at different compositions are determined using density functional theory. I find nanowires with $x = 3$ to be particularly stable. Nanowires with other compositions are likely to phase separate into iodine-rich and iodine-depleted segments, some of which should have the stoichiometry $Mo_6S_6I_3$. My transport calculations, based on the nonequilibrium Green's function formalism, indicate that the nanowires are metallic independent of composition and exhibit a quantum conductance of $G = 3G_0$, with the three conductance channels involving the S_3 bridges.

Chapter 6

Self-assembly of long chain alkanes and their derivatives on graphite

The following discussion is closely related to a publication by Teng Yang, Savas Berber, Jun-Fu Liu, Glen P. Miller, and David Tománek, J. Chem. Phys. **128**, 124709 (2008) [125]. This study is a collaborative project with an experimental group at the University of New Hampshire. Even though my contribution is limited to calculations in the theoretical part, results of the entire study are reproduced in the following as an example, how a Theory-Experiment collaboration can help to understand nanoscale phenomena.

6.1   Introduction

The controlled self-assembly of molecules to form ordered nanoscale patterns is an area of active research. These superstructures often exhibit unusual properties [42] and are finding numerous applications in nanotechnology, including use as nanotemplates [43]. Nanotemplates enable directed assembly of nanoscale objects and allow for the transfer of those patterned objects to receiving substrates. For example, as nanoparticles can be selectively attached to either molecular or polymeric species,

nanotemplates derived from self-assembled molecules or polymers provide an efficient means to prepare ordered arrays of uniformly spaced nanoparticles. Nanotemplates of this type permit feature sizes and feature densities that are unrivaled by current lithographic techniques including electron-beam nanolithography and scanning probe methods like dip-pen nanolithography [44] and field-assisted nanolithography [45].

Self-assembled monolayers (SAMs) of molecular and polymeric species on highly oriented pyrolytic graphite (HOPG) have attracted much attention, since the formation of various adsorption patterns can be monitored using scanning tunneling microscopy (STM) methods [46, 47, 48, 49]. Although many patterns have been reported even for alkane films on graphite, the energetic grounds for the optimum SAM structure have never been investigated. Since the interplay between adsorbate-adsorbate and adsorbate-substrate interactions ultimately determines the equilibrium geometry of the molecular assemblies, it should be possible to induce specific changes in the SAM superstructures by modifying the terminal functional groups of the molecules in a pre-determined manner. Unfortunately, published STM data of SAMs on graphite do not provide a quantitative interpretation of the resulting superstructures and therefore do not allow for predictions concerning the effect of specific functional groups on the corresponding self-assembled superstructure.

Here I study the self-assembly of long chain alkanes and their derivatives on graphite using a combination of scanning tunneling microscopy (STM) measurements with *ab initio* electronic structure and total energy calculations. I identify the optimum adsorption geometry of the molecules and explain the energetic origin of the domain morphology observed by STM. My electronic structure calculations allow a quantitative interpretation of the STM images. Calculated total energy results provide a quantitative basis for judging the ordering tendency of alkane chains in self-assembled monolayers and ways to modify the ordering using alcohol (OH) and carboxylic acid (COOH) functional groups.

6.2 Computational details

To obtain fundamental insight into the origin of different adsorption patterns of long chain alkanes and their derivatives on graphite, I determined the equilibrium geometry, binding energy and electronic structure of these systems under different conditions. My calculations are based on the *ab initio* density functional theory (DFT) within the local density approximation (LDA) [126]. I used the Perdew-Zunger [100] parameterized exchange-correlation functional, as implemented in the SIESTA code [87], and a double-ζ polarized basis localized at the atomic sites. I used the counterpoise method [94] to avoid basis-set superposition errors (BSSE) introduced by the localized basis. The valence electrons were described by norm-conserving Troullier-Martins pseudopotentials [89] in the Kleinman-Bylander factorized form [92]. This computational approach is known to correctly describe the equilibrium geometries and energies associated with the alkane-alkane and alkane-HOPG interaction, as well as the strength of alcohol-alcohol and acid-acid hydrogen bonds.

Since adsorption of alkane chains on graphite and graphene should be very similar, I performed my calculations on infinite graphene monolayers using periodic boundary conditions. In the superlattice geometry modeling isolated monolayers, graphene layers were separated by 20 Å in the normal direction and represented by orthorhombic unit cells containing 4 carbon atoms. The supercells were sampled by a 32×32×1 k−point mesh. When modeling finite alkane chains on graphene, I used 3×5 graphene supercells with 60 C atoms and sampled the Brillouin zone by a 11×7×1 k−point mesh. The self-consistent charge density was obtained using a real-space grid with a mesh cutoff energy of 250 Ry, sufficient to achieve a total energy convergence of better than 0.05 meV/atom during the self-consistency iterations.

6.3　Experimental details

As a counterpart to the theoretical results, my experimental colleagues observed overlayers of alkanes and their derivatives on graphite using scanning tunneling microscopy (STM). Saturated solutions of n-docosane (99%, Aldrich, Milwaukee, WI), 1-docosanol (97%, Aldrich, Milwaukee, WI), and 1-docosanoic acid (99%, Aldrich, Milwaukee, WI) were prepared in 1-phenyloctane (99.9%, Aldrich, Milwaukee, WI). A small drop of the solutions was spread onto a freshly cleaved surface of HOPG (ZYA grade, MikcroMasch, Wilsonville, OR). Scanning tunneling microscope imaging was performed under ambient conditions (21° − 23°C) using a Nanoscope IIIa STM (Digital Instruments, Santa Barbara, CA) with platinum/iridium tips (Digital Instruments, Santa Barbara, CA). The STM was calibrated using freshly cleaved HOPG. Images were captured *in situ* in constant current mode at the HOPG-liquid interface, while integral and proportional gains were in the range 2-5. The raw images were filtered to remove high frequency noise.

6.4　Results

6.4.1　Free-standing long-chain alkanes

The calculated equilibrium geometry and electronic structure of free-standing polyethylene, representing an alkane chain, is shown in Figs. 6.1(a-b). To represent isolated polymers in a superlattice geometry, I arranged them on a tetragonal lattice with a large inter-chain separation of 20 Å and sampled the rather short Brillouin zone of these 1D structures by 16 k−points. The optimized structure of free-standing polyethylene, with the carbon backbone forming a zigzag chain, is shown in Fig. 6.1(a). The primitive unit cell of length $a = 2.55$ Å contains two C and four H atoms. The LDA band structure of the infinite chain, depicted in Fig. 6.1(b), sug-
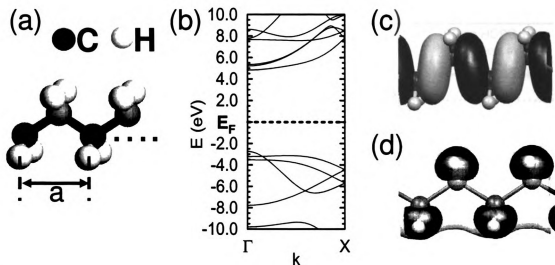
Figure 6.1: (a) Equilibrium geometry and (b) electronic band structure of an infinitely long polyethylene chain. Wave functions of the states at $k = \Gamma$ corresponding to (c) the top of the valence band and (d) the bottom of the conduction band are shown in the same perspective as used in (a). The wave function contours are presented for the amplitude $|\psi| = 0.04 \, a_0^{-3/2}$ and superposed with the atomic positions. The wave function phase is distinguished by color.

gests that polyethylene is a wide-gap insulator. The wave functions associated with the top of the valence band at Γ are shown in Fig. 6.1(c), those of the conduction band bottom at Γ are shown in Fig. 6.1(d). The spatial distribution of these frontier orbitals is useful for judging the nature of polymer-polymer and polymer-graphene interactions.

6.4.2 Structure and stability of long-chain alkane monolayers

For long chain alkanes on graphite, controversy exists concerning whether the carbon skeletal plane should lie parallel [127], perpendicular [49], or at an $\approx 30°$ angle [128] to the graphite basal plane in the SAM superstructure. To help solve this controversy, I compared the total energies of the different structures and show my results in Fig. 6.2. I distinguish the *co-planar orientation* (P), where the zigzag carbon backbones of the alkanes or polyethylene, separated by the distance d, all lie in the
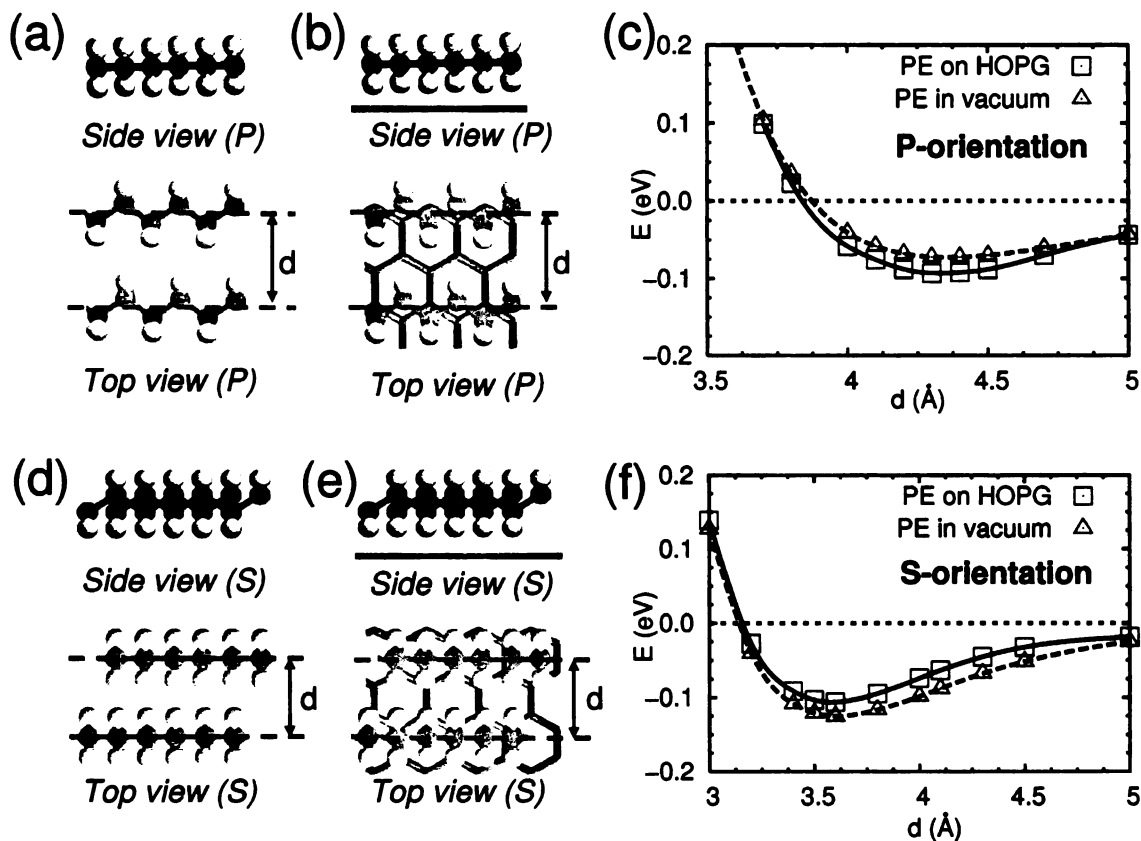
Figure 6.2: Interactions between two infinitely long polyethylene chains in (a-c) co-planar (P) and (d-f) stacked (S) arrangements. Interaction energies are plotted in (c) and (f) as a function of the inter-chain distance d for polymers in vacuum, depicted in (a) and (d), and polymers adsorbed on graphene, depicted in (b) and (e). Energy values per primitive unit cell of the polyethylene chain pair in vacuum are indicated by empty triangles and those for chains chemisorbed on graphene by empty squares in (c) and (f).

same plane, from the *stacked orientation* (S), where all alkane or polyethylene chains are axially rotated by 90° and the zigzag carbon backbone planes are separated by d in the normal direction. On graphene, the P orientation of polyethylene in vacuum, depicted in Fig. 6.2(a), translates to that of polyethylene chains lying down parallel to graphene, as shown in Fig. 6.2(b). The energetic comparison in Fig. 6.2(c) suggests that the graphene substrate plays only a minor role in the inter-chain interaction. In particular, the equilibrium inter-chain distance of 4.26 Å in the co-planar orientation is nearly the same in vacuum and on graphene.

Similarly, the S orientation of polyethylene in vacuum, depicted in Fig. 6.2(d), translates to that of polyethylene chains adsorbed with their zigzag planes normal to the graphene substrate, as indicated in Fig. 6.2(e). Again, the equilibrium inter-chain distance of 3.50 Å in this geometry is very similar on graphene and in vacuum, as seen in Fig. 6.2(f). Comparing energy values in Figs. 6.2(c) and 6.2(f), I find that the inter-chain attraction leads to an energy gain of ≈ 0.1 eV per C_2H_4 unit with respect to separated polymers, both in the co-planar (P) and the stacked (S) orientation. The small energy differences in the inter-chain interaction are introduced by the graphene substrate and can be attributed to inequivalent adsorption sites on graphene. These are likely to be modified in the case of incommensurate overlayers, which are known to form Moiré patterns in STM images [49].

Considering a C_2H_4 unit of an isolated polyethylene chain, adsorption on graphene leads to an energy gain of 0.09 eV in the S orientation and 0.12 eV in the more stable P orientation. In view of the polyethylene-substrate attraction that is similar to the inter-chain attraction, I expect the formation of self-assembled monolayers forming both S- and P-domains on graphene. Due to their higher stability, P-domains should prevail unless the system is subject to external constraints including lateral pressure.

Having established the optimum polymer arrangement within the polyethylene layers, I next address the preferential orientation of the polymer chains with respect to the graphene substrate. Different representative alignments for the two orientations are depicted in Fig. 6.3. The optimized adsorption geometry of polyethylene in the preferential parallel (P) orientation, lying down on graphene along the armchair direction, is depicted in Fig. 6.3(b), and the corresponding zigzag alignment is shown in Fig. 6.3(c). I should note that in the optimum adsorption geometry of P-oriented PE aligned along the zigzag direction on graphene, the plane of the PE carbon backbone is tilted by 2.5° with respect to graphene, which will have important consequences for the STM images of alkane chains.
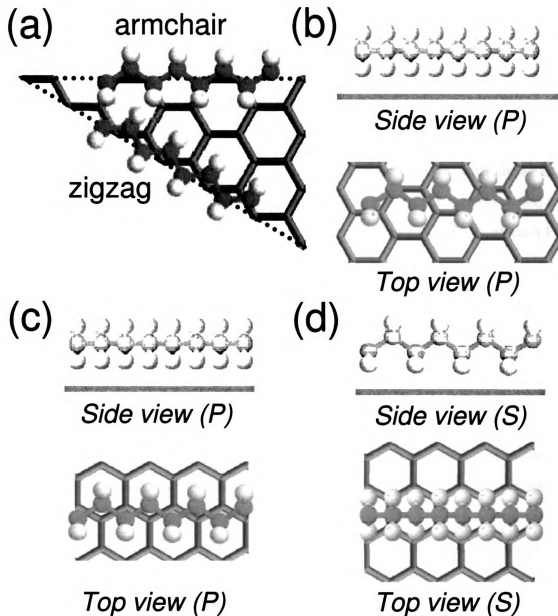
Figure 6.3: Alignment of polyethylene (PE) chains in different orientation on graphene. Polyethylene may lie parallel to graphene in the P orientation or normal to graphene in the S orientation. (a) Definition of armchair and zigzag directions on graphene. (b) PE(P) along the armchair direction, (c) PE(P) along the zigzag direction, and (d) PE(S) along the zigzag direction, viewed from the side or the top.

Energetically, I find zigzag aligned PE in Fig. 6.3(c) to be favored by 0.08 eV per C_2H_4 unit with respect to armchair aligned PE. The zigzag alignment represents the most favorable structure, since axial displacements of the chain reduce its binding

energy by no more than 0.02 eV per C_2H_4 unit, suggesting that even misaligned or displaced chains prefer the zigzag direction. As mentioned in the discussion of my results in Fig. 6.2, zigzag aligned polyethylene lying down parallel to graphene in Fig. 6.3(c) is energetically favored by 0.03 eV per C_2H_4 unit over polyethylene standing up normal to graphene in Fig. 6.3(d). Based on the hierarchy of interactions, I expect coexistence of polyethylene chains in P and S orientation, with zigzag and armchair alignment on the graphene substrate. The largest domains are expected for the stable P-oriented PE in zigzag alignment, the smallest domains for S-oriented PE in armchair alignment.

6.4.3 Bonding nature of long-chain alkanes on graphite

The chemical origin of the adsorbate interaction with the graphene substrate is addressed in Fig. 6.4 for P-oriented polyethylene and in Fig. 6.5 for S-oriented polyethylene. The height of the polyethylene axis center above graphene is $h = 3.4$ Å for P-oriented polyethylene and $h = 3.8$ Å for S-oriented polyethylene. This relatively large adsorbate-substrate separation is consistent with the relatively small adsorption energy. The total charge densities in Figs. 6.4(c) and 6.5(c), and in particular the difference charge densities in Figs. 6.4(d) and 6.5(d) indicate that there is essentially no net charge transfer between adsorbate and substrate. Small, but nonzero values of the charge density difference in Figs. 6.4(d) and 6.5(d) are indicative of weak covalent bonds. The moderate charge density accumulation in the region between PE and graphene, observed in Fig. 6.4(d), explains the slightly stronger adsorption bond in the P orientation. The weaker adsorption bond in the S orientation may be traced back to a moderate charge density depletion in the same region, observed in Fig. 6.5(d).
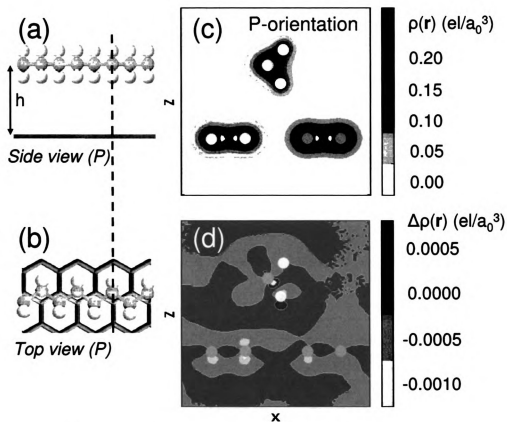
Figure 6.4: Nature of bonding of polyethylene in P orientation, lying parallel to graphene. The polyethylene adsorption geometry on graphene, shown (a) in side view and (b) in top view. Contour plots of (c) the total charge density $\rho_{PE/gra}(\mathbf{r})$ and (d) the charge density difference, defined as $\Delta\rho(\mathbf{r}) = \rho_{PE/gra}(\mathbf{r}) - \rho_{PE}(\mathbf{r}) - \rho_{gra}(\mathbf{r})$. The plane of the contour plots is normal to the polymer axis and is indicated by the dashed line in (a) and (b).

6.4.4 STM images of long-chain alkane monolayers on graphite

To verify my results for the preferential adsorption geometry of polyethylene or finite alkane chains on graphene, I compare the optimized structures to STM images of the corresponding systems. Since scanning tunneling microscopy only images electronic states in the energy range $E_F - eV_{bias} < E < E_F$, where V_{bias} is the bias voltage and E_F is the Fermi level, I must further inspect the electronic structure of polyethylene on graphene to interpret the images.

Results for the electronic density of states (DOS) of polyethylene on graphene
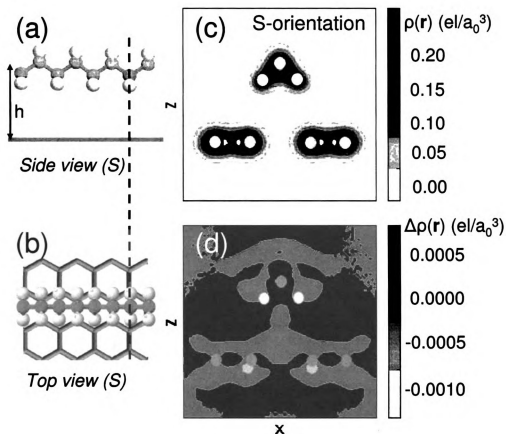
Figure 6.5: Nature of bonding of polyethylene in S orientation, standing normal to graphene. The polyethylene adsorption geometry on graphene, shown (a) in side view and (b) in top view. Contour plots of (c) the total charge density $\rho_{PE/gra}(\mathbf{r})$ and (d) the charge density difference, defined as $\Delta\rho(\mathbf{r}) = \rho_{PE/gra}(\mathbf{r}) - \rho_{PE}(\mathbf{r}) - \rho_{gra}(\mathbf{r})$. The plane of the contour plots is normal to the polymer axis and is indicated by the dashed line in (a) and (b).

are presented in Fig. 6.6. In Fig. 6.6(a) I compare the DOS of pristine graphene to polyethylene/graphene in P- and S-orientation. As seen in Fig. 6.1(b), polyethylene is a wide-gap insulator with a fundamental gap exceeding 7.5 eV and becomes visible to the STM only in the energy range, where the electronic states of PE-covered graphene display a significant PE character. I expect a non-vanishing polyethylene character at those energies, where the DOS of PE on graphene differs from the pristine graphene substrate. This can be best judged by inspecting the difference density of states ΔDOS for P-oriented PE in Fig. 6.6(b) and that of S-oriented PE in Fig. 6.6(c).

These results suggest that no signal related to polyethylene should occur at bias voltages $V_{bias} \lesssim 1.4$ V when imaging the occupied states.

Calculated and observed STM images of self-assembled alkane monolayers on graphene are shown in Fig. 6.7. STM images obtained in the constant current mode display changes of the tip height h as a function of the lateral tip position (x, y). The
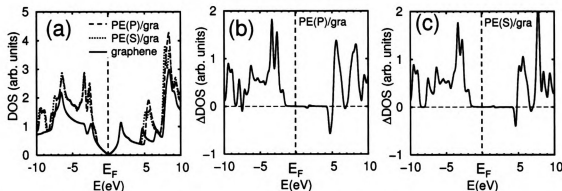
Figure 6.6: (a) Density of states (DOS) of polyethylene (PE) monolayers in P- and S-orientation on graphene, compared to the DOS of pristine graphene. The DOS has been convoluted by 0.2 eV. (b) Difference density of states $\Delta DOS(\text{PE(P)/gra}) = DOS(\text{PE(P)/gra}) - DOS(\text{graphene})$ for P-oriented PE. (c) Difference density of states $\Delta DOS(\text{PE(S)/gra}) = DOS(\text{PE(S)/gra}) - DOS(\text{graphene})$ for S-oriented PE.
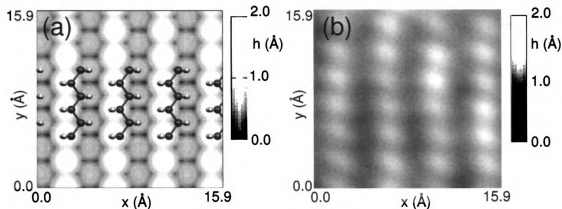
Figure 6.7: Scanning tunneling microscopy (STM) images of self-assembled alkane monolayers on graphene at the bias voltage $V_{bias} = 2.0$ V (sample negative). (a) Calculated STM image of a polyethylene (PE) monolayer on graphene, corresponding to a constant charge density $\rho_{STM} = 10^{-6}$ e/a_0^3. The image is superimposed with the model of the PE structure. (b) STM image of an n-docosane monolayer on graphene, observed at the constant tunneling current of 215 pA.

corresponding calculated images display the height $h(x, y)$ corresponding to a given value of the charge density ρ_{STM} that is associated with states in the range $E_F - eV_{bias} < E < E_F$. The calculated STM image in Fig. 6.7(a), obtained for $V_{bias} = 2.0$ V and $\rho_{STM} = 10^{-6}$ e/a_0^3, can be directly compared to STM images obtained in the constant-current mode at the same bias voltage. Superposed to the calculated image in Fig. 6.7(a) is the underlying structure of P-oriented polyethylene chains, aligned along the zigzag direction of graphene and separated by 4.26 Å, commensurate with the underlying graphene layer. Comparison between the calculated STM image and the underlying polymer structure indicates that the bright spots in the image closely correlate with the position of H atoms of the alkane chains. As mentioned above, due to the small horizontal tilt of polyethylene on graphene, the hydrogen atoms on the right-hand side of the polymer in Fig. 6.7(a) are closer to graphene by 0.2 Å and thus could naïvely be expected to be observed at a slightly smaller height than those on the left-hand side of the chains. At the finite bias voltage used in the STM, however, the height contours are not directly correlated with atomic positions. In the present case, the small height difference of 0.2 Å between the hydrogen atoms translates into a much larger apparent height difference of 0.6 Å in STM images observed at $V_{bias} = 2.0$ V.

Figure 6.7(b) shows STM data obtained when imaging a solution of n-docosane in 1-phenyloctane on graphite at $V_{bias} = 2.0$ V (sample negative), at the constant tunneling current of 215 pA. The STM image, obtained using a tip submersed in the solution, shows a well-formed self-assembled monolayer of n-docosane, closely resembling my calculated image of Fig. 6.7(a) showing atomic resolution.
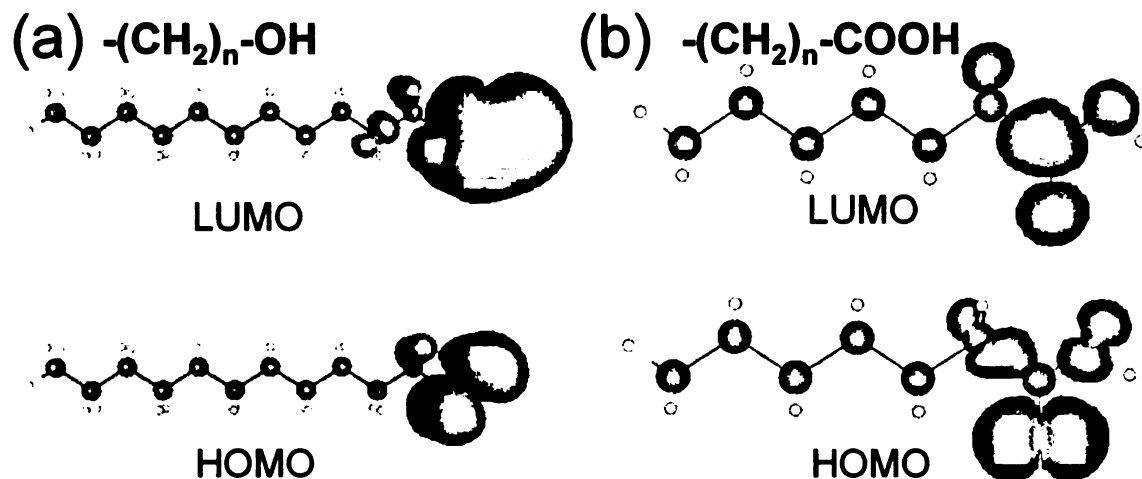
Figure 6.8: Highest occupied (HOMO) and lowest unoccupied (LUMO) molecular orbitals of polyethylene chains terminated by (a) an OH group and (b) a COOH group. Charge density contours are superposed with ball-and-stick models of the molecules.

6.4.5 Structure and stability of long-chain alkane derivatives on graphite

Next, I studied the effect of alcohol and carboxylic acid functional groups on the adsorption geometry and the corresponding STM images. Whereas the frontier orbitals of polyethylene or unmodified alkane chains extend along the entire chain, as seen in Fig. 6.1(c) and 6.1(d), this is generally not the case with molecules possessing terminal functional groups. Since frontier orbitals are very important for understanding the interaction and optimum alignment of molecules, I plot the charge density associated with the highest occupied (HOMO) and lowest unoccupied (LUMO) molecular orbitals of polyethylene chains terminated by an OH group in Fig. 6.8(a) and those of COOH-terminated polyethylene in Fig. 6.8(b).

These functional groups introduce new localized states between the top of the valence and bottom of the conduction band of polyethylene, which become frontier states and reduce the fundamental gap. Inspection of Fig. 6.8 suggests that the frontier states are localized near the functional groups.
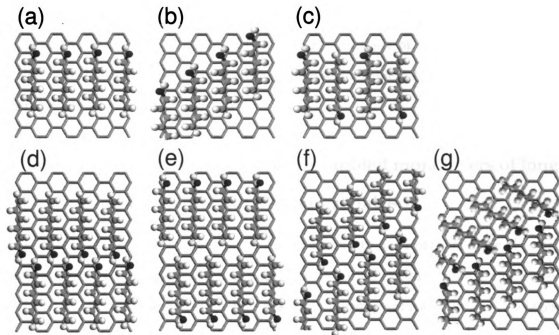
Figure 6.9: Adsorption arrangements in finite-width domains of straight chain alcohols in self-assembled monolayers on graphene. Common to all structures is the P-orientation of the alkyl chains and their alignment along the zigzag direction on graphene. Adjacent chains within one domain can be parallel, with OH groups pointing in the same direction, or antiparallel, with OH groups pointing in opposite directions.

Possible adsorption arrangements of long chain alcohols within self-assembled monolayers on graphene are displayed in Fig. 6.9. The relative stability of the different

Structure	E_{ad}
(a)	-1.00 eV
(b)	-0.95 eV
(c)	-0.98 eV
(d)	-1.45 eV
(e)	-1.03 eV
(f)	-1.20 eV
(g)	-1.60 eV

Table 6.1: Relative stability of finite-width domains of $C_6H_{13}OH$ in self-assembled monolayers on graphene. The structure labels correspond to the adsorption arrangements of Figs. 6.9(a)-(g). The adsorption energy E_{ad} of $C_6H_{13}OH$ is given by $E_{ad} = E_{tot}(C_6H_{13}OH$ array/graphene$)-E_{tot}$(isolated $C_6H_{13}OH$ in vacuum$)-E_{tot}$(graphene).

arrangements depends upon whether the alcohol functions are arranged head-to-head or head-to-tail within a domain, and also upon the nature of the domain boundary. Relative stabilities of these systems are compared in Table 6.1 for the arrangements displayed in Fig. 6.9.

6.4.6 Domain formation in self-assembled monolayers of long-chain alkane derivatives on graphite

Within an isolated domain, which contains head-to-head parallel or head-to-tail antiparallel OH-terminated alkanes, possible adsorption arrangements are displayed in Figs. 6.9(a)-(c). The corresponding adsorption energy values in Table 6.1 suggest that the parallel arrangement of Fig. 6.9(a), with all alcohol ends aligning head-to-head along a domain edge normal to the chains, is most stable. The staggered parallel arrangement of Fig. 6.9(b), with the domain edge at a 30° angle to the chains, is least stable. The antiparallel arrangement of Fig. 6.9(c), with the alcohol ends aligning head-to-tail along a domain edge normal to the chains, is not as stable as the parallel head-to-head arrangement of Fig. 6.9(a). Nevertheless, since it contains a shorter domain boundary than the staggered arrangement of Fig. 6.9(b), the arrangement of Fig. 6.9(c) lies energetically between those of Fig. 6.9(a) and Fig. 6.9(b).

Possible boundaries between domains of long chain alcohols are considered in Figs. 6.9(d)-(g). All these arrangements are energetically preferred over those for a single domain with the energetically taxing open edge. In long chain alcohols, the OH bond direction forms a 60° angle to the axis of the alkyl chain. Among the many ways to assemble long chain alcohols into a monolayer superstructure, arrangements that from H-bonds at the domain boundary are energetically preferred [129]. The chain directions within the SAMs are furthermore constrained by the symmetry of the underlying graphene lattice, which allows lamellar directions in adjacent domains to be either parallel or to form a 120° angle.

Figures 6.9(d)-(e) depict head-to-head and tail-to-tail alignment of long chain alcohols at the boundary of adjacent domains, in which all long chain alkyls are aligned parallel to one another. The head-to-head alignment provides additional hydrogen bonding at the interface, thus stabilizing the structure of Fig. 6.9(d) over that of Fig. 6.9(c). In the arrangement of Fig. 6.9(f), the parallel alignment of all long chain alcohols in adjacent domains is maintained, but the domain boundary is rotated by 30° with respect to the alkyl axis. Even though hydrogen bonding stabilizes this arrangement over that of Fig. 6.9(e), the longer boundary length makes it energetically unfavorable relative to the arrangement of Fig. 6.9(d).

The symmetry of the underlying graphene lattice also allows long chain alcohols of two different domains to meet at a 120° angle, as shown in Fig. 6.9(g). Since the arrangement of the terminal OH groups at the domain boundary in Fig. 6.9(g) is most favorable among all the arrangements discussed here, I expect it to occur frequently in the self-assembled monolayers.

My findings for self-assembled monolayers of alkane derivatives with COOH functional groups are qualitatively similar to those discussed in Fig. 6.9. However, the energy to separate a pair of facing carboxylic acid molecules (so-called carboxylic acid dimers), $\Delta E_b = -1.72$ eV, is more than three times larger than the separation energy $\Delta E_b = -0.47$ eV of a pair of facing alcohol molecules.

6.4.7 STM images of monolayers of long-chain alkane derivatives on graphite

To help identify the location of OH and COOH functional groups in self-assembled monolayers of long chain alcohols and carboxylic acids, I calculated the corresponding STM images of $C_6H_{13}OH$ and $C_6H_{13}COOH$ assemblies on graphene. My results, shown in Fig. 6.10, suggest that the OH terminal group should appear at a larger apparent height, whereas the COOH group should appear at a smaller ap-

parent height than the alkane chain in STM images obtained in the constant current mode. Figure 6.11 displays STM images and corresponding structural models of self-assembled monolayers of 1-docosanol ($C_{22}H_{45}OH$) and 1-docosanoic acid ($C_{22}H_{45}COOH$) molecules on graphite. According to Fig. 6.7, I associate the lamellar structure with parallel alkane chains. For illustration purposes, the length of fully stretched (all s-trans conformations) docosanol ($l = 29.5$ Å) and docosanoic acid ($l = 30.8$ Å) molecules is indicated in the figure. The STM images in Figs. 6.11(a) and 6.11(c) suggest the presence of stripe-shaped domains that are split in the middle into sub-domains spanned by parallel arrays of the alkane derivatives.

According to my calculations, the equilibrium separation between docosanol chains in the S-orientation is 3.50 Å, incommensurate with the graphene lattice, which agrees well with the inter-chain separation in domains (1) and (2) of Fig. 6.11(a). Similarly, the predicted equilibrium separation of P-oriented docosanol chains of 4.26 Å agrees well with the observed inter-chain separation in domains (3) and (4) of Fig. 6.11(a). My energy results in Table 6.1 suggest that hydrogen bonds stabilize the interface between adjacent domains of head-to-head aligned long chain alcohols.
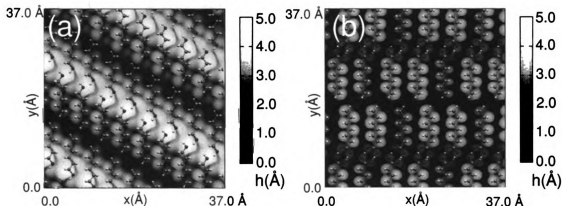
Figure 6.10: Calculated STM images of alkane derivatives forming self-assembled monolayers on graphene. (a) $C_6H_{13}OH$ at the bias voltage $V_{bias} = 1.6$ V, (b) $C_6H_{13}COOH$ at $V_{bias} = 1.3$ V (sample negative). Charge density contours for $\rho_{STM} = 10^{-6}$ e/a_0^3 are superimposed with structural models. The y-axis is aligned along the zigzag direction of the underlying graphene.

As a plausible working hypothesis, I will assume that the sub-domains in Fig. 6.11(a)
contain OH groups at both sides of the interface, with hydrogen bonds acting as a
stabilizing element of the semi-rigid domain backbone. This assumption is confirmed
by the observation of the largest apparent height in the STM image of Fig. 6.11(a) in
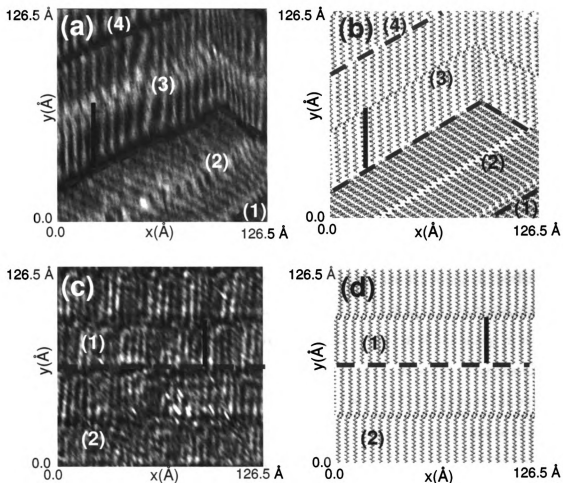
Figure 6.11: STM images (a,c) and structural models (b,d) of alkane derivatives
forming self-assembled monolayers (SAMs) on graphite. (a) Observed and (b) model
structure of 1-docosanol ($C_{22}H_{45}OH$) on graphite. (c) Observed and (d) model
structure of 1-docosanoic acid ($C_{22}H_{45}COOH$) on graphite. The STM image (a) was
obtained using the bias voltage 1.6 V (sample negative) at the constant tunneling
current of 30 pA, the STM image (c) was obtained using 1.3 V (sample negative)
bias and a 25 pA current. Domains are labeled by numbers. The size of individual
molecules is indicated by a black rectangle in each panel. The OH and COOH terminal
groups are emphasized in red in (b) and (d), and the domain boundaries are indicated
by the heavy dashed lines.

the middle of the domains, in accordance with predicted STM images for this molecular arrangement, shown in Fig. 6.10(a). Combining all this information is sufficient to present a well-defined structural counterpart to the STM image of Fig. 6.11(a) in Fig. 6.11(b).

A similar interpretation can be applied to the STM image of docosanoic acid monolayers in Fig. 6.11(c). The predicted equilibrium separation between P-oriented docosanoic acid chains in the P-orientation is 5.50 Å, incommensurate with the graphene lattice, which agrees well with the inter-chain separation in the domains of Fig. 6.11(c). Also in this case, the domains are stripe-shaped and contain two sub-domains, each spanned by an array of docosanoic acid molecules. As in the case of the alcohol terminal group, the acid groups favor a head-to-head configuration at the interface of the sub-domains, which provides the domain with a stabilizing backbone. Unlike in alcohols, where the chains may either be parallel or form a 120° angle, the alkyl chains in carboxylic acid SAMs have a strong energetic preference for being parallel. Also, the interaction between head-to-head acid terminal groups of alkanes is more than three times larger than in the alcohols, resulting in a very rigid, straight domain backbone that is normal to the chain direction. The postulated head-to-head alignment of the acid groups in the middle of the domain can not be verified easily, since the predicted apparent height of the acid terminal group in STM images of monolayers is only slightly smaller than that of the alkane, showing very little contrast.

6.5 Discussion

The favored structure of bulk polymer melts at high temperatures is known to depend largely on entropy. I believe that the relevant degrees of freedom are largely frozen out when polymers self-assemble to ordered monolayers on a substrate, thus

significantly reducing the configurational part of entropy. I furthermore assume that other contributions, including configurational entropy, may be nearly equal in systems I compare, thus justifying *a posteriori* my discussion of stability differences based on total energy calculations performed at $T = 0$.

The formation of ordered overlayers of long chain alkanes and their derivatives on graphite out of their solution in phenyloctane is a slow process. After an initial fast adsorption stage, it takes several minutes at room temperature to complete the ordering in the self-assembled monolayers. Once a domain structure is formed, domain walls are observed to move in time [49]. Assuming that the presence of the solvent does not affect the adsorption energy hierarchy in Table 6.1, the most stable structure at $T = 0$ would consist of infinite stripe domains. The favored lamellar structure of long chain alcohols would be a 120° chevron pattern, locally represented in Fig. 6.9(g). In the corresponding structure of long chain acids, the lamellae should be all parallel and aligned normal to the domain walls, as seen in Fig. 6.9(d). At nonzero temperatures, configurational entropy should introduce roughening of the domain walls. Moreover, the assumption that the solvent does not affect the adsorption geometry hierarchy is not very well founded, since the adsorption energy of phenyloctane molecules on graphite is only slightly smaller than that of alkanes and their derivatives of a comparable size. Thus, the real SAM patterns may deviate on energy and entropy grounds from the $T = 0$ equilibrium structure.

In reality, the origin of the complex patterns in Figs. 6.11(a) and 6.11(b) is only partly related to stability issues, since the relatively slow self-assembly process has an important kinetic component. Alkane chains are likely to adsorb simultaneously at different substrate locations and assemble to domains that grow in size, until they hit the next domain. At this moment, the two domains will attempt to minimize the interface energy by local rearrangements. Since the assembly process is relatively slow, I expect these rearrangements not to yield the globally optimized structure.

In general, I expect an energy-related compromise structure of the adsorbate layer subdivided into large domains with straight edges. Energetic compromises, resulting in a complete monolayer coverage, may include unfavorable adsorbate orientation, including the S-oriented domains (1) and (2) in Figs. 6.11(a) and 6.11(b) that may form under lateral pressure. Rather than forming void islands, the system may accept the formation of energetically unfavorable domain wall boundaries, such as that between domains (2) and (3) in Figs. 6.11(a) and 6.11(b).

As mentioned above, the strong interaction between head-to-head terminal groups of long chain acids favors only one domain structure with all chains parallel and the domain boundaries normal to the chain direction. Due to the high stability and rigidity of this assembly, I expect straight stripe domains to cover the entire sample, with diminished effects of entropy, presence of the solvent, or kinetics. Indeed, the pattern observed in Fig. 6.11(c) is nearly free of defects and identical to the optimum structure expected at $T = 0$.

6.6   Summary and conclusions

In summary, this study combined scanning tunneling microscopy observations with *ab initio* calculations to study the self-assembly of long chain alkanes and their derivatives on graphite. I identified the optimum adsorption geometry of polyethylene, long chain alkanes, alcohols and carboxylic acids on graphite. Calculated adsorption energies in different arrangements were used to predict the optimum structure of self-assembled monolayers. Theoretical predictions for STM images of optimized adsorbate overlayers were compared to the experimental data for docosane, docosanol and docosanoic acid on graphite. My total energy results provided a sound base for interpreting the observed domain wall structure in the self-assembled monolayers. In particular, I found that the observed domain wall structure in docosanol

SAM superstructures should vary from sample to sample, since kinetic processes are as important as structural stability. In docosanoic acid SAM superstructures, the interaction between COOH terminal groups at the domain wall boundary is much stronger, resulting in patterns reflecting the globally optimized structure, with no sample-to-sample domain variation. These results can be directly used when designing templates to be used in template directed nanoassembly and transfer processes. Finally, since nearly any nanoparticle can be attached to long chain molecules, including those described here, self-assembly of such molecules or polymers provides an efficient means to prepare ordered arrays of uniformly spaced nanoparticles.

Chapter 7

Molecular self-assembly of functionalized fullerenes on a metal surface

The following discussion is closely related to a publication by Bogdan Diaconescu, Teng Yang, Savas Berber, Mikael Jazdzyk, Glen P. Miller, David Tománek, and Karsten Pohl, Phys. Rev. Lett. **102**, 056102 (2009) [130]. This study is a collaborative project with an experimental group at the University of New Hampshire. Even though my contribution is limited to calculations in the theoretical part, results of the entire study are reproduced in the following as an example, how a Theory-Experiment collaboration can help to understand nanoscale phenomena.

7.1 Introduction

Ordered arrays of molecules or nanoparticles such as C_{60} fullerenes have a great number of practical applications, ranging from sensors and biological interfaces [50] to organic electronics [51], photovoltaics, and novel computational methods such as quantum dot cellular automata and, with endohedral fullerenes, a spin-based quantum

computer [52, 53]. Generally speaking, self-assembled monolayers of molecules (SAM) form as a result of a delicate balance between competing molecule-substrate and intermolecular interactions [54]. Therefore, to control such self-assembly processes and grow molecular arrays of designed geometries, it is mandatory to understand how this balance reflects onto the SAM's final structure [55].

Here I describe a novel way of controlling the self-assembly process and designing the structure of self-assembled monolayers via chemical functionalization of the fullerene cages. Self-organization of fullerene cages in ordered arrays at desired non close-packed distances can be achieved by controlling the hierarchy of interactions within the SAM, in accordance with *ab initio* total energy calculations. The scanning tunneling microscopy (STM) images, obtained by my experimental colleagues, show that C_{60} fullerene cages functionalized with two long alkane tails (Fig. 7.1(a)), once grown onto the close-packed surface of Ag, self-assemble into parallel zigzag rows (Fig. 7.1(b)), the separation of which is determined by the length of the tails.

My colleagues synthesized [131] this fullerene derivative with multiple supramolecular synthons in order to exploit several intermolecular interactions during assembly on Ag(111). These interactions include fullerene–fullerene π–π stacking interactions [132, 133], alkyl–alkyl inter-chain interactions and substrate–molecule interactions. The peculiar dimerization pattern in the zigzag rows can be traced back to a conformational change of the functionalized C_{60} molecule (F-C_{60}) upon adsorption. The conformational change and the self-assembled molecular pattern are a consequence of a hierarchy of interactions within the SAM, which can be explained by *ab initio* density functional theory calculations (DFT).

In this combined experimental and theoretical investigation, we studied self-assembled monolayers on an atomically flat thin film of silver used as substrate. The Ag film, with a thickness of two atomic Ag layers or more, was grown on the (0001) surface of a single crystal ruthenium sample by physical vapor deposition under
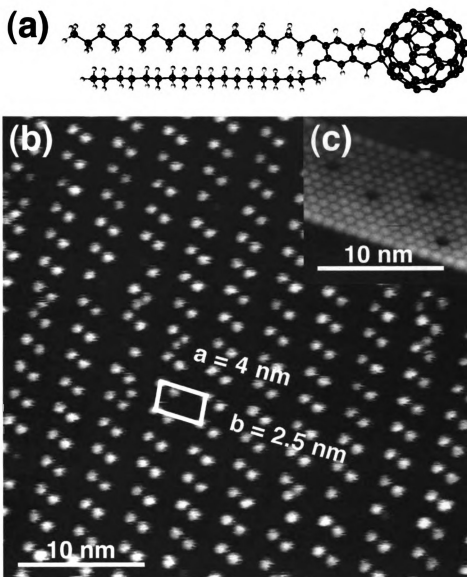
Fig. 7.1: Self-assembled monolayer of F-C$_{60}$ on Ag(111). (a) Equilibrium structure of an isolated F-C$_{60}$ molecule; carbon atoms are shown in green, oxygens in red, and hydrogens in grey. (b) STM constant current image of F-C$_{60}$ SAM (295 K, −1 V sample bias, 0.4 nA tunneling current) also showing the geometry of the unit cell of the molecular structure. (c) Island of pristine C$_{60}$ on Ag(111) imaged in identical conditions (295 K, −1 V, and 0.4 nA).
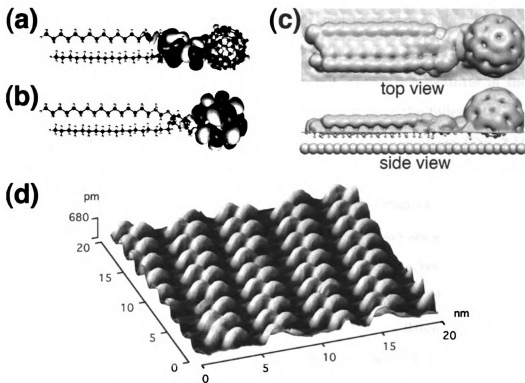
Fig. 7.2: F-C$_{60}$ STM signature. Wavefunctions of (a) the HOMO and (b) the LUMO of the free F-C$_{60}$ molecule, superposed with the atomic structure. (c) Calculated contours of constant local density of states for an F-C$_{60}$ molecule on Ag(111) representing constant current STM images under experimental conditions. (d) 3D representation of the STM data showing the corrugation of the F-C$_{60}$ SAM (295 K, –1 V sample bias, 0.4 nA tunneling current).

ultrahigh vacuum (UHV) conditions and has a (111) orientation. Functionalized C$_{60}$ [131] molecules (Fig. 7.1(d)) have then been deposited *in situ* on freshly prepared Ag films by low temperature sublimation at about 520 K. Following the F-C$_{60}$ deposition, annealing of the sample at 420 K to 470 K was performed for a few minutes in order to increase the size of the ordered SAM domains. The sample preparation and analysis took place in a home-built variable temperature STM operating in UHV at a base pressure of 1×10^{-10} torr [134]. The STM data presented here were acquired at room temperature (295 K).

Figure 7.1(b) shows a constant current STM image of an ordered domain of F-C$_{60}$ molecules. The molecular 2D superstructure forms a 4 nm × 2.5 nm oblique unit

cell with a sharp angle of about 80°, in stark contrast to the triangular close-packed arrangement of pristine C_{60} grown in UHV conditions on an identically prepared Ag(111) surface (Fig. 7.1(c)). The bright spherical symmetrical features in the F-C_{60} SAM image, shown in Fig. 7.1(b), are the fingerprint of the fullerene cages, as tested against pure fullerenes imaged in identical tunneling conditions (Fig. 7.1(c)). The darker areas between those features correspond to the regions where the alkane chains lie down on the Ag(111) surface. The measured distances between the first and second nearest neighbor fullerene cages in the STM images are about 1.6 nm and 2.0 nm. These distances are larger than the C_{60}-C_{60} close-packed interaction distance of 1.0 nm (Fig. 7.1(c)) [135]. It is somewhat surprising that the functionalized fullerenes do not assemble in such a manner as to maximize fullerene-fullerene $\pi - \pi$ stacking interactions given that fullerenes are known to assemble on Ag into hexagonal close packed 2D island domains [135] as seen in Fig. 7.1(c). The implication is that fullerene-fullerene $\pi - \pi$ stacking interactions are weaker than other prevailing interactions that drive the patterning during assembly.

Since experimental data had low contrast associated with individual F-C_{60} alkane tails (presumably because of the high corrugation of the SAM), a detailed analysis of the F-C_{60} STM signature is needed. Interpretation of the STM images is often counter-intuitive since the tunneling current is correlated with wavefunctions near the Fermi level rather than atomic positions. This is best illustrated by plotting the charge distribution associated with the highest occupied molecular orbital (HOMO) and the lowest unoccupied molecular orbital (LUMO) as shown in Figs. 7.2(a)-7.2(b). When adsorbed on the Ag(111) surface, the nature of states imaged by STM changes dramatically due to the hybridization between the electronic states of the substrate and the molecular orbitals of F-C_{60}. Calculated contours of constant tunneling current for F-C_{60} shown in Fig. 7.2(c), match the experimentally observed high corrugation of 0.65 nm of the SAM, shown in Fig. 7.2(d).
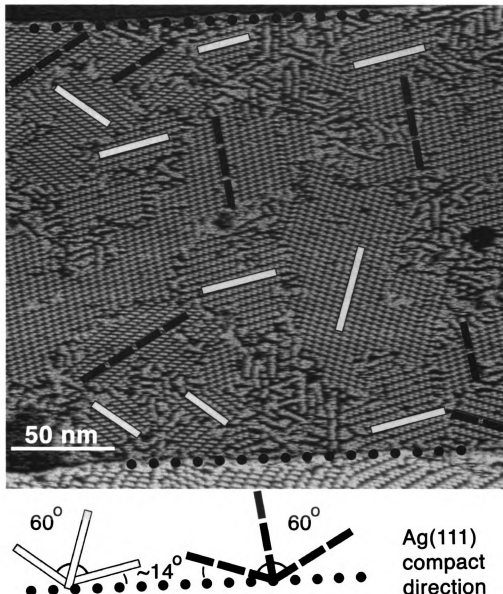
Fig. 7.3: Large scale STM image of F-C$_{60}$ SAM on 2 ML Ag/Ru(0001). The terrace edges of the Ag(111) substrate, corresponding to one of its compact directions, are marked by black dotted lines. The F-C$_{60}$ self-assemble in domains with six different orientations, shown schematically in the bottom diagram. We distinguish two domain groups, characterized by the solid bright green and dashed dark blue lines. Each group contains three types of domains with distinct orientations, separated by 60°. Any domain of one group is related to a domain of the other group by reflection symmetry on a compact direction of Ag(111). The sharpest angle between any domain direction and a Ag(111) compact direction is 14°.

Significantly more crystallographic information about the F-C_{60} SAM structure can be obtained from larger scale STM images. Fig. 7.3 shows all the observed orientations of the F-C_{60} ordered domains. The image also contains two Ag steps oriented along a compact direction of the (111) surface. I see that the F-C_{60} SAM domains are oriented in six distinct directions, identified by lines coinciding with the direction of the short side of the unit cell in Fig. 7.1(b). These domains can be subdivided into two groups containing three distinct directions, separated by 60° (since lines have no direction, there is a trivial reduction from 6 to 3 angles in each group). These two groups of sixfold symmetries suggest a preferential orientation of the F-C_{60} molecules with the alkane tails aligned along a high symmetry direction on Ag(111), such as the most and the least compact direction of the substrate. Any domain of one group is related to a domain of the other group by a reflection operation on a compact direction of Ag(111), under which the Ag(111) surface is invariant. This finding suggests that the F-C_{60} molecule possesses two mirror image configurations once adsorbed onto the metal surface.

7.2   Computational details

To obtain fundamental insight into the origin of the SAM pattern of F-C_{60} molecules on Ag(111), I determined the equilibrium geometry, binding energy and electronic structure of these systems via *ab initio* DFT calculations [125]. I use the local density approximation and the Perdew-Zunger [136] parametrization of the exchange-correlation functional. Most total energy calculations were performed using the Quantum-ESPRESSO code [81] with ultrasoft pseudopotentials [137] and employing a plane wave basis with a 25 Ry kinetic energy cutoff. I calculated the charge density in real space on a mesh equivalent to a 200 Ry cutoff energy, and used Ag pseudopotentials containing $4d$ semicore orbitals. I sampled the Ag(111) Brillouin

zone by a 32×32×1 k-point mesh and adjusted the mesh density for F-C$_{60}$/Ag(111) systems with larger unit cells. The vacuum region between 2D slabs was taken larger than 1 nm to minimize the inter-layer interaction.

Selected structure optimizations were performed using the SIESTA code [87] with a double-ζ polarized basis localized at the atomic sites. The valence electrons were described by norm-conserving Troullier-Martins pseudopotentials [89] in the Kleinman-Bylander factorized form [92]. I used the counterpoise method [94] to avoid basis-set superposition errors (BSSE) introduced by the localized basis and found the BSSE corrected local basis results in good agreement with my plane-wave results. I used $1-4$-layer slab representations of Ag(111) and periodic boundary conditions. In the superlattice geometry, the slabs were separated by 2 nm in the normal direction and represented by orthorhombic unit cells containing $2-8$ silver atoms. The super-cells were sampled by a 32×32×1 k-point mesh. The self-consistent charge density was obtained using a real-space grid with a mesh cutoff energy of 250 Ry, sufficient to achieve a total energy convergence of better than 0.05 meV/atom.

7.3   The hierarchy of interactions

We next discuss separately the mutual interactions between the substrate, alkane chains, and fullerenes. The final structure of the F-C$_{60}$/Ag(111) monolayer will be determined by the hierarchy of interactions between these constituents.

Since the functional tail of F-C$_{60}$ contains alkane chain segments, I performed total energy calculations of infinite polyethylene chains adsorbed on Ag(111) along various directions. I found the adsorption energy of 0.22 eV along the most compact direction, with the carbon backbone parallel to the surface, and with the C atoms in the trough, to be the most stable. All adsorption energies are normalized per C$_2$H$_4$ segment of polyethylene. The energy cost to displace the polymer across the
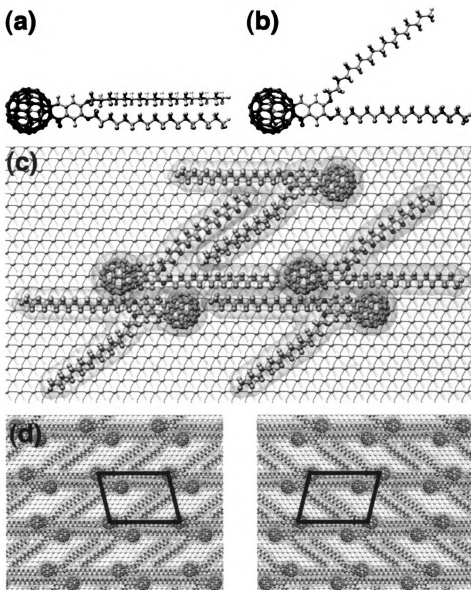
Fig. 7.4: Equilibrium configurations of free and adsorbed F-C$_{60}$ molecule: (a) top view in the I-shape configuration and (b) top view in the V-shape configuration. (c) Detail of the F-C$_{60}$ assembling in the optimum geometry. (d) Adsorbtion geometries of the F-C$_{60}$ SAM resulting from the proposed model. Besides the backbone of the F-C$_{60}$ molecules, I also depict the envelope associated with the Van der Waals radii of the atoms. The primitive unit cell depicted by the black lines, containing two F-C$_{60}$ molecules, agrees with the unit cell shown in Fig. 7.1(b).

surface, while maintaining its direction and orientation, is less than 0.02 eV per C_2H_4. Keeping the carbon backbone parallel to the surface, but changing the orientation from the most compact to the least compact direction, occurs at an energy cost of 0.01 eV. Displacing the chain across the surface in this orientation occurs at an even lower energy cost of less than 0.001 eV. Comparing polymers aligned along the same direction on the Ag(111) surface, I found that polymers with the backbone normal to the surface are less bound by 0.05 eV than polymers with the backbone parallel to the surface.

Although the alkyl chains of the free F-C_{60} molecules have many conformational degrees of freedom, the optimized geometry representing the global minimum (Fig. 7.1(a)) places the C backbones of the adjacent alkyl chains normal to each other. My calculations indicate that the alkane tail will gain 0.05 eV per C_2H_4 segment, thus favoring both alkane tails to adsorb with the C backbone plane parallel to the surface. In the free molecule, rotating one of the chains around the virtual hinge of a C-O bond to make the backbones co-planar, is associated with a moderate energy gain of about 0.2 eV. However, during this rotation, the chains assume the V-configuration (Fig. 7.4(b)), therefore eliminating the attractive interaction between the neighboring chains and as such necessitating a net energy investment of 0.42 eV for the entire F-C_{60} molecule. I find the equilibrium opening angle between the alkane chains in the optimized structure to be $30° - 40°$, which would be expected for rigid bonds and bond angles. The improved interaction between the chains and the substrate results in a net energy gain of 0.48 eV for the entire molecule, suggesting that adsorbed F-C_{60} molecules undergo a conformational change from the I-shape (Fig. 7.4(a)) to the V-shape (Fig. 7.4(b)) upon adsorption on Ag(111).

The fullerene adsorption energy on Ag(111) is sensitive to substrate relaxation and increases from 0.84 eV on a monolayer to 1.22 eV on a 4-layer slab, with energy differences below 0.03 eV depending on the orientation of the C_{60}, in qualitative

agreement with earlier results [138]. In equilibrium, depending on orientation, the center of the fullerene cage lies about $0.60 - 0.65$ nm above the Ag(111) surface.

Addressing separately the intermolecular interactions between various constituents, I found that adjacent C_{60} cages bind to each other with 0.15 eV at the equilibrium distance of 1 nm. Also, long chain alkanes bind with 0.27 eV to a fullerene cage, but interact very weakly with the phenyl rings connecting the C_{60} to the alkane tails. Finally, two infinite polyethylene chains, both with their C backbones parallel to the Ag(111) surface, experience an attractive interaction of 0.06 eV per C_2H_4 segment at their equilibrium separation of 0.43 nm [125] and a separation from the substrate of 0.32 nm.

The equilibrium structure of the F-C_{60} self-assembled monolayer on Ag(111) is illustrated in Figs. 7.4(c)-7.4(d). As discussed above, the chemisorbed F-C_{60} undergoes a conformational change from the I-shape (Fig. 7.4(a)) to the V-shape (Fig. 7.4(b)) configuration. The structure in Fig. 7.4(c) furthermore maximizes the interaction between the alkane chains and the C_{60} ends of the F-C_{60} molecules. The optimum angle between the chains of the F-C_{60} molecules, which is about 30° in Fig. 7.4(c), may be modified to some degree in order to maximize the inter-chain interaction. When optimizing the SAM geometry, I furthermore must consider the fact that the alkane tails lie much closer to the substrate than the fullerene cages, suggesting an apparent overlap between the two when viewed from top as probed by the STM tip. The orientation of the SAM on Ag(111) is likely given by the preference of at least one of the alkane tails in each F-C_{60} molecule to align along the most compact direction, as shown in Fig. 7.4(c). Moreover, the model generates all the possible orientations of the SAM with respect to the Ag(111) surface (Fig. 7.4(d)), observed as simultaneously occurring domains in Fig. 7.3. Thus, the self-assembly process selects molecules of given mirror configuration once adsorbed on the surface in individual domains. The overall calculated adsorption pattern therefore explains the observed unit cell

size and shape, including the distances between neighboring C_{60} ends of the F-C_{60} molecules. The alkane chain conformations are the reason for the formation of the intriguing asymmetric zigzag pattern observed here.

7.4 Summary and conclusions

Given the fundamental nature of my calculations and the good agreement with the experimental data, I can use the obtained insight to predict the behavior of related systems on other substrates. The pattern depicted in Figs. 7.4(c)-7.4(d) should not only occur on Ag(111), but on any substrate where the energetic preference for the alkane chains to adsorb with their backbones parallel rather than normal to the substrate is sufficiently large to initiate the V-shape configuration of Fig. 7.4(b). I also expect patterns with oblique, but larger unit cells, if the chain length in F-C_{60} increases. Other monolayer patterns could be obtained by changing the relative length of the alkyl chains attached to the C_{60} molecule.

Chapter 8

Optically induced transient structures in graphite

The following discussion is closely related to a publication by Ramani K. Raman, Yoshie Murooka, Chong-Yu Ruan, Teng Yang, Savas Berber and David Tománek, Phys. Rev. Lett. **101**, 077401 (2008) [139]. This study is a collaborative project with Prof. Ruan's experimental group at Michigan State University. Even though my contribution is limited to calculations in the theoretical part, results of the entire study are reproduced in the following as an example, how a Theory-Experiment collaboration can help to understand nanoscale phenomena.

8.1 Introduction

There is growing interest in displacing atoms in materials by photo-excitations [56]. Observations of transient structures thus formed offer a glimpse into the transformation pathways between different structures. Carbon, with its propensity to form a wide range of bonding networks (sp, sp^2, sp^3), is ideal to study the dynamics of bond formation and rupture. Of particular interest is the conversion of graphite to diamond [58, 59], which is believed to involve the rhombohedral phase of graphite as

intermediate state [60, 61]. Whereas pioneering ultrafast optical studies of graphite have provided evidence for photo-induced melting [62, 63] and generation of coherent phonons [64, 65] by observing changes in the electronic properties, direct determination of lattice structural dynamics from optical data proves difficult, especially in the far-from-equilibrium regime. X-ray diffraction has been successful in observing nonthermal structural changes in semiconductors [66], relying primarily on the integrated Bragg intensities. However, direct observation of atomic motion in nanostructures with low atomic number, such as carbon, has not yet been achieved. Electron diffraction, with its five orders of magnitude enhanced scattering cross-section and advanced schemes achieving femtosecond temporal resolution [67, 68, 69, 70], offers a new window into the realm of photo-excited structural dynamics, with resolution down to $\lesssim 1$ nm [67, 70, 71].

In this combined experimental and theoretical study, we report the first direct determination of structural changes induced in graphite by a femtosecond laser pulse. At moderate fluences of ≤ 21 mJ/cm^2, after a short thermalization period of ≈ 8 ps, we can attribute a temperature value to the graphitic layers and find the interlayer vibration amplitudes to match those reported in X-ray and neutron scattering studies [140]. At higher fluence values approaching the damage threshold, we observe lattice vibration amplitudes to saturate. Following a marked initial contraction of the interlayer spacing by $\leq 6\%$, graphite is driven nonthermally into a transient state with sp^3-like character, forming 1.9 Å long interlayer bonds. Using *ab initio* density functional theory (DFT) calculations, we trace the structural changes back to a nonthermal heating of the electron gas, followed by a photo-induced charge separation causing a compressive Coulomb stress.

The experimental setup, shown in Fig. 8.1(a), has been described in detail elsewhere [70]. Freshly cleaved samples of highly oriented pyrolytic graphite (HOPG) were placed inside an ultrahigh vacuum chamber through a load lock system at room
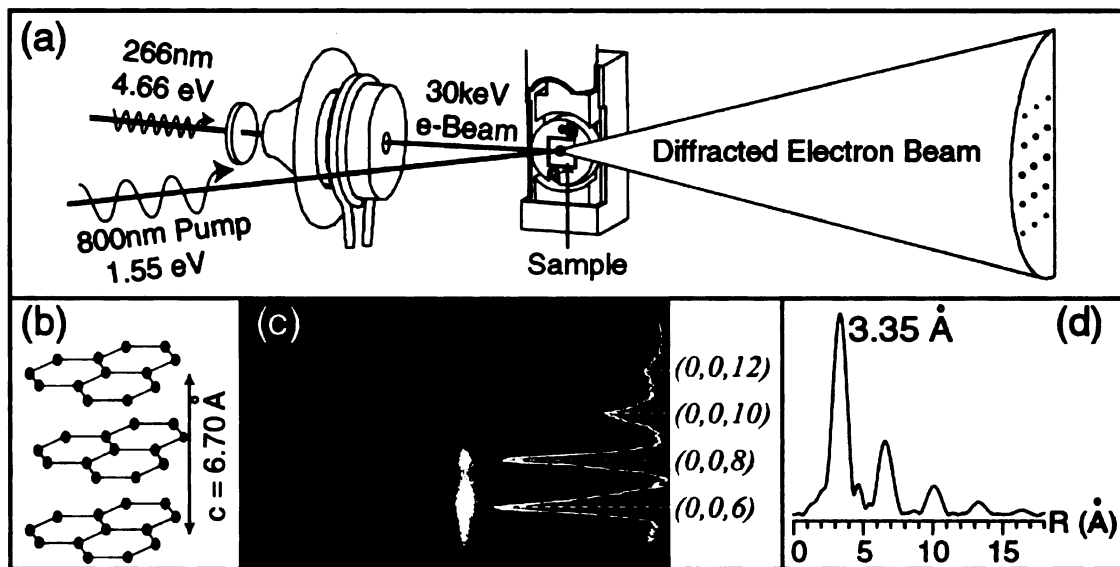
Figure 8.1: Ultrafast Electron Crystallography (UEC) of highly oriented pyrolytic graphite. (a) The UEC pump-probe setup. (b) The layered structure of graphite. (c) Ground state diffraction pattern of graphite. (d) Ground state layer density distribution function (LDF), obtained via a Fourier transform of the central streak pattern in (c).

temperature. A mode-locked Ti-Sapphire laser (p—polarized, 45 fs, 800 nm, 1 kHz) generated the pump pulse, which was marginally focused ($\approx$600 μm diameter) onto the sample at $\approx$45° relative to the HOPG c-axis. The range of the laser fluence $0.5 < F < 90$ mJ/cm² was below the *in situ* determined optical damage threshold of $\approx$120 mJ/cm².

A photo-generated 30 keV electron beam (wavelength $\lambda_e = 0.069$ Å), with diameter demagnified to ≤ 5 μm, was directed onto the sample at grazing incidence of 2.4° to serve as the probe. A translational optical delay stage was used to vary the relative delay between the arrival of pump and probe pulses at the sample, to observe the changes induced by laser irradiation. The electron pulse sampled the top $3 - 5$ layers of the graphite structure, depicted in Fig. 8.1(b), and produced oriented molecular diffraction patterns in the central streak region, shown in Fig. 8.1(c). The layer density distribution function (LDF), shown in Fig. 8.1(d), was obtained from the Fourier analysis of the interference pattern. The primary peak at 3.35 Å and

less pronounced peaks at 6.7 Å and $\approx$10 Å were found to be in good agreement with the layered structure of bulk graphite [140]. The decay of higher order LDF peaks suggest a probing depth of $\approx$1 nm.

To study the photo-induced structure dynamics, my experimental colleagues first examined the near-equilibrium regime at low fluences of 0.5 mJ/cm$^2 \leq F \leq 21$ mJ/cm^2. Random atomic displacements diminish the intensity of the diffraction spectra by a Debye-Waller factor e^{-2M}, where $M = -s^2 \bar{u}^2/4$, $\bar{u}^2$ is the mean-square atomic displacement perpendicular to the reflecting planes, and $s = (4\pi/\lambda_e) \sin(\theta/2)$ is the momentum transfer associated with the maxima located at the scattering angle θ. Thus, the change in the mean-square atomic displacement $\Delta \bar{u}^2$, measured relative to the unperturbed state at negative times, determines the rise in lattice temperature and can be calculated from the diffraction intensities as $\ln(I_s(t)/I_s(t<0)) = -s^2 \Delta \bar{u}^2/4$. In Ultrafast Electron Crystallography (UEC), we monitor the integrated intensity of the (0,0,6), (0,0,8) and the (0,0,10) maxima arising from the interference between the graphitic layers, shown in Fig. 8.2(a). The intensity of all 3 maxima drops within a timescale of 8 ± 1 ps, indicative of increased thermal motion of the graphitic planes. As we probe reflections from the basal planes, the observed intensity drops mainly due to the increased out-of-plane displacement of the atoms. Recent optical studies [64, 65] have associated near-infrared optical excitations in graphite with a femtosecond generation of coherent phonons with E_{2g} symmetry (interlayer shearing mode). Hence, this 8 ps timescale of interlayer thermal excitation is a direct measure of the phonon-phonon interactions in HOPG, and is in good agreement with reports of hot phonon relaxation times in graphite [141].

Quantitative analysis of the intensity drops in Fig. 8.2(a) indicates that the mean square atomic displacement $\Delta \bar{u}^2$ increases linearly with the applied fluence in the near-equilibrium regime, as seen in Fig. 8.2(b). Comparing our data to a theoretical model of temperature dependent $\Delta \bar{u}^2$, benchmarked with X-Ray and neutron
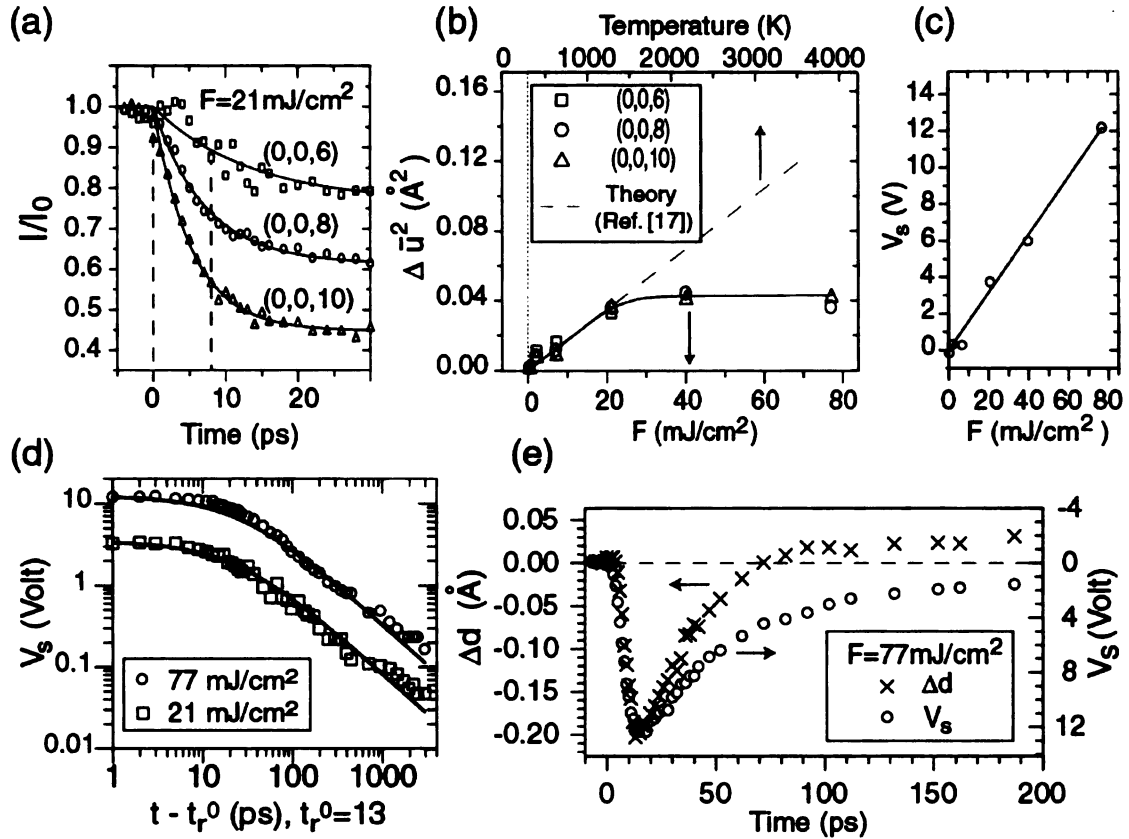
Figure 8.2: (a) Decay of the diffraction intensity. (b) Change in mean-squared atomic displacements perpendicular to the graphite planes, estimated from the Debye-Waller analysis of the intensity drops in (a). (c) Effective surface potential V_S at the HOPG surface as a function of the applied fluence F. (d) Decay of the effective surface potential with fit to the drift-diffusion recombination model (see text). (e) Contraction of the interlayer spacing Δd (left axis) and the corresponding increase in the effective surface potential (right axis) in the far-from equilibrium regime.

scattering data [140], we estimate a temperature rise of 950 K at $F = 21$ mJ/cm^2 in Fig. 8.2(b). This is also in good agreement with temperature extracted from optical studies using heat capacity and absorbance [63].

As we enter the far-from-equilibrium regime by increasing the excitation fluence beyond 21 mJ/cm^2, the amplitude of atomic vibrations saturates and no longer increases with increasing fluence, as seen in Fig. 8.2(b). This is rather surprising, for one would expect a monotonic increase in the thermal motion as graphite approaches its melting threshold at 130 mJ/cm^2 [63]. Furthermore, the (0,0,6) maximum is found

108

to shift by almost 0.34 $\mathring{A}^{-1}$ at $F = 40$ mJ/cm^2, which would correspond to an inter-planar expansion of 6%. Such a large peak shift cannot arise from structural changes alone.

We believe that the key effect of the optical excitation is the repopulation of electronic states, causing re-bonding and redistribution of charge at the surface[142]. This charge redistribution gives rise to a Coulomb field near the graphite surface, which induces a collective shift of the electron diffraction pattern. We measure this Coulomb field here directly by modeling the 'refraction' effect commonly associated with the existence of a surface potential at the vacuum-material interface [142]. We deduce the effective surface potential V_s as a function of the applied fluence and find it to increase linearly up to $F \approx 80$ mJ/cm^2, as shown in Fig. 8.2(c). This linear trend indicates that the surface charging is mainly driven by the non-equilibrium diffusion of photogenerated carriers rather than multiphoton ionization. The decay of this transient surface potential resulting from the recombination of space charge follows a power-law decay with the exponent -1, as shown in Fig. 2(d) and predicted by the drift-diffusion recombination model [142].

To examine the effect of optical excitations on the atomic structure at these elevated fluences, we monitored the interlayer separation following the photo-excitation by a time-resolved LDF analysis, after having accounted for the surface potential effects. In contrast to the thermal expansion at low fluences, we observed the interlayer separation to contract rapidly, as seen in Fig. 8.2(e). The change in the interlayer spacing Δd is found to correlate well with the rise and fall of V_s at $F = 77$ mJ/cm^2, with a maximum value $V_s \approx 12$ V corresponding to an interlayer contraction of $\approx 6\%$. The potential rise V_s sampled within the electron probe depth of 1 nm yields an internal field of $E \approx 1.2$ V/ $\mathring{A}$, which causes Coulomb stress. Using this value of E and $\epsilon_r = 10$ for graphite, we estimate a maximum energy density of $U_e = \epsilon_r \epsilon_0 E^2/2 = 0.2$ eV/atom, close to the ≈ 0.3 eV/atom value based on DFT for the activation barrier in the
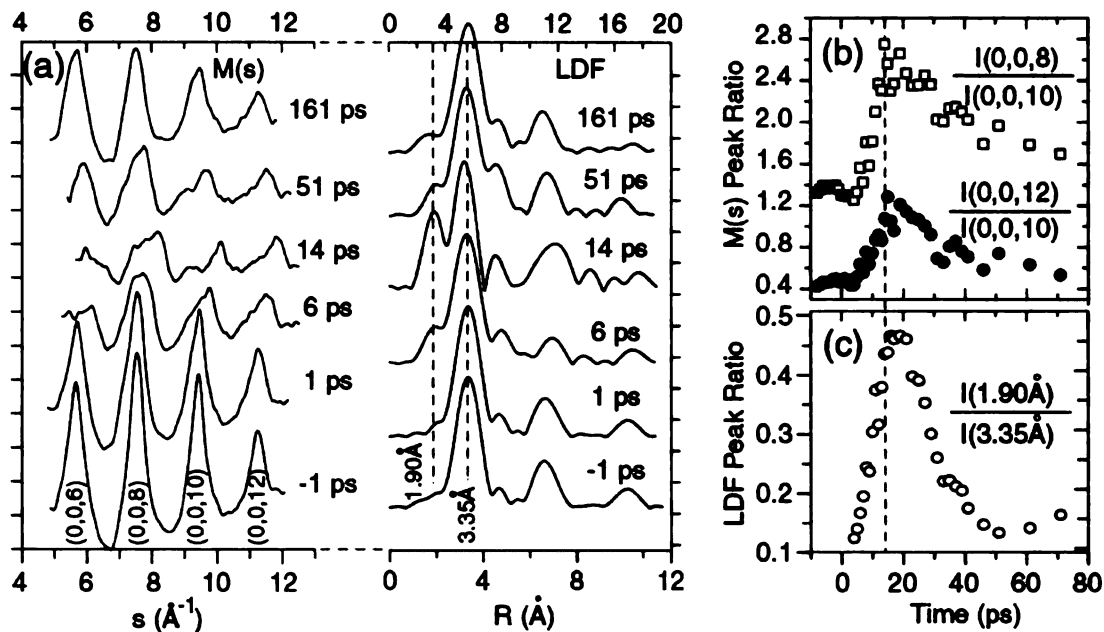
Figure 8.3: Signature of sp^3-like bonding in HOPG. (a) Molecular interference pattern $M(s)$ and the corresponding LDF curves at selected time stances following strong photo-excitation. The transient peak at 1.9 Å in the LDF indicates formation of an interlayer bond. (b) Ratio of peak intensities obtained from the diffraction patterns. The enhancement of the $(0,0,12)$ with respect to the $(0,0,10)$ peak cannot be explained by thermal vibrations and indicates a transient structure consistent with sp^3 bonding. (c) Ratio of peak intensities at $R = 1.9$ Å and 3.35 Å in the LDF.

graphite-to-diamond transformation [60, 59].

To further elucidate the structural evolution, we examined closely the diffraction spectra. Figure 8.3(a) shows the time evolution of the molecular interference curves $M(s)$ and the corresponding LDF curves at $F = 77$ mJ/cm^2, just below the damage threshold. Starting at ≈ 6 ps, as V_s rises beyond 4 V, we observe the onset of peak shouldering and broadening in the $M(s)$ curve and appearance of a new peak at $R \approx 1.9$ Å in the LDF curve. Concurrent with this, we also observe a drastic change of relative intensities between the even and odd peaks in the $M(s)$ curves. In graphite with the interlayer spacing of $d_0 = c_0/2 = 3.35$ Å, the even Bragg peaks $n = 4, 6$ are labeled $(0,0,8)$ and $(0,0,12)$, and the odd peaks $n = 3, 5$ are labeled $(0,0,6)$ and $(0,0,10)$, respectively. The observed higher intensity of the $(0,0,12)$ peak with

respect to the $(0, 0, 10)$ peak in Fig. 8.3(b) cannot be explained by thermal vibrations and suggests a significant structural change. Consistent with the fact that only the even diffraction peaks should be present in the structure of diamond, and also with the observation of a well-defined interlayer bond at $R \approx 1.9$ Å, we conclude that the transient structure is consistent with sp^3 bonding. We find the transient sp^3-like structure, associated with the relative intensity of the $R \approx 1.9$ Å peak in the LDF curve, to reach a maximum fraction of 47% at 14 ps, as seen in Fig. 8.3 (c). Similar $sp^2 - sp^3$ hybrid structures have also been identified in pressure-driven pathways of graphite-to-diamond transition[143]. By 45 ps, the structure recovers its sp^2 character, but remains hot even after 3 ns with an average value $\Delta \bar{u}^2 = 0.033$ Å^2, corresponding to a lattice temperature $T \approx 1000$ K.

8.2 Theory

To clarify the origin of the structural changes, I studied the effect of laser pulses on the electronic structure and bonding in hexagonal graphite using *ab initio* DFT calculations in the local density approximation (LDA). While much of the basic physics underlying photo-induced structural changes can be understood in the bulk structure, I used graphite slabs representing the surface for quantitative predictions. The total energy was determined using the ABINIT plane-wave code [144] with a 64 Ry energy cutoff, Troullier-Martins pseudopotentials, and the Ceperley-Alder form of the exchange-correlation functional. The Brillouin zone of the $4-$atom bulk unit cell was sampled using a fine mesh of $24 \times 24 \times 12$ k-points that included the $K - H$ line at the Brillouin zone edge, close to the Fermi surface. This approach correctly reproduced the observed [140] in-layer bond length $d_{CC} = 1.42$ Å and the interlayer spacing $d_0 = 3.34$ Å in the bulk system at $T = 0$, shown schematically in Fig. 8.4(a). The electronic density of states of graphite near the Fermi level is shown in Fig. 8.4(b),

and the total charge density is depicted in Fig. 8.4(c) in a plane normal to the layers. In the following, I will study the effect of two types of photo-induced electronic excitations on the structure.

First, I will consider the thermalization of the initial nonequilibrium population of electronic states in the laser-irradiated target over a sub-picosecond time scale [145] to that of a very hot electron gas [146]. The electronic temperature (T_e) is probably lower than the limiting value $k_B T_e \lesssim h\nu = 1.55$ eV and depends on the laser fluence. For the sake of illustration, I compare the Fermi-Dirac distribution in graphite at $k_B T_e = 0$ and $k_B T_e = 1.0$ eV in Fig. 8.4(b), indicating the electronic excitations in the $\pi - \pi^*$ manifold of the hot electron gas. Populating initially empty conduction states by valence electrons leads to a change in the total electron density $\Delta\rho(\mathbf{r}) = \rho(\mathbf{r}; k_B T_e) - \rho(\mathbf{r}; 0)$, which is depicted in Fig. 8.4(d) for $k_B T_e = 1.0$ eV.

As stipulated by DFT, changes in the charge density modify the force field in the system. Our results in Fig. 8.4(d) suggest an increased population of C$2p_z$ orbitals that may hybridize to $pp\sigma$ bonding states connecting neighboring layers, increasing their attraction. The depopulation of in-layer bonding states, on the other hand, should cause an in-layer expansion. To obtain a quantitative estimate of photo-induced structural changes, I performed a set of global structure optimization calculations of graphite with electrons subject to effective temperatures in the range 0 eV$< k_B T < 1.55$ eV. I used a stringent convergence criterion, requiring that all stress components lie below 5.0×10^{-7} Ha/a$_0^3$ and that no force exceeds 5.0×10^{-5} Ha/a$_0$. In bulk graphite, I indeed found that nonzero electronic temperature leads to a maximum interlayer contraction $\Delta d/d_0 = -1\%$ and in-layer expansion $\Delta r_{CC}/r_{CC} = +1\%$ for $k_B T_e \approx 1.0$ eV. In the slab geometry, I obtained a slightly larger interlayer contraction of up to $\Delta d/d_0 = -1.5\%$.

To further take into account the effect of Coulomb stress induced by the laser pulse, I represent the charge separation in the electronic ground state, correspond-

112
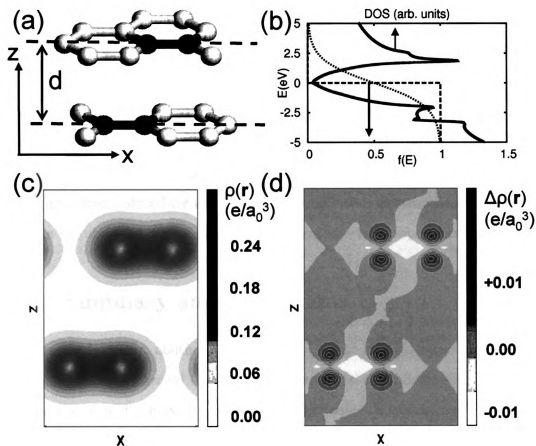
Figure 8.4: (Color online) Electronic structure changes during photo-excitations in graphite. (a) Schematic view of the structure. (b) Electronic density of states (solid line) and the Fermi-Dirac distribution of graphite at $T = 0$ (dashed line) and $k_B T = 1.0$ eV (dotted line). (c) Total pseudo-charge density $\rho(\mathbf{r})$ and (d) change in the pseudo-charge density $\Delta\rho(\mathbf{r})$ due to an electronic temperature increase to $k_B T = 1.0$ eV. The plane used in (c) and (d) intersects the graphene layers along the dashed lines in (a).

ing to the observed internal field of ≈ 1.2 V/Å. To model this system, I immersed three-layer graphite slabs, separated by 30 Å, in a uniform electric field and adjusted its strength to reproduced the observed field value. With the polarized charge distribution frozen in, the external electric field was switched off. Then, the internal field was only due to the polarized charge distribution. The slab calculations were performed using the SIESTA code [87] with double-polarized triple-ζ local basis and a fine 24×24 k-point mesh. The charge density was obtained on a real-space grid with a mesh cutoff energy of 250 Ry. From total energy calculations at different interlayer separations, I found that charge density redistribution associated with the internal field may further reduce the interlayer separation by $2-3\%$. Combined with the contraction induced by the initial non-equilibrium electron heating, I thus can explain the observed contraction of the topmost interlayer separation by up to $\approx 5\%$.

8.3 Summary and conclusions

In conclusion, a nonthermal pathway of photo-induced structural changes in graphite has been observed through multidimensional crystallographic determination in space, time and energy. Beyond a threshold fluence, a transient sp^3-like structure with well-defined interlayer bonds emerges. The modified force field in the excited state and the Coulomb stress are the main forces driving this structural change.

BIBLIOGRAPHY

[1] R. Saito, G. Dresselhaus, and M. Dresselhaus, *Physical Properties of Carbon Nanotubes*, Imperial College Press, 1998.

[2] S. Iijima, *Helical microtubules of graphitic carbon*, Nature **354**, 56 (1991).

[3] A. Thess, R. Lee, P. Nikolaev, H. Dai, P. Petit, J. Robert, C. Xu, Y. Lee, S. Kim, D. Colbert, G. Scuseria, D. Tománek, J. Fischer, and R. Smalley, *Crystalline ropes of metallic carbon nanotubes*, Science **273**, 483 (1996).

[4] Chalcohalides are stable chemical compounds containing chalcogens (S, Se, Te), halides (I, F) and metal ions.

[5] V. Nicolosi, D. Vrbanic, A. Mrzel, J. McCauley, S. O'Flaherty, D. Mihailovic, W. J. Blau, and J. N. Coleman, *Solubility of $Mo_6S_{4.5}I_{4.5}$ nanowires*, Chem. Phys. Lett **401**, 13 (2005).

[6] V. Nicolosi, D. Vrbanic, A. Mrzel, J. McCauley, S. O'Flaherty, C. McGuinness, G. Compagnini, D. Mihailovic, W. J. Blau, and J. N. Coleman, *Solubility of $Mo_6S_{4.5}I_{4.5}$ Nanowires in Common Solvents: A Sedimentation Study*, J. Phys. Chem. B **109**, 7124 (2005).

[7] A. Simon, *Clusters Of Valence Electron Poor Metals - Structure, Bonding, And Properties*, Angew. Chem., Int. Ed. Engl. **27**, 159 (1988).

[8] B. Bercic, U. Pirnat, P. Kusar, D. Dvorsek, D. Mihailovic, D. Vengust, and B. Podobnik, *Transport properties of $Mo_6S_3I_6$ nanowire networks*, Appl. Phys. Lett. **88**, 173103 (2006).

[9] J. V. Lauritsen, J. Kibsgaard, S. Helveg, H. Topsøe, B. S. Clausen, E. Lægsgaard, and F. Besenbacher, *Size-dependent structure of MoS_2 nanocrystals*, Nature Nanotechnology **2**, 53 (2007).

[10] L. Rapoport, Y. Bilik, Y. Feldman, M. Homyonfer, S. R. Cohen, and R. Tenne, *Hollow nanoparticles of WS_2 as potential solid-state lubricants*, Nature (London) **387**, 791 (1997).

[11] L. Joly-Pottuz, F. Dassenoy, M. Belin, B. Vacher, J. Martin, and N. Fleischer, *Ultralow-friction and wear properties of IF-WS2 under boundary lubrication*, Tribology Letters **18**, 477 (2005).

[12] M. S. Dresselhaus, G. Dresselhaus, and P. Avouris, *Carbon Nanotubes: Synthesis, Structure, Properties and Applications*, Springer, Berlin, 2001.

[13] D. Vrbanic, M. Remskar, A. Jesih, A. Mrzel, P. Umek, M. Ponikvar, B. Jancar, A. Meden, B. Novosel, S. Pejovnik, P. Venturini, J. C. Coleman, and D. Mihailovic, *Air-stable monodispersed $Mo_6S_3I_6$ nanowires*, Nanotechnology **15**, 635 (2004).

[14] T. Hughbanks and R. Hoffmann, *Molybdenum chalcogenides: Clusters, chains, and extended solids. The approach to bonding in three dimensions*, J. Am. Chem. Soc. **105**, 1150 (1983).

[15] M. Potel, R. Chevrel, M. Sergent, J. Armici, M. Decroux, and O. Fischer, *New pseudo-one-dimensional metals: $M_2Mo_6Se_6$ (M = Na, In, K, TI), $M_2Mo_6S_6$ (M = K, Rb, Cs), $M_2Mo_6Te_6$ (M = In, TI)*, J. Solid State Chem. **35**, 286 (1980).

[16] F. J. Ribeiro, D. J. Roundy, and M. L. Cohen, *Electronic properties and ideal tensile strength of MoSe nanowires*, Phys. Rev. B **65**, 153401 (2002).

[17] L. Venkataraman and C. M. Lieber, *Molybdenum Selenide Molecular Wires as One-Dimensional Conductors*, Phys. Rev. Lett. **83**, 5334 (1999).

[18] S. Gemming, G. Seifert, and I. Vilfan, *Li doped Mo_6S_6 nanowires: elastic and electronic properties*, Phys. Stat. Sol. (b) **243**, 3320 (2006).

[19] A. Jorio, M. Dresselhaus, and G. Dresselhaus, *Carbon Nanotubes: Advanced Topics in the Synthesis, Structure, Properties and Applications*, Springer, Berlin, 2008.

[20] D. Vrbanic, M. Remskar, A. Jesih, A. Mrzel, P. Umek, M. Ponikvar, B. Jancar, A. Meden, B. Novosel, S. Pejovnik, P. Venturini, J. C. Coleman, and D. Mihailovic, *Air-stable monodispersed $Mo_6S_3I_6$ nanowires*, Nanotechnology **15**, 635 (2004).

[21] A. Meden, A. Kodre, J. P. Gomilsek, I. Arcon, I. Vilfan, D. Vrbanic, A. Mrzel, and D. Mihailovic, *Atomic and electronic structure of $Mo_6S_{9-x}I_x$ nanowires*, Nanotechnology **16**, 1578 (2005).

[22] M. Zumer, V. Nemani, B. Zajec, M. skar, M. Ploscaru, D. Vengust, A. Mrzel, and D. Mihailovic, *Field emission of point-electron source $Mo_6S_3I_6$ nanowires*, Nanotechnology **16**, 1619 (2005).

[23] M. Ploscaru, S. J. Kokalj, M. Uplaznik, D. Vengust, D. Turk, and D. Mihailovic, *Force spectroscopy measurements of $MoSI_x$ nanowires with functionalized molecules*, Physica Status Solidi B-Basic Solid State Physics **243**, 3325 (2006).

116

[24] Z. Kutnjak, D. Vrbanic, S. Pejovnik, and D. Mihailovic, *Two-channel electrical conduction in air-stable monodispersed $Mo_6S_3I_6$ nanowire sheets*, J. Appl. Phys **99**, 064311 (2006).

[25] B. Bercic, U. Pirnat, P. Kusar, D. Dvorsek, D. Mihailovic, D. Vengust, and B. Podobnik, *Transport properties of $Mo_6S_3I_6$ nanowire networks*, Appl. Phys. Lett. **88**, 173103 (2006).

[26] A. Kis, G. Csanyi, D. Vrbanic, A. Mrzel, D. Mihailovic, A. Kulik, and L. Forro, *Nanomechanical investigation of $Mo_6S_{9-x}I_x$ nanowire bundles*, Small **3**, 1544 (2007).

[27] D. N. McCarthy, V. Nicolosi, D. Vengust, D. Mihailovic, G. Compagnini, W. J. Blau, and J. N. Coleman, *Dispersion and purification of $Mo_6S_3I_6$ nanowires in organic solvents*, J. Appl. Phys **101**, 014317 (2007).

[28] J. C. Lasjaunias, A. Sulpice, K. Biljakovic, D. Vengust, and D. Mihailovic, *Low-energy vibrational excitations of $Mo_6S_3I_6$ nanowires revealed by low-temperature specific heat*, Nanotechnology **18**, 355704 (2007).

[29] D. Vrbanic, S. Pejovnik, D. Mihailovic, and Z. Kutnjak, *Electrical conductivity of $Mo_6S_3I_6$ and $Mo_6S_{4.5}I_{4.5}$ nanowires*, Journal of the European Ceramic Society **27**, 975 (2007).

[30] R. Murphy, V. Nicolosi, Y. Hernandez, D. McCarthy, D. Rickard, D. Vrbanic, A. Mrzel, D. Mihailovic, W. J. Blau, and J. N. Coleman, *Observation of extremely low percolation threshold in $Mo_6S_{4.5}I_{4.5}$ nanowire/polymer composites*, Scripta Materialia **54**, 417 (2006).

[31] M. I. Ploscaru, S. J. Kokalj, M. Uplaznik, D. Vengust, D. Turk, A. Mrzel, and D. Mihailovic, *$Mo_6S_{9-x}I_x$ nanowire recognitive molecular-scale connectivity*, Nano Lett. **7**, 1445 (2007).

[32] J. J. Doyle, V. Nicolosi, S. M. O'Flaherty, D. Vengust, A. Drury, D. Mihailovic, J. N. Coleman, and W. J. Blau, *Nonlinear optical response of $Mo_6S_{4.5}I_{4.5}$ nanowires*, Chem. Phys. Lett **435**, 109 (2007).

[33] V. Nicolosi, P. D. Nellist, S. Sanvito, E. C. Cosgriff, S. Krishnamurthy, W. J. Blau, M. L. H. Green, D. Vengust, D. Dvorsek, D. Mihailovic, G. Compagnini, J. Sloan, V. Stolojan, J. D. Carey, S. J. Pennycook, and J. N. Coleman, *Observation of van der Waals driven self-assembly of MoSI nanowires into a low-symmetry structure using aberration-corrected electron microscopy*, Adv. Mater. **19**, 543 (2007).

[34] V. Nicolosi, D. Vengust, D. Mihailovic, W. J. Blau, and J. N. Coleman, *De-bundling by dilution: Observation of significant populations of individual MoSI nanowires in high concentration dispersions*, Chem. Phys. Lett **425**, 89 (2006).

117

[35] T. Yang, S. Okano, S. Berber, and D. Tomanek, *Interplay between Structure and Magnetism in $Mo_{12}S_9I_9$ Nanowires*, Phys. Rev. Lett. **96**, 125502 (2006).

[36] I. Vilfan and D. Mihailovic, *Nonlinear elastic and electronic properties of $Mo_6S_3I_6$ nanowires*, Phys. Rev. B **74**, 235411 (2006).

[37] D. Vengust, F. Pfuner, L. Degiorgi, I. Vilfan, V. Nicolosi, J. N. Coleman, and D. Mihailovic, *Optical properties of $Mo_6S_3I_6$ nanowires*, Phys. Rev. B **76**, 075106 (2007).

[38] European Patent, PCT/EP 2004/001870.

[39] L. Joly-Pottuz, F. Dassenoy, J. Martin, D. Vrbanic, A. Mrzel, D. Mihailovic, W. Vogel, and G. Montagnac, *Tribological properties of Mo-S-I nanowires as additive in oil*, Tribology Letters **18**, 385 (2005).

[40] G. Paglia, E. S. Bozin, D. Vengust, D. Mihailovic, and S. J. L. Billinge, *Accurate structure determination of $Mo_6S_yI_z$ nanowires from atomic pair distribution function (PDF) analysis*, Chem. Mater. **18**, 100 (2006).

[41] V. Nicolosi, S. Berber, J. N. Coleman, J. Sloan, D. Tománek, D. Mihailovic, and W. J. Blau, *Atomic and electronic structure of $Mo_6S_{9-x}I_x$ nanowires*, (presentation at the NT'04 conference on the Science and Application of Nanotubes, San Luis Potosi, Mexico, July 19-23, 2004.).

[42] P. Ball, *The Self-Made Tapestry: Pattern Formation in Nature*, Oxford University Press, 2001.

[43] A. E. Busnaina, *Nanomanufacturing Handbook*, CRC Press, 2006.

[44] R. D. Piner, J. Zhu, F. Xu, S. Hong, and C. A. Mirkin, *"Dip-Pen" Nanolithography*, Science **283**, 661 (1999).

[45] J.-F. Liu and G. P. Miller, *Field-Assisted Nanopatterning*, J. Phys. Chem. C **111**, 10758 (2007).

[46] J. S. Foster and J. E. Frommer, *Imaging of liquid-crystals using a tunnelling microscope*, Nature **333**, 542 (1988).

[47] T. Muller, T. L. Werblowsky, G. M. Florio, B. J. Berne, and G. W. Flynn, *Ultra-high vacuum scanning tunneling microscopy and theoretical studies of 1-halohexane monolayers on graphite*, Proceedings of the National Academy of Sciences of the United States of America **102**, 5315 (2005).

[48] D. M. Cyr, B. Venkataraman, and G. W. Flynn, *STM investigations of organic molecules physisorbed at the liquid-solid interface*, Chemistry of Materials **8**, 1600 (1996).

[49] J. P. Rabe and S. Buchholz, *Commensurability And Mobility In 2-Dimensional Molecular-Patterns On Graphite*, Science **253**, 424 (1991).

[50] D. Bonifazi, O. Euger, and F. Diederich, *Supramolecular [60]fullerene chemistry on surfaces*, **36**, 390 (2007).

[51] C. Joachim, J. K. Gimzewski, and A. Aviram, *Electronics using hybrid-molecular and mono-molecular devices*, Nature **408**, 541 (2000).

[52] S. Lloyd, *A potentially realizable quantum computer*, Science **261**, 1569 (1993).

[53] W. Harneit, *Fullerene-based electron-spin quantum computer*, Phys. Rev. A **65**, 032322 (2002).

[54] J. V. Barth, G. Constantini, and K. Kern, *Engineering atomic and molecular nanostructures at surfaces*, Nature **437**, 671 (2005).

[55] F. Rosei, M. Schunack, Y. Naitoh, P. Jiang, A. Gourdon, E. Laegsgaard, I. Stensgaard, C. Joachim, and F. Besenbacher, *Properties of large organic molecules on metal surfaces*, **71**, 95 (2003).

[56] K. Nasu, editor, *Photoinduced Phase Transitions*, World Scientific, Hackensack, USA, 2004.

[57] C. Z. Wang, K. M. Ho, M. D. Shirk, and P. A. Molian, *Laser-Induced Graphitization on a Diamond (111) Surface*, Phys. Rev. Lett. **85**, 4092 (2000).

[58] T. Meguro, A. Hida, M. Suzuki, Y. Koguchi, H. Takai, Y. Yamamoto, K. Maeda, and Y. Aoyagi, *Creation of nanodiamonds by single impacts of highly charged ions upon graphite*, Appl. Phys. Lett. **79**, 3866 (2001).

[59] H. Nakayama and H. Katayama-Yoshida, *Direct conversion of graphite into diamond through electronic excited states*, J.Phys: Condens. Matter **15**, R1077 (2003).

[60] S. Fahy, S. G. Louie, and M. L. Cohen, *Pseudopotential total-energy study of the transition from rhombohedral graphite to diamond*, Phys. Rev. B **34**, 1191 (1986).

[61] G. W. Yang and J. B. Wang, *Pulsed-laser-induced transformation path of graphite to diamond via an intermediate rhombohedral graphite*, Appl. Phys. A: Mater. Sci. Process. **72**, 475 (2001).

[62] S. Ashitkov, M. B. Agranat, P. S. Kondratenko, S. I. Anisimov, V. E. Fortov, V. V. Temnov, K. Sokolowski-Tinten, P. Zhou, and D. von der Linde, *Ultrafast structural transformations in graphite*, JETP Lett. **75**, 87 (2002).

[63] D. H. Reitze, H. Ahn, and M. C. Downer, *Optical properties of liquid carbon measured by femtosecond spectroscopy*, Phys. Rev. B **45**, 2677 (1992).

[64] T. Mishina, K. Nitta, and Y. Masumoto, *Coherent lattice vibration of interlayer shearing mod of graphite*, Phys. Rev. B **62**, 2908 (2000).

[65] K. Ishioka, M. Hase, M. Kitajima, and K. Ushida, *Ultrafast carrier and phonon dynamics in ion-irradiated graphite*, Appl. Phys. Lett **78**, 3965 (2001).

[66] M. Bargheer, N. Zhavoronkov, M. Woerner, and T. Elsaesser, *Recent Progress in Ultrafast X-ray Diffraction*, ChemPhysChem **7**, 783 (2006).

[67] A. H. Zewail, *4D Ultrafast electron diffraction, crystallography, and microscopy*, Ann. Rev. Phys. Chem. **57**, 65 (2006).

[68] J. R. Dwyer, C. T. Hebeisen, R. Ernstorfer, V. B. Deyirmenjian, R. E. Jordan, and R. J. D. Miller, *Femtosecond electron diffraction: "Making the molecular movie"*, Phil. Trans. R. Soc. A **364**, 741 (2006).

[69] H. Park, X. Wang, S. Nie, R. Clinite, and J. Cao, *Direct and real-time probing of both coherent and thermal lattice motions*, Solid State Commun. **136**, 559 (2005).

[70] C.-Y. Ruan, Y. Murooka, R. Raman, and R. Murdick, *Dynamics of Size-Selected Gold Nanoparticles Studied by Ultrafast Electron Nanocrystallography*, Nano Lett. **7**, 1290 (2007).

[71] A. Janzen, B. Krenzer, P. Zhou, D. von der Linde, and M. Horn-von Hoegen, *Ultrafast electron diffraction at surfaces after laser excitation*, Surface Science **600**, 4094 (2006).

[72] R. M. Martin, *Electronic Structure: Basic Theory and Practical Methods*, Cambridge University press, 2004.

[73] M. Born and R. Oppenheimer, *Quantum theory of molecules*, Annalen Der Physik **84**, 0457 (1927).

[74] D. R. Hartree, *The Wave Mechanics of an Atom with a Non-Coulomb Central Field. Part I. Theory and Methods*, Proc. Cam. Phil. Soc. **24–111**, 89 (1928).

[75] V. Fock, *Naherungsmethode zur Losung des quantenmechanischen Mehrkorperproblems*, Z. Physik **61**, 126 (1930).

[76] P. Hohenberg and W. Kohn, *Inhomogeneous Electron Gas*, Physical Review **136**, B864 (1964).

[77] W. Kohn and L. Sham, *Self-Consistent Equations Including Exchange and Correlation Effects*, Physical Review **140**, A1133 (1965).

[78] P. Ordejón, E. Artacho, and J. M. Soler, *Self-consistent order-N density-functional calculations for very large systems*, Phys. Rev. B **53**, R10441 (1996).

[79] D. SanchezPortal, P. Ordejon, E. Artacho, and J. M. Soler, *Density-functional method for very large systems with LCAO basis sets*, International Journal of Quantum Chemistry **65**, 453 (1997).

[80] E. Artacho, D. Sanchez-Portal, P. Ordejon, A. Garcia, and J. M. Soler, *Linear-scaling ab-initio calculations for large and complex systems*, Physica Status Solidi B-Basic Research **215**, 809 (1999).

[81] S. Baroni, A. D. Corso, S. de Gironcoli, P. Giannozzi, C. Cavazzoni, G. Ballabio, S. Scandolo, G. Chiarotti, P. Focher, A. Pasquarello, K. Laasonen, A. Trave, R. Car, N. Marzari, and A. Kokalj, http://www.pwscf.org/.

[82] M. C. Payne, M. P. Teter, D. C. Allan, T. A. Arias, and J. D. Joannopoulos, *Iterative minimization techniques for ab initio total-energy calculations: molecular dynamics and conjugate gradients*, Rev. Mod. Phys. **64**, 1045 (1992).

[83] J. P. Perdew, K. Burke, and M. Ernzerhof, *Generalized Gradient Approximation Made Simple*, Phys. Rev. Lett. **77**, 3865 (1996).

[84] D. M. Ceperley and B. J. Alder, *Ground State of the Electron Gas by a Stochastic Method*, Phys. Rev. Lett. **45**, 566 (1980).

[85] G. Ortiz and P. Ballone, *Correlation energy, structure factor, radial distribution function, and momentum distribution of the spin-polarized uniform electron gas*, Phys. Rev. B **50**, 1391 (1994).

[86] Y. Kwon, D. M. Ceperley, and R. M. Martin, *Effects of backflow correlation in the three-dimensional electron gas: Quantum Monte Carlo study*, Phys. Rev. B **58**, 6800 (1998).

[87] J. M. Soler, E. Artacho, J. D. Gale, A. García, J. Junquera, P. Ordejón, and D. Sánchez-Portal, *The SIESTA method for ab initio order-N materials simulation*, J. Phys: Condens. Matter **14**, 2745 (2002).

[88] D. R. Hamann, M. Schlüter, and C. Chiang, *Norm-Conserving Pseudopotentials*, Phys. Rev. Lett. **43**, 1494 (1979).

[89] N. Troullier and J. L. Martins, *Efficient pseudopotentials for plane-wave calculations*, Physical Review B **43**, 1993 (1991).

[90] D. Vanderbilt, *Soft self-consistent pseudopotentials in a generalized eigenvalue formalism*, Phys. Rev. B **41**, 7892 (1990).

[91] D. M. Ceperley and B. J. Alder, *Ground-state of the electron-gas by a stochastic method*, Physical Review Letters **45**, 566 (1980).

[92] L. Kleinman and D. M. Bylander, *Efficacious form for model pseudopotentials*, Physical Review Letters **48**, 1425 (1982).

[93] J. Junquera, O. Paz, D. Sánchez-Portal, and E. Artacho, *Numerical atomic orbitals for linear-scaling calculations*, Phys. Rev. B **64**, 235111 (2001).

121

[94] S. F. Boys and F. Bernardi, *Calculation of small molecular interactions by differences of separate total energies - some procedures with reduced errors*, Molecular Physics **19**, 553 (1970).

[95] D. Pinchon and P. E. Hoggan, *New index functions for storing Gaunt coefficients*, International Journal of Quantum Chemistry **107**, 2186 (2007), Pinchon, Didier Hoggan, Philip E.

[96] O. F. Sankey and D. J. Niklewski, *Ab initio multicenter tight-binding model for molecular-dynamics simulations and other applications in covalent systems*, Phys. Rev. B **40**, 3979 (1989).

[97] E. Kaxiras, *Atomic and Electronic Structure of Solids*, Cambridge University press, 2003.

[98] P. P. Ewald, *Die Berechnung optischer und electrostatischer Gitterpotentiale*, Ann. der Physik **64**, 253 (1921).

[99] M. T. Yin and M. L. Cohen, *Will Diamond Transform under Megabar Pressures?*, Phys. Rev. Lett. **50**, 2006 (1983).

[100] J. P. Perdew and A. Zunger, *Self-interaction correction to density-functional approximations for many-electron systems*, Physical Review B **23**, 5048 (1981).

[101] Details of the electronic structure were obtained using a finer mesh of 16 k-points.

[102] Since the X-ray diffraction peaks in the direction of $Mo_{12}S_9I_9$ nanowires appear somewhat diffuse, we believe that the long-range order, including the lattice constant, is not as well defined as the short range oder.

[103] A. Hassanien, M. Tokumoto, A. Mrzel, D. Mihailovic, and H. Kataura, *Structural and mechanical properties of MoS_2-I_x nanotubes and $Mo_6S_xI_y$ nanowires*, Physica E **29**, 684 (2005).

[104] R. T. Senger, S. Tongay, E. Durgun, and S. Ciraci, *Atomic chains of group-IV elements and III-V and II-VI binary compounds studied by a first-principles pseudopotential method*, Phys. Rev. B **72**, 075419 (2005).

[105] Y. Feldman, E. Wasserman, D. Srolovitz, and R. Tenne, *High Rate, Gas Phase Growth of MoS_2 Nested Inorganic Fullerenes and Nanotubes*, Science **267**, 222 (1995).

[106] G. Seifert, H. Terrones, M. Terrones, G. Jungnickel, and T. Frauenheim, *Structure and Electronic Properties of MoS_2 Nanotubes*, Phys. Rev. Lett. **85**, 146 (2000).

[107] M. Remskar, A. Mrzel, Z. Skraba, A. Jesih, M. Ceh, J. Demšar, P. Stadelmann, F. Lévy, and D. Mihailovic, *Self-Assembly of Subnanometer-Diameter Single-Wall MoS_2 Nanotubes*, Science **292**, 479 (2001).

[108] M. Verstraete and J. C. Charlier, *Ab initio study of MoS$_2$ nanotube bundles*, Phys. Rev. B **68**, 045423 (2003).

[109] A. Zimina, S. Eisebitt, M. Freiwald, S. Cramm, W. Eberhardt, A. Mrzel, and D. Mihailovic, *Electronic Structure of Subnanometer Diameter MoS$_2$-I$_x$ Nanotubes*, Nano Lett. **4**, 1749 (2004).

[110] I. Popov, T. Yang, S. Berber, G. Seifert, and D. Tomanek, *Unique Structural and Transport Properties of Molybdenum Chalcohalide Nanowires*, Phys. Rev. Lett. **99**, 085503 (2007).

[111] J. Taylor, H. Guo, and J. Wang, *Ab inito modeling of quantum transport properties of molecular electronic devices*, Phys. Rev. B **63**, 245407 (2001).

[112] M. Brandbyge, J.-L. Mozos, P. Ordejon, J. Taylor, and K. Stokbro, *Density functional method for nonequilibrium electron transport*, Phys. Rev. B **65**, 165401 (2002).

[113] D. Porezag, T. Frauenheim, T. Köhler, G. Seifert, and R. Kaschner, Phys. Rev. B **51**, 12947 (1995).

[114] G. Seifert, D. Porezag, and T. Frauenheim, *Calculations of molecules, clusters, and solids with a simplified LCAO-DFT-LDA scheme*, Int. J. Quant. Chem. **58**, 185 (1996).

[115] G. Seifert, H. Terrones, M. Terrones, G. Jungnickel, and T. Frauenheim, *Structure and electronic properties of MoS$_2$ nanotubes*, Phys. Rev. Lett. **85**, 146 (2000).

[116] In analogy to the mixing energy, we define ΔE as the energy gain upon forming a Mo$_6$S$_{6-x}$I$_x$ nanowire from non-interacting Mo$_6$S$_6$ and Mo$_6$I$_6$ segments of proper length ratio.

[117] L. Zhechkov, T. Heine, S. Patchkovskii, G. Seifert, and H. Duarte, *Efficient A Posteriori Treatment for Dispersion Interaction in Density Functional-Based Tight Binding*, J. Chem. Theory Comput. **1**, 841 (2005).

[118] Y.-K. Kwon, D. Tománek, Y. H. Lee, K. H. Lee, and S. Saito, *Do carbon nanotubes spin when bundled?*, J. Mater. Res. **13**, 2363 (1998).

[119] Y.-K. Kwon and D. Tománek, *Orientational melting in carbon nanotube ropes*, Phys. Rev. Lett. **84**, 1483 (2000).

[120] T. Yang, S. Berber, and D. Tomanek, *Compositional ordering and quantum transport in Mo$_6$S$_{9-x}$I$_x$ nanowires: Ab initio calculations*, Phys. Rev. B **77**, 165426 (2008).

[121] F. A. Cotton and G. Wilkinson, *Advanced inorganic chemistry: A comprehensive text*, Interscience Publishers, New York, 1966.

[122] I. Vilfan, Mo_6S_6 *nanowires: structural, mechanical and electronic properties*, The European Physical Journal B **51**, 277 (2006).

[123] In analogy with the energy gain upon mixing two pure components in an alloy, we define $\Delta E_b = E_b- < E_b >$ as the energy gain associated with mixing Mo_6S_9 and $Mo_6S_3I_6$ with S_3 bridges into a homogeneous nanowire with the composition $Mo_6S_{9- <x>}I_{<x>}$.

[124] D. Mihailovic, (private communication).

[125] T. Yang, S. Berber, J.-F. Liu, G. P. Miller, and D. Tomanek, *Self-assembly of long chain alkanes and their derivatives on graphite*, J. Chem. Phys. **128**, 124709 (2008).

[126] Density functional theory (DFT) is best known for its structural predictions in covalently bonded systems. Within the local density approximation (LDA), DFT is moreover known to correctly reproduce even the equilibrium structure of weakly interacting systems such as graphite that are held together – to an important degree – by van der Waals forces. In reality, van der Waals forces are not neglected in DFT, but enter in an approximate way through the exchange-correlation functional.

[127] G. C. McGonigal, R. H. Bernhardt, and D. J. Thomson, *Imaging Alkane Layers At The Liquid Graphite Interface With The Scanning Tunneling Microscope*, Applied Physics Letters **57**, 28 (1990).

[128] W. Liang, M. H. Whangbo, A. Wawkuschewski, H. J. Cantow, and S. N. Magonov, *Electronic Origin Of Scanning-Tunneling-Microscopy Images And Carbon Skeleton Orientations Of Normal-Alkanes Adsorbed On Graphite*, Advanced Materials **5**, 817 (1993).

[129] S. Abrahamsson, G. Larsson, and E. Vonsydow, *The Crystal Structure Of The Monoclinic Form Of Normal-Hexadecanol*, Acta Crystallographica **13**, 770 (1960).

[130] B. Diaconescu, T. Yang, S. Berber, M. Jazdzyk, G. P. Miller, D. Tománek, and K. Pohl, *Molecular Self-Assembly of Functionalized Fullerenes on a Metal Surface*, Phys. Rev. Lett. **102**, 056102 (2009).

[131] *Ortho*-catechol was alkylated using two equivalents of 1-iodooctadecane and then bromomethylated in regioselective fashion to produce 1,2-dioctadecyloxy-4,5-dibromomethylbenzene, an *ortho*-quinodimethane precursor. Reaction with iodide in the presence of C_{60} generates the corresponding 1,2-diocta-decyloxy-4,5-quinodimethane which undergoes a [4+2] cycloaddition across C_{60} to produce the final functionalized fullerene.

[132] G. P. Miller and J. Mack, *Completely Regioselective, Highly Stereoselective Syntheses of cis-Bisfullerene[60] Adducts of 6,13-Disubstituted Pentacenes*, Organic Letters **2**, 3979 (2000).

[133] G. P. Miller and J. B. Briggs, *Fullerene-Acene Chemistry: Diastereoselective Synthesis of a cis,cis-Tris[60]fullerene Adduct of 6,8,15,17-Tetraphenylheptacene*, Organic Letters **5**, 4203 (2003).

[134] B. Diaconescu, G. Nenchev, J. de la Figuera, and K. Pohl, *An ultra high vacuum fast-scanning and variable temperature scanning tunneling microscope for large scale imaging*, Rev. Sci. Instr. **78**, 103701 (2007).

[135] E. I. Altman and R. J. Colton, *Determination of the orientation of C_{60} adsorbed on Au(111) and Ag(111)*, Phys. Rev. B **48**, 18244 (1993).

[136] J. P. Perdew and A. Zunger, *Self-interaction correction to density-functional approximations for many-electron systems*, Phys. Rev. B **23**, 5048 (1981).

[137] D. Vanderbilt, *Soft self-consistent pseudopotentials in a generalized eigenvalue formalism*, Phys. Rev. B **41**, 7892 (1990).

[138] L.-L. Wang and H.-P. Cheng, *Density functional study of the adsorption of a C_{60} monolayer on Ag(111) and Au(111) surfaces*, Phys. Rev. B **69**, 165417 (2004).

[139] R. K. Raman, Y. Murooka, C.-Y. Ruan, T. Yang, S. Berber, and D. Tomanek, *Direct Observation of Optically Induced Transient Structures in Graphite Using Ultrafast Electron Crystallography*, Phys. Rev. Lett. **101**, 077401 (2008).

[140] B. T. Kelly, *Physics of Graphite*, Applied Science, London, 1981.

[141] T. Kampfrath, L. Perfetti, F. Schapper, C. Frischkorn, and M. Wolf, *Strongly Coupled Optical Phonons in the Ultrafast Dynamics of the Electronic Energy and Current Relaxation in Graphite*, Phys. Rev. Lett **95**, 187403 (2005).

[142] R. A. Murdick, R. K. Raman, Y. Murooka, and C.-Y. Ruan, *Photovoltage dynamics of the hydroxylated Si(111) surface investigated by ultrafast electron diffraction*, Physical Review B **77**, 245329 (2008).

[143] W. L. Mao, H.-k. Mao, P. J. Eng, T. P. Trainor, M. Newville, C.-c. Kao, D. L. Heinz, J. Shu, Y. Meng, and R. J. Hemley, *Bonding Changes in Compressed Superhard Graphite*, Science **302**, 425 (2003).

[144] The ABINIT code is a common project of the Université Catholique de Louvain, Corning Incorporated, and other contributors (URL http://www.abinit.org).

[145] Y. Miyamoto, A. Rubio, and D. Tománek, *Real-Time Ab Initio Simulations of Excited Carrier Dynamics in Carbon Nanotubes*, Phys. Rev. Lett. **97** (2006).

[146] P. L. Silvestrelli, A. Alavi, M. Parrinello, and D. Frenkel, *Ab initio Molecular Dynamics Simulation of Laser Melting of Silicon*, Phys. Rev. Lett. **77**, 3149 (1996).